Mars Magnetotail Current Sheet Dynamics in Multispecies MHD Simulations

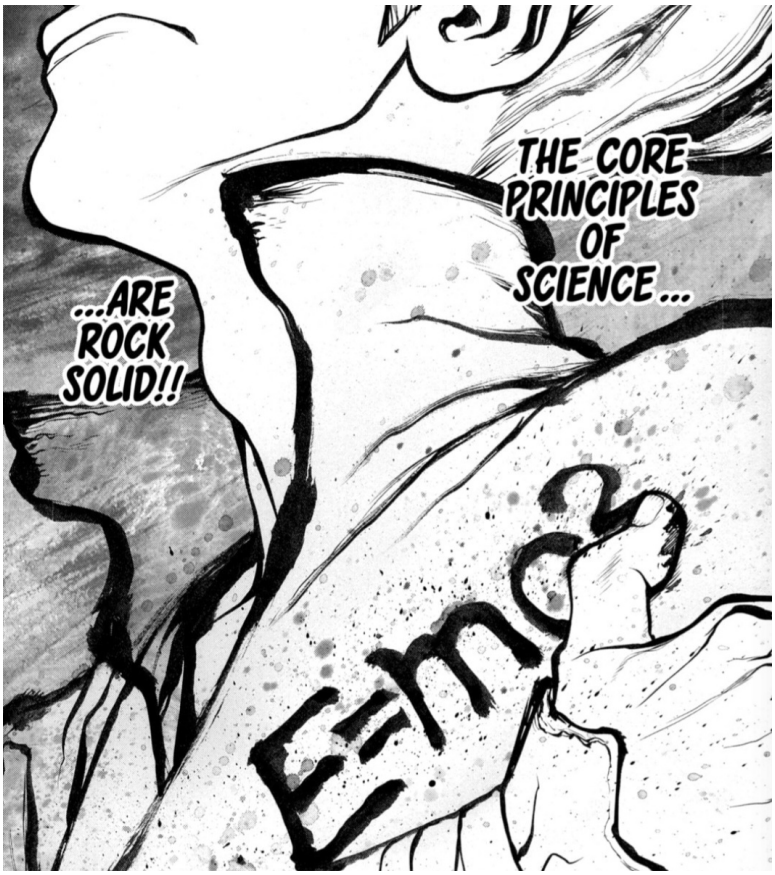
by

Nii-Boi Quartey

A dissertation submitted in partial fulfillment
of the requirements for the degree of
Doctor of Philosophy
(Applied Physics)
in the University of Michigan
2026

Doctoral Committee:

Professor Michael Liemohn, Chair
Professor Xianzhe Jia
Professor Mark Moldwin
Assistant Research Scientist Alexander Shane
Assistant Professor Lulu Zhao



Cover image: Panel from Dr. Stone, written by Riichiro Inagaki and illustrated by Boichi

Nii-Boi Quartey
nquartey@umich.edu
ORCID iD: 0009-0007-7278-5328

© Nii-Boi Quartey 2026

DEDICATION

To my family, for their support throughout this journey.

ACKNOWLEDGEMENTS

First and foremost, I would like to thank my dissertation chair and the greatest advisor of all time, Dr. Michael Liemohn. Mike created an environment where I felt supported, challenged, and encouraged to grow as a scientist, giving me the freedom to explore my own ideas while being there for me when I needed direction. He has been a phenomenal mentor, and I am forever grateful for his mentorship for the past four years.

I would also like to thank the members of my dissertation committee Dr. Mark Moldwin, Dr. Xianzhe Jia, Dr. Lulu Zhao, and Dr. Alexander Shane, and my preliminary exam committee member Dr. Matti Ala-Lahti. Their guidance and suggestions of my various projects helped shape my academic path and made me a better researcher.

I'd like to thank Applied Physics Chairs Dr. Cagliyan Kurdak and Dr. Vanessa Sih, Academic Chair Cynthia McNabb, and the various program assistants for their guidance in my time as an Applied Physics student. I am grateful for their willingness to help me navigate the many moving parts of the Applied Physics Program.

Throughout my time at Michigan, I've made many friends, and perhaps a few enemies. There are so many people I'd like to thank: my lab group and office 1435, my Applied Physics cohort and honorary cohort members, the MITHRAS group, coauthors, Applied Physicists, CLASPers, MAVENites, my Physics 141 students, AP and CLASP faculty and staff, and the many people I got to meet at conferences.

I've also had the opportunity to lead two phenomenal organizations. I'd like to thank the organizing committee members of the Michigan Geophysical Union and the executive board of the National Society of Black Physicists, along with members and attendees who shape these organizations into what they are.

I've heard constantly throughout my time as a graduate student the importance of maintaining a good work-life balance. I achieved this through sports, specifically running and volleyball. I'd first like to thank my Michigan Outback Relay team *We Argoners* for a fun yet exhausting three-day that gave me a chance to experience the Upper Peninsula in a way that was scenic and tiring. I'd also like to thank the many friends I met playing volley-

ball at the NCRB. A hige thank you to my teammates across competitive and recreational teams: *Sparkly Unicorn*, *Yay Woohoo*, *Team Team*, *Otterside Hitters*, *Climate and Ace*, *Unc's Knees*, *Soft Serves*, and the overused team name *Gradiators*. Additionally, I'd like to thank my favorite content creators, RDCWorld1, for providing a form of work-life balance that didn't require me to leave my room. The countless skits and streams featuring Mark 'Cash Money Mawk' Phillips, Affiong 'Waff' Harris, Leland 'Mickey Lee' Manigo, Desmond 'OKAYYYDES' Johnson, Benjamin 'Ben-san' Skinner, Dylan 'The Big Dyl' Patel, and John 'J.O.H.N.' Newton helped entertain me when I was too lazy to socialize.

Finally, I'd like to thank my life advisors, otherwise known as my family, for their unwavering support and guidance. To my father, Robert and my mother, Clara, thank you for supporting my decision to attend graduate school and encouraging me the whole way. To my older sister Naa-Kwarley, I can't thank you enough for the your recommendation to apply for a PhD program in the first place. I never intended to pursue a PhD, but your support and guidance especially in my first two years were so crucial to my success as a graduate student. And to my older twin brother Nii-Kwartei, thank you for the many memes and inside jokes you shared that had me trying my hardest not to laugh aloud in public. I would also like to thank my extended family in the United States and Ghana for their all their support and encouragement during my time as a graduate student.

TABLE OF CONTENTS

DEDICATION ii

ACKNOWLEDGEMENTS iii

LIST OF FIGURES viii

LIST OF TABLES xiv

LIST OF ACRONYMS xv

ABSTRACT xvi

CHAPTER

1 Introduction 1

1.1 The Sun 1
1.2 Solar Wind 2
1.3 Planetary Magnetospheres 4
1.4 The Martian Magnetotail 8
1.5 Crustal Magnetic Fields and Planetary Ion Escape 8
1.6 Magnetotail Current Sheet Asymmetry 9
1.6.1 Numerical Simulations 9
1.6.2 Satellite Observations 17
1.6.3 Subsolar Longitude 18
1.6.4 Model Grid Resolution 18
1.7 Objectives 20
1.8 Dissertation Outline 21

2 Model Description and Numerical Methodology 23

2.1 Overview 23
2.2 Ideal MHD Equations 23
2.3 Multispecies MHD 26
2.4 Space Weather Modeling Framework 27
2.5 BATS-R-US Configuration 29

3 Multispecies MHD Simulations of the Crustal Field Influence at the Mars Magnetotail Current Sheet 31

3.1 Introduction . . . 31
3.2 Solar Condition Numerical Methodology . . . 32
3.3 Results . . . 35
3.3.1 Crustal Field Influence . . . 35
3.3.2 Extreme Ionization Rates . . . 38
3.3.3 Dayside Ionosphere . . . 42
3.3.4 MHD Model Comparison . . . 44
3.4 Summary and Conclusions . . . 46

4 Rotational Influence on the Martian Magnetotail Current Sheet: A Multispecies MHD Study . . . 48

4.1 Introduction . . . 48
4.2 Model Setup . . . 49
4.3 Results . . . 50
4.3.1 Magnetic Field Subsolar Longitude Orientation . . . 50
4.3.2 Current Density . . . 54
4.3.3 Mass Flux . . . 57
4.4 Brief Grid Configuration Case Study . . . 64
4.5 Conclusion . . . 65

5 Sensitivity of Mars Multispecies MHD Simulations to Model Configuration Choices . . . 67

5.1 Introduction . . . 67
5.2 Model Description and Configurations . . . 68
5.2.1 BATS-R-US Multispecies MHD Code . . . 68
5.2.2 Baseline Configuration . . . 68
5.2.3 Grid Configuration Adjustments . . . 69
5.3 Results . . . 71
5.3.1 Magnetic Field . . . 71
5.3.2 Total Current Density . . . 76
5.4 Grid Geometry . . . 79
5.5 Conclusion . . . 83

6 Comparison of MAVEN Observations and BATS-R-US Simulations at the Mars Magnetotail Current Sheet . . . 85

6.1 Introduction . . . 85
6.2 MAVEN Trajectory . . . 86
6.3 BATS-R-US Configuration . . . 88
6.4 Results . . . 93
6.5 Discussion . . . 95
6.5.1 BATS-R-US Interval Selection . . . 96
6.5.2 Model Configuration and Resolution . . . 96
6.5.3 Steady-State Assumption . . . 96
6.5.4 Event Selection . . . 97
6.6 Conclusion . . . 97

7 Conclusion **99**
7.1 Summary 99
7.2 Broader Implications 102
7.3 Future Work 103

BIBLIOGRAPHY 105

LIST OF FIGURES

FIGURE

1.1 Diagram of the interior structure of the Sun including key interior and exterior regions. Image courtesy of Kelvin Song *https://commons.wikimedia.org/w/index.php?curid=23371669*. 2

1.2 Schematic of the Parker Spiral in the heliosphere. Streamlines of solar wind wind drag out the Sun's magnetic field as a result of the frozen-in-flux condition and the Sun's rotation. *Image courtesy of Steve Suess, NASA/MSFC*. 3

1.3 Diagram of Earth's intrinsic magnetosphere (Lang, 2005). The bow shock forms near 10 Earth radii on the dayside. The solar wind deflects around the Earth, creating a long magnetotail on the nightside. Solar wind is deflected at the bow shock, flows along the magnetopause into the magnetotail, and is injected back toward the Earth within the plasma sheet. 5

1.4 Sketch of the structure of the Martian plasma environment, depicting the major boundaries and regions in the equatorial plane (Nagy et al., 2004). R_M - Mars radii. 6

1.5 Sketch depicting the geometry of draped magnetic field lines at Mars (Nagy et al., 2004). Positive x points towards the Sun (to the right) and positive z points up from the exliptic plane (out of the page). 7

1.6 Artist depiction of a solar storm hitting Mars, stripping ions from its upper atmosphere. Image credit: NASA Goddard Space Flight Center. 9

1.7 Magnetic field component B in the xy plane (Ma et al., 2002). The color plot shows the magnitude and the white lines with arrows indicate the vector direction of the magnetic field. In this figure, the magnetotail current sheet is shifted towards dusk ($+Y$), as this is the region where the magnetic field lobes intersect and are near zero. 11

1.8 Magnetic field lines in the equatorial plane obtained from an MHD simulation of the Mars-solar wind interaction under nominal solar wind conditions and a Parker spiral IMF (Luhmann et al., 2015). The strongest crustal magnetic fields are at noon. The magnetotail current sheet is shifted dawnward. 12

1.9 Current density J amplitude 1.1 R_M (left) and 2 R_M (right) downtail in the yz plane (Li et al., 2013). The color bar shows the magnitude of the current density and the black arrows show the 2-dimensional component direction in the yz plane. 13

1.10 Calculated magnetic field (left) and average ion velocity (right) in the equatorial plane for solar minimum conditions (Najib et al., 2011). Color plots show the magnitudes and the white lines with arrows show the vector direction of the magnetic field. White arrows on the ion velocity plot show the direction of the velocity. The black dashed lines represent the mean bow shock location (Vignes et al., 2000). The magnetotail current sheet shifts towards dusk. 14
1.11 Magnetic field B intensity in the equatorial plane and the X=-4 R_M plane (Liemohn et al., 2017). The gray sphere is the surface of Mars, the blue-green-pink color bar represents the altitude and the second color bar represents the magnitude of the magnetic field. The view is from above the ecliptic plane in the afternoon sector with the Sun down and to the left. The dots along each axis are space 1 R_M apart. The magnetotail current sheet is shift towards dawn. 15
1.12 Pressure profiles for the seven participating models extracted along the subsolar line (Brain et al., 2010). MHD models are Ma (multispecies), Terada (multispecies), and Harnett (multifluid). Hybrid models are Brecht, Kallio, Modolo, and Boesswetter. Dashed lines indicate dynamic pressure, solid lines indicate plasma thermal pressure, dot-dashed lines indicate magnetic pressure. The darker shaded area in the initial region of the figure indicates regions interior to the planet. 16
1.13 Portion of MAVEN's orbit on 5 May 2015 projected onto the equatorial ($X_{MSO} - Y_{MSO}$) plane (DiBraccio et al., 2015). Nominal induced magnetospheric boundary and bow shock positions are indicated by dashed lines. Normalized magnetic field vector projections are plotted along the trajectory where the color represents the normalized out-of-plane component. The color bar represents the magnetic field in the x-direction B_x. The magnetotail current sheet crossing is oriented in the $+Y$ direction, indicating a duskward shift for the observed case study. 17
1.14 Map of the Mars crustal magnetism observed by MGS at 400 km (Connerney et al., 2005). Pixels are colored by the median value of the radial magnetic field component B_r observed within the 1°× 1°latitude/longitude range represented by the pixel. Colors are assigned in 12 sections spanning two orders of magnitude variation. 19
1.15 Seasons in the Martian orbit. Perihelion is where Mars is closest to the Sun (1.38 AU) and aphelion is where Mars is farthest from the Sun (1.67 AU). The respective seasons (northern winter/southern summer, northern autumn/southern spring, northern summer/southern winter, northern spring/southern autumn) are a result of the Martian tilt. Image credit: NASA/JPL-Caltech. 19

2.1 Schematic diagram of the SWMF and its various physics domains, and computational tools (Gombosi et al., 2021). 28
2.2 Example of simulation reaching steady-state. The BATS-R-US multispecies MHD magnetic field point B_x is sampled at (-2, 0, 0) R_M, and reaches a quasi-steady-state by 30,000 iterations. Though the result is oscillating, B_x is consistent at approximately 6 nT. 30

3.1 Magnetotail current sheet shift under the influence of the crustal magnetic fields and ionosphere. The top row shows the cases under the influence of crustal magnetic fields and the bottom row is without the crustal fields. The purple zeros indicate the magnetotail current sheet. Positive B_x is red and negative B_x is blue. PERMAX: Solar Maximum at Perihelion, APHMAX: Solar Maximum at Aphelion, PERMIN: Solar Minimum at Perihelion, APHMIN: Solar Minimum at Aphelion. 37
3.2 Magnetotail orientation viewed from the tail towards Mars (y-axis is flipped) at a slice of X_{MSO}=-2 R_M from -10 to 10 nT. The top row shows the cases under the influence of crustal magnetic fields and the bottom row is without the crustal fields. Results are shown in the Y_{MSO}-Z_{MSO} plane 2 R_M downtail. 37
3.3 PERMAX and APHMIN cases with changes in the ionization rates for the X_{MSO}-Y_{MSO} (top row) and Y_{MSO}-Z_{MSO} (bottom row) planes. The tail slices are extracted at X_{MSO}=-2 R_M and all results are shown from -15 to 15 nT. These results do not include the crustal sources and the ionization rates were modified by several orders of magnitude until a shift in the magnetotail current sheet was present. Refer to Table 3.2 for specific adjustments in ionization rates. 40
3.4 IMF behavior downtail in the extreme cases. The black dotted line on the APHMIN extreme case indicates Y=0 and the purple dashed lines indicate where the IMF reaches Y=0 on the dawn and dusk side assuming there is no curvature. The IMF slippage in the PERMAX extreme extends beyond the simulation domain, but the slippage in the APHMIN extreme is near 6 R_M. 41
3.5 Multispecies MHD simulation output of the O^+ ion density in $\log_{10}$-scaled particles per cubic centimeter ($\log_{10}(cm^{-3})$) with and without crustal sources. The maximum O^+ values with and without the log scale are as follows - PERMAX: 3.04 $\log_{10}(cm^{-3})$ or 1170 cm^{-3}, APHMAX: 2.79 $\log_{10}(cm^{-3})$ or 628 cm^{-3}, PERMIN: 2.40 $\log_{10}(cm^{-3})$ or 252 cm^{-3}, APHMIN: 2.23 $\log_{10}(cm^{-3})$ or 171 cm^{-3}. . 43
3.6 MHD model comparison of the dawn-dusk (left), nightside (middle), and dayside (right) log-scaled O^+ profiles. The dawn-dusk profile extracts the simulation data for each model along the X_{MSO}=-2 line and is plotted against the Y_{MSO} plane. The nightside and dayside profiles plot the O^+ ion density against altitude. The nightside altitude is reversed to show the behavior of the O^+ ion as it starts downtail and approaches the inner boundary. All simulations show the PERMAX case except the Multifluid MHD simulations from the MAVEN databse, which uses the average Mars-to-Sun distance of 1.5 AU at solar maximum. 45

4.1 Magnetotail current sheet behavior for subsolar longitudes from 0°W to 105°W in 15°increments. Purple zeros indicate where B_x= 0 nT, showing the location of the magnetotail current sheet. At 0°W, the strongest crustal fields (CF) are on the night side. This case also shows that dawn is in the $-Y_{MSO}$ region and dusk in the $+Y_{MSO}$ region. At 90°W, the strongest crustal fields are on the dawn side. 51
4.2 Magnetotail current sheet behavior from 120°W to 225°W. At 180°W, the strongest crustal fields (CF) are located on the dayside. 52

4.3 Magnetotail current sheet behavior from 240°W to 345°W. At 270°W, the strongest crustal fields (CF) are at dusk. 53
4.4 Schematic summary of the magnetotail current sheet location at each subsolar longitude. Blue and red indicate that the magnetotail current sheet is entirely dawnward and duskward, while gray indicates that it transitions between dawn and dusk. 53
4.5 Total current density J for cases where the strongest crustal fields are on the night (0°W), dawn (90°W), day (180°W), and dusk (270°W) sides of Mars. Key structures such as the bow shock, MPB, and magnetotail current sheet have been label on the the 0°W case while dawn and dusk are labeled on the 270 °W case. Current density ranges from 0 to 20 nanoamperes per square meter (nA/m^2). . 54
4.6 Total current density at a downtail slice of $X = -2$ R$_M$. The current density ranges from 0 to 10 nA/m^2. The slice shown here is representative of the current sheet structure shown in Figure 4.5. 55
4.7 Current density heatmap at $= -2$ R$_M$. The x-axis shows the subsolar longitude in degrees west (°W), and the y-axis shows Y_{MSO} from -1 to 1 R_M. The color bar shows the current density from 0 to 0.02 nanoamperes per square meter (nA/m^2). 56
4.8 Schematic summary of the current density structure at each subsolar longitude. Green indicates that the magnetotail current sheet is bifurcated, and purple indicates that it is uniform. 57
4.9 Mass flux ρv at 0°W, 90°W, 180°W, and 270°W. Mass flux is calculated as the product of the total ion density and scalar velocity, with values ranging from 1.0×10^8 to 2.0×10^9 atomic mass units per square centimeter seconds (amu/cm$^2\cdot$s). 58
4.10 Mass flux heatmap slices at $X= -1.5$ R$_M$, $X= -2$ R$_M$, $X= -3$ R$_M$, and $X= -4$ R$_M$. The x-axis represents the subsolar longitude in degrees west (°W), and the y-axis represents the Y_{MSO} coordinate from -1 to 1 R$_M$. Mass flux ranges from 1.0×10^8 to 2.0×10^9 atomic mass units per square centimeter seconds (amu/cm$^2\cdot$s). 59
4.11 Downtail slices of the mass flux at $X= -2$ R$_M$, $X= -3$ R$_M$ and $X= -4$ R$_M$ along the current sheet. 61
4.12 Downtail mass flux slices at $X= -2$ R$_M$, $X= -3$ R$_M$ and $X= -4$ R$_M$ without crustal magnetic fields. 63
4.13 Grid configuration cases simulated at 180°W. For grid structure, resolution, and numerical model options, refer to Table 4.2. 65

5.1 Comparison of the baseline (left column) and logarithmic grid (right column) at the inner (top row) and outer (bottom row) boundaries. Grid blocks and refinement levels are identical for both runs. 71
5.2 Comparison of the baseline (left) and initial refinement (right). X_{MSO} ranges from -4 to 2 R$_M$ and Y_{MSO} from -3 to 3 R$_M$. 72
5.3 Magnetic field in the x-direction for all cases shown in Table 5.2. The magnetotail current is is located where $B_x= 0$ nT, indicated by the purple zeros on each case. 73
5.4 Zoomed in version of Figure 5.3 with a range from -2 to 2 R$_M$. 74

5.5 Magnetic field slice at X=-2 R_M, as seen from the $Y_{MSO} - Z_{MSO}$ plane. The Y_{MSO}-axis is reversed to show the magnetotail current sheet behavior from the tail towards the Sun. 75
5.6 Comparison of B_x from the baseline and Quartey and Liemohn (2025). 76
5.7 Total current density cases in the X_{MSO}-Y_{MSO} plane. Current density ranges from 0 to 20 nanoamperes per square meter (nA/m^2). 77
5.8 Total current density at X=-2 R_M in the Y_{MSO}-Z_{MSO} plane from 0 to 10 nA/m^2. The red square in Case 2 shows where the current is weaker, indicating the location of the bifurcation. 78
5.9 Mesh comparison of the baseline and Quartey and Liemohn (2025) at the inner boundary, mid-range (X_{MSO}=[-4, 2] R_M, Y_{MSO}=[-3, 3] R_M), and the full simulation domain. See Tables 5.1 and 5.3 for the details of the grid settings used in each study. 80
5.10 Magnetotail current sheet comparison of the baseline grid settings and the grid settings of Quartey and Liemohn (2025), rerun here using an updated version of BATS-R-US. PERMAX - solar maximum at perihelion, APHMAX - solar maximum at aphelion, PERMIN, solar minimum at perihelion, APHMIN - solar minimum at aphelion. At -4 R_M, the magnetotail current sheet is shifted in the following ranges (top to bottom): 0 R_M, -0.1 R_M, -0.2 R_M, -0.1 R_M, 0.3 R_M, 0.3 R_M, 0.1 R_M, 0.1 R_M. 81
5.11 Slice of the magnetic field B_x at 2 R_M, plotted in the Y_{MSO}-Z_{MSO} plane. The top and bottom rows show the generalized and the logarithmic grid settings used in Quartey and Liemohn (2025) respectively. See Tables 5.1 and 5.3 for the details of each respective grid configuration. Each column shows a different solar condition (PERMAX, APHMAX, PERMIN, APHMIN). 82
5.12 Comparison of B_x with respect to Y_{MSO} from -2 to 2 R_M, with the line extracted at X=-2 R_M. Lines in blue show the baseline grid configuration and lines in red show the Quartey and Liemohn (2025) grid configuration for PERMAX, APHMAX, PERMIN, and APHMIN. 83

6.1 MAVEN orbit summary plot on 28 May 2017 at 04:22 UTC, obtained from the MAVEN Science Data Center. The top row shows the spacecraft trajectory in the $X_{MSO} - Y_{MSO}$, $X_{MSO} - Z_{MSO}$, and $Y_{MSO} - Z_{MSO}$ planes. The bottom row displays the trajectory in the $X_{MSO} - (Y^2 + Z^2)^{1/2}_{MSO}$ plane (left) and the map projection (right). The rightmost panel shows the 3D image of Mars and a color bar indicating orbit time. The plus symbol in each panel marks the spacecraft location at 04:22 UTC. 87
6.2 MAVEN orbit summary plot on 28 May 2017 at 08:54 UTC. See Figure 6.1 for interpretation of individual panels. 87

6.3 MAVEN orbit combined with MAG measurements on 28 May 2017 from 00:00-4:30 UTC. From top to bottom, the rows show the magnetic field components B_x, B_y, and B_z. From left to right, the columns show MAVEN's orbit trajectory in the $X_{MSO} - Y_{MSO}$ and $X_{MSO} - Z_{MSO}$ planes. The magnetic field is plotted from -15 to 15 nT in all directions, and all distances range from -3 to 3 R_M. The average bow shock (red dotted lines) is taken from Slavin et al. (1982), and MAG data is obtained from NASA's Coordinated Data Analysis Web (CDAWeb). . . 89
6.4 MAVEN orbit combined with MAG measurements on 28 May 2017 from 04:30-09:00 UTC. See Figure 6.3 for details of the plotted data. 90
6.5 BATS-R-US simulation at solar minimum at the subsolar longitude of 120°E, 0°N. The columns correspond to the $X_{MSO} - Y_{MSO}$ and $Y_{MSO} - Z_{MSO}$ planes, and the rows display B_x, B_y, and B_z respectively, plotted from -15 to 15 nT. . . 91
6.6 BATS-R-US simulation at solar minimum at the subsolar longitude of 60°E, 0°N. See Figure 6.5 for details of the plot. 92
6.7 Comparison of the MAVEN pass (blue) in the magnetotail current sheet on 28 May 2017 from 02:15 to 03:15 UTC with BATS-R-US simulation (red) at 120°E, 0°N. The B_x component of the magnetic field is plotted on the y-axis as a function of time along the selected MAVEN orbit segment. The simulation values correspond to a spatial extraction near the modeled current sheet, treated as equivalent to a representative 10-minute interval for comparison. 94
6.8 Comparison of the MAVEN pass in the magnetotail current sheet on 28 May 2017 from 07:10 to 08:10 UTC with BATS-R-US simulation at 60°E, 0°N. See Figure 6.7 for details of the plot. 95

LIST OF TABLES

TABLE

3.1 Table of Neutral Temperature, Neutral Density, Scale Height, and Ionization Rate Profiles at the Different Points of the Solar Cycle and Martian Season . . 36
3.2 Table of Modified Ionization Rates for PERMAX and APHMIN 39

4.1 Peak northern, central, and southern region mass fluxes at 0°W, 90°W, 180°W, and 270°W 62
4.2 Inner boundary grid resolution and model options used in each case study . . . 64

5.1 Baseline configuration settings and corresponding inner boundary grid resolution 69
5.2 Grid configuration adjustments and corresponding inner boundary grid resolution 70
5.3 Grid configuration and corresponding inner boundary resolution from Quartey and Liemohn (2025). 80

LIST OF ACRONYMS

AMR Adaptive Mesh Refinement

APHMAX Solar Maximum at Aphelion

APHMIN Solar Minimum at Aphelion

BATS-R-US Block Adaptive Tree Solar-wind Roe-type Upwind Scheme

CF Crustal Fields

EUV Extreme Ultraviolet

GM Global Magnetosphere

IMF Interplanetary Magnetic Field

MAVEN Mars Atmosphere and Volatile EvolutioN

MGS Mars Global Surveyor

MHD Magnetohydrodynamic

MPB Magnetic Pileup Boundary

MPR Magnetic Pileup Region

MSO Mars-centered Solar Orbital

NASA National Aeronautics and Space Administration

PERMAX Solar Maximum at Perihelion

PERMIN Solar Minimum at Perihelion

SWMF Space Weather Modeling Framework

ABSTRACT

Mars lacks a global intrinsic magnetic field, resulting in a complex induced magnetosphere shaped by its interaction with solar wind. This interaction induces a dawn-dusk asymmetry in the magnetotail current sheet. Spacecraft observations and numerical simulations have been used to study this system, but inconsistencies persist between observations and model predictions, even under nominally identical solar wind conditions. We use the Block Adaptive Tree Solar wind Roe-type Upwind Scheme (BATS-R-US) multispecies magnetohydrodynamic (MHD) code to investigate the physical processes driving the magnetotail current sheet asymmetry and to improve consistency with spacecraft observations.

The first project incorporates seasonal variations driven by planetary eccentricity and solar variability within BATS-R-US. Results examine the influence of crustal magnetic fields and the ionosphere on the magnetotail current sheet asymmetry. **We find that the crustal magnetic fields have significant influence on the asymmetry, while the ionosphere has minimal impact.**

The second project increments Mars in 15° increments in BATS-R-US to determine how the magnetotail current sheet structure evolves over local time. **Results show that the current sheet forms a single layer at local times near dusk but splits into two layers at the equatorial plane at all other local times.**

The third project presents a small-scale grid parameter study using a baseline configurations of standard settings, modifying one parameter at a time to assess how grid resolution influences the magnetotail current sheet structure. We find that the grid geometry has substantial effect on the current sheet shape, whereas grid resolution has minimal influence. The baseline configuration from this investigation is used in the final project in a data-model comparison.

The final project compares the baseline grid configuration from the parameter study to two Mars atmosphere and Volatile EvolutioN (MAVEN) passes on 28 May 2017. Results show encouraging agreement between BATS-R-US simulations and MAVEN observations, demonstrating the ability of the BATS-R-US model to reproduce key features observed in spacecraft data.

These projects demonstrate how the Mars magnetotail current sheet responds to seasonal, longitudinal, and geometric changes within a global multispecies MHD framework. By isolating the drivers of asymmetry, this work provides a clearer physical interpretation of magnetotail structure as captured by numerical models and spacecraft observations. Because atmospheric escape is closely linked to magnetotail dynamics, resolving these structural asymmetries improves our understanding of Mars' atmospheric evolution. More broadly, this work contributes to comparative studies of planetary magnetotails, offering insight into the fundamental processes that shape plasma environments at Mars and other terrestrial planets.

CHAPTER 1

Introduction

1.1 The Sun

The Sun is a magnetized, rotating plasma body that governs the electromagnetic and plasma environment of planetary systems. It has a radius of 6.96×10^5 km, and is located 1.49×10^{11} km, or one astronomical unit (AU) away from the Earth. The solar interior is comprised of three main regions (Figure 1.1):

1. The core
2. The radiative zone
3. The convection zone

The core extends from 0-0.25 solar radii ($R_\odot$) and primarily generates solar energy through nuclear reactions. The radiative zone, spanning 0.25-0.7 $R_\odot$, transmits this energy outward via photons. In the convection zone (0.7-1 $R_\odot$), energy is transported by convective motion; the temperature gradient exceeds the adiabatic gradient, causing plasma to rise and carry energy toward the surface. These interior regions drive the solar outflow that shapes the heliosphere.

The energy transport within the Sun's interior drives the solar dynamo, which converts the solar kinetic energy into electromagnetic energy and generates a powerful magnetic field. The solar dynamo requires an electrically conductive fluid medium, provided by the plasma

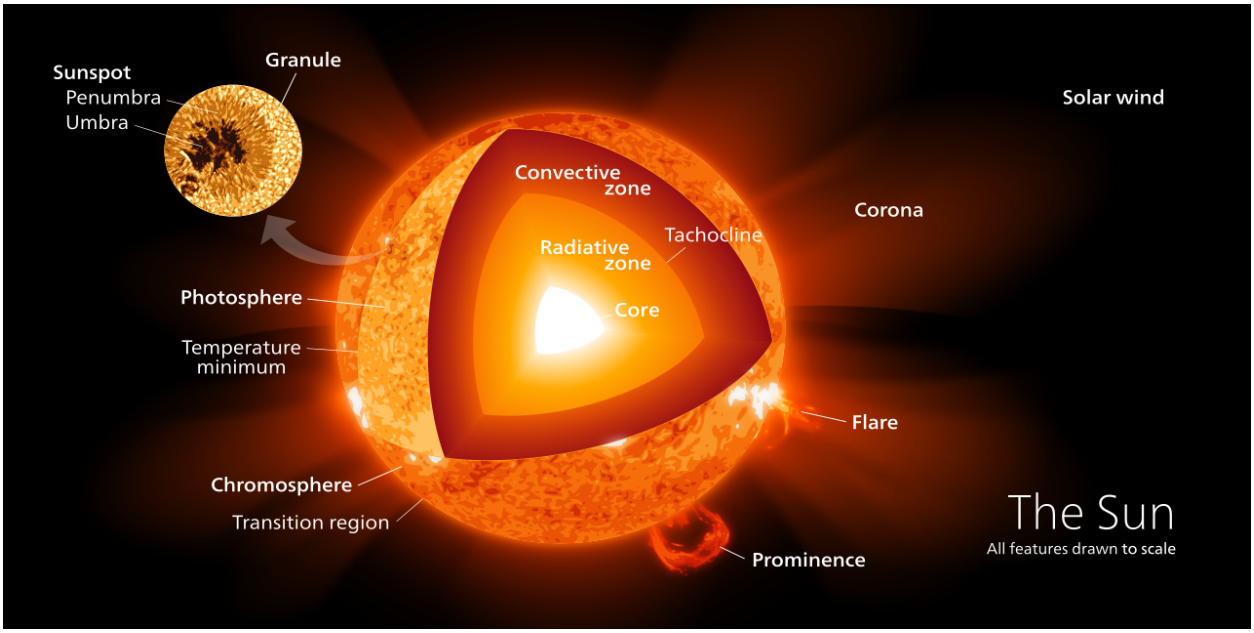


Figure 1.1: Diagram of the interior structure of the Sun including key interior and exterior regions. Image courtesy of Kelvin Song *https://commons.wikimedia.org/w/index.php?curid=23371669*.

in the convection zone. A source of kinetic energy is also necessary, which comes from the Sun's differential rotation. Finally, an internal energy source is needed to sustain convective motion, supplied by the nuclear energy emerging through the radiative zone. These processes interact to sustain the solar dynamo, which generates and sustains the Sun's magnetic field.

1.2 Solar Wind

As plasma flows outward from the Sun, its density decreases as the particles expand into an increasingly large volume, forming the solar wind. Solar wind is a continuous stream of magnetized plasma that originates in the solar corona, the outermost layer of the solar atmosphere. As it flows outward, the plasma carries the magnetic field along with it due to the frozen-in flux condition. This condition means that any two points connected by a field line retain their connectivity, and the magnetic flux through a given surface remains constant even as the surface and shape evolve over time. The magnetic field carried by the

solar wind is known as the interplanetary magnetic field (IMF). As the Sun rotates, the outward flowing plasma stretches the IMF into a spiral pattern known as the Parker spiral (Parker, 1958).

The Parker spiral produces an angle between the magnetic field and radial flow, which becomes more pronounced at larger distances from the Sun (Figure 1.2). Slower solar wind speeds produce a tighter spiral, increasing the azimuthal component of the magnetic field. This angle is important as the orientation of the IMF determines how the solar wind interacts with planetary environments.

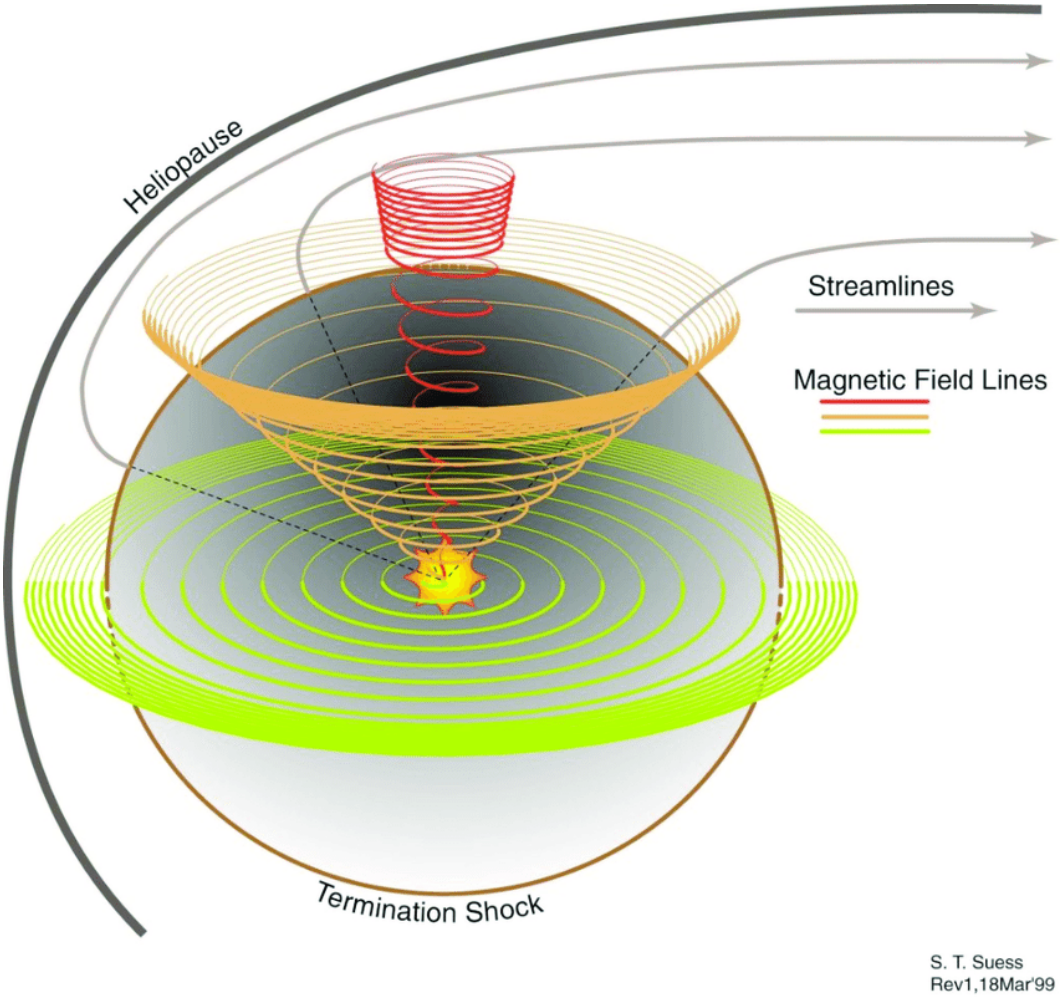


Figure 1.2: Schematic of the Parker Spiral in the heliosphere. Streamlines of solar wind wind drag out the Sun's magnetic field as a result of the frozen-in-flux condition and the Sun's rotation. *Image courtesy of Steve Suess, NASA/MSFC.*

Solar wind escapes primarily through coronal holes, dark regions in the solar corona often found at the poles. These regions are associated with open magnetic field lines, which serve as the source of the high-speed solar wind. Solar wind emerging from coronal holes and open field regions can reach speeds of 800 km/s, and its typically around 400 km/s at closed field regions. The properties of the solar wind also vary over the solar cycle. At solar minimum, when the Sun is least active, slow wind dominates near the ecliptic regions and fast wind dominates near the poles. At solar maximum, when solar activity peaks, fast and slow solar wind coexist at all latitudes, the magnetic field in polar regions becomes highly variable, and solar eruptions create large, coherent structures.

1.3 Planetary Magnetospheres

Solar wind decelerates when it encounters a planetary obstacle. The nature of this interaction depends on whether the obstacle has a large-scale magnetic field, known as the magnetosphere, or a well developed atmosphere and/or ionosphere.

The magnetosphere is a region of space around a planet that is dominated by its magnetic field. Most planets in the solar system possess an intrinsic magnetosphere, generated internally by the planet's internal dynamo which interacts with the solar wind. This magnetic field is generally strong enough to protect the planet from atmospheric erosion and other harmful effects of solar wind (Axford, 1962). Some solar wind can enter through regions such as the planet's cusps, producing phenomena like auroras on Earth, or disturbing the magnetosphere at other planets (Figure 1.3). Solar wind that is deflected by the magnetosphere continues to flow around the planet and out through the magnetotail, the elongated region of the magnetic field behind the planet. Mercury, Earth, Jupiter, Saturn, Neptune, and Uranus all have intrinsic magnetic fields.

Induced magnetotails are formed through atmospheric mass loading and draping of passing magnetosheath flux tubes that sink into the wake. In general, planetary bodies with

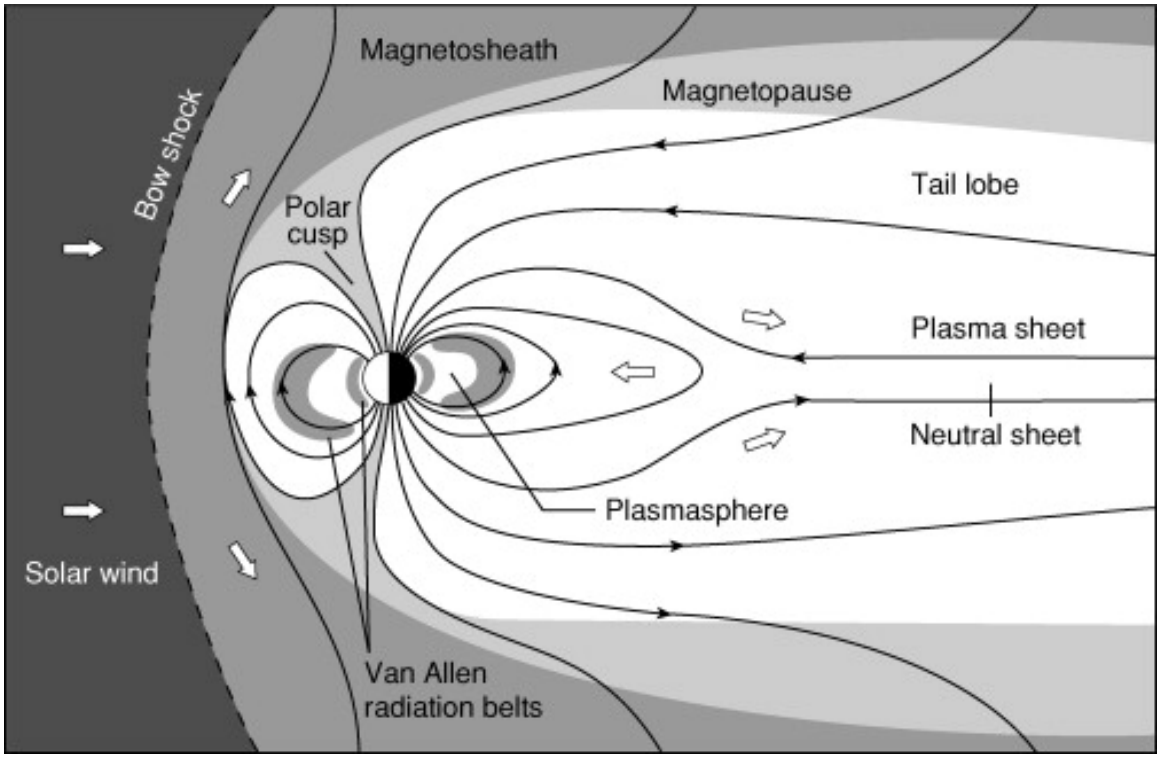


Figure 1.3: Diagram of Earth's intrinsic magnetosphere (Lang, 2005). The bow shock forms near 10 Earth radii on the dayside. The solar wind deflects around the Earth, creating a long magnetotail on the nightside. Solar wind is deflected at the bow shock, flows along the magnetopause into the magnetotail, and is injected back toward the Earth within the plasma sheet.

substantial atmospheres and no intrinsic magnetic field are known to possess cometlike magnetotails.

Venus and Mars do not possess intrinsic magnetospheres. In situ observations of the magnetic field and plasma population at Venus have shown that its magnetic field is induced (Russell et al., 1980; McComas et al., 1986). As it lacks a strong internal dipole field, the draped IMF magnetizes the top layers of the ionosphere to increase the pressure and stand off the dynamic pressure of the oncoming solar wind (Liemohn and Xu, 2018). This magnetization slows the IMF progression, resulting in a draping of the IMF around the planet. The IMF is typically at an angle in this interaction.

The draping effect an IMF angle also influence this behavior at Mars (Luhmann et al.,

1987; Nagy et al., 1990). Without the presence of an internal dynamo, solar wind can impinge directly on the upper atmosphere of Mars, creating a relatively small obstacle in the solar wind flow (Luhmann and Brace, 1991). In situ measurements suggested the presence of a weak intrinsic magnetic field, which can partially shield the nightside atmosphere and prevent magnetotail electrons from precipitating into the ionosphere. The key insights from these observations are summarized as follows (Nagy et al., 2004):

- The bow shock forms upstream of Mars at a distance consistent with MHD models.
- The magnetic pileup region (MPR) is populated by planetary ions. It is separated from the magnetosheath by the magnetic pileup boundary (MPB), a sharp, narrow transition where the solar wind proton density drops significantly and is deflected around the planet.

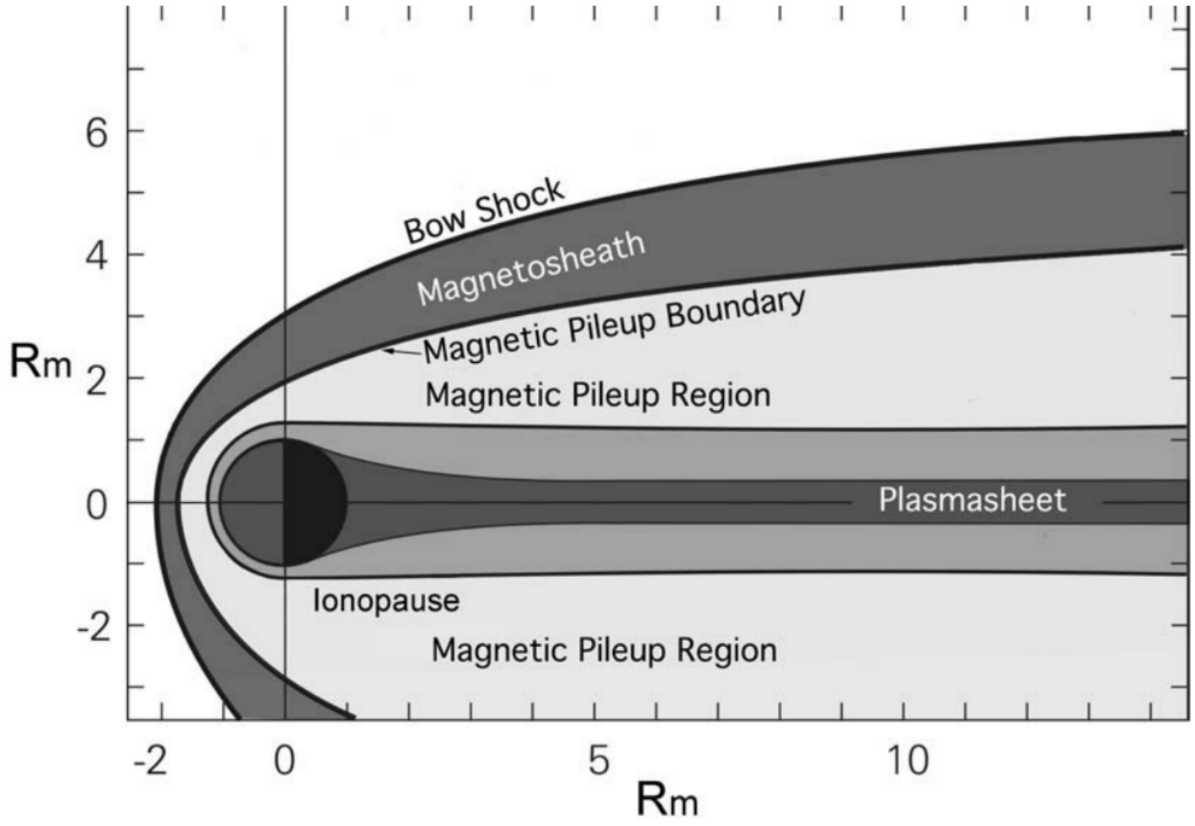


Figure 1.4: Sketch of the structure of the Martian plasma environment, depicting the major boundaries and regions in the equatorial plane (Nagy et al., 2004). R_M - Mars radii.

The magnetic field morphology of the solar wind interaction at Mars is dominated by the draping of the IMF (Figure 1.5). Early understanding of magnetic field draping originated from studies of Venus and comets, starting with Alfvén's theory (Alfvén, 1957). The most detailed observational data on magnetic field draping at Mars comes from MGS, whose elliptical orbit provided coverage across a wide range of altitudes and local times (Crider et al., 2001, 2002).

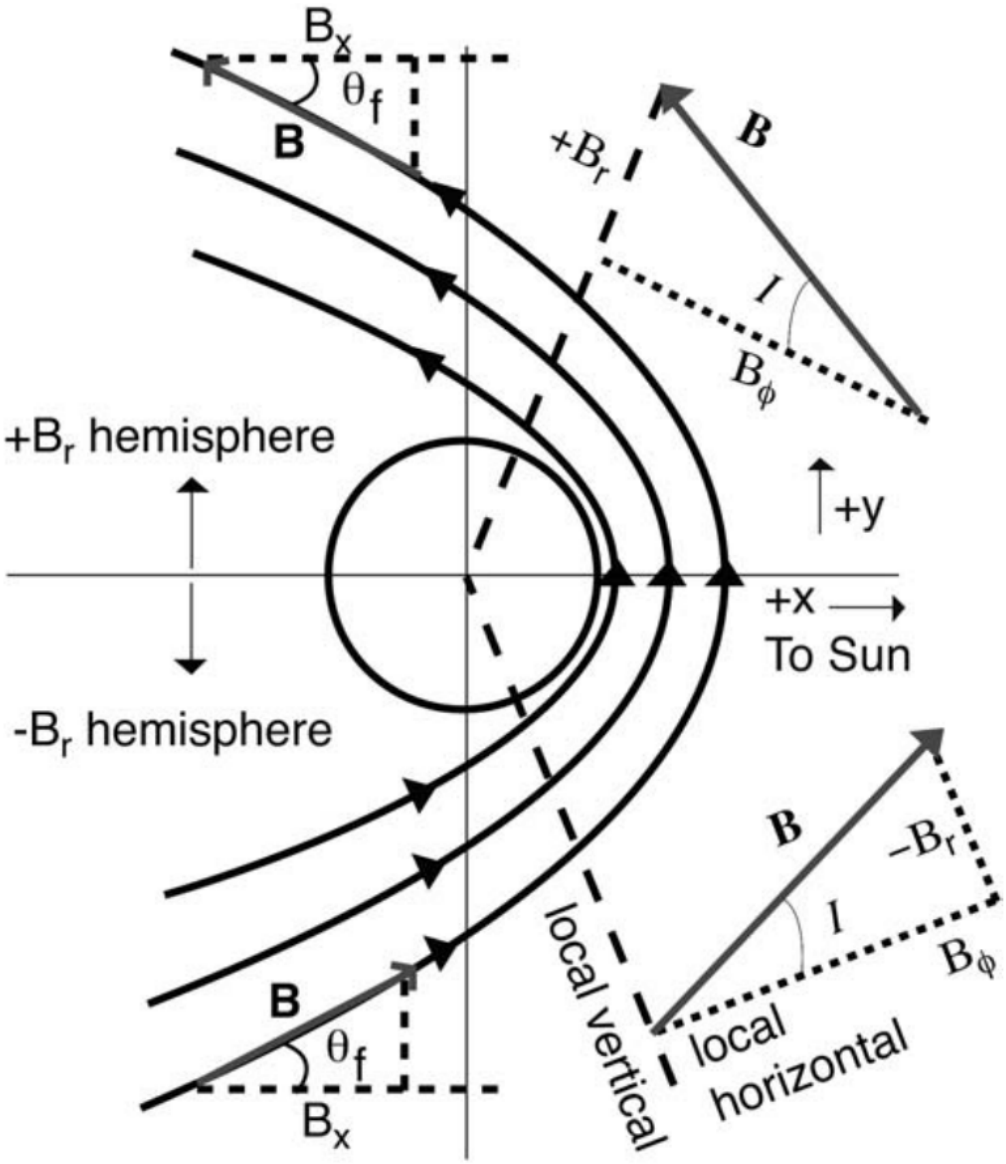


Figure 1.5: Sketch depicting the geometry of draped magnetic field lines at Mars (Nagy et al., 2004). Positive x points towards the Sun (to the right) and positive z points up from the exliptic plane (out of the page).

1.4 The Martian Magnetotail

The interaction of solar wind and a planetary obstacle forms an extended wake known as the magnetotail. This region develops as the solar wind flows around the planet and stretches the magnetic field lines antisunward, producing an elongated structure aligned with the solar wind flow. The magnetotail is key in controlling plasma transport, energy flow, and magnetic topology in planetary space environments.

Early in situ measurements of the Mars demonstrated that the tail is compressible and responds to variations in solar wind dynamic pressure (Vaisberg et al., 1975; Gringauz et al., 1975; Yeroshenko et al., 1990). These observations showed that the Martian magnetotail is structured into two tail lobes, with magnetic fields oriented toward and away from the Sun. The two lobes are separated by a thin current sheet. IMF draping alters the magnetic field direction across different regions of the tail. However, the magnetic field orientation remains relatively stable with respect to the current sheet that separates the two lobes.

1.5 Crustal Magnetic Fields and Planetary Ion Escape

The solar wind interaction at Mars is unique due to the presence of strong localized crustal magnetic fields (Connerney et al., 1999). Analyses of Martian magnetotail boundary crossing indicate that crustal magnetization can influence the location and structure of the magnetotail (Verigin et al., 2001).

The magnetotail is also a key region for planetary ion escape, the process by which ions from the planet's atmosphere are accelerated into deep space, contributing to atmospheric loss over time (Figure 1.14). Because Mars does not have an internal dynamo, planetary ions are stripped from the atmosphere and dragged out with the solar wind (Barabash et al., 2007; Carlsson et al., 2008; Fang et al., 2008; Dubinin et al., 2011; Lundin, 2011). The Martian magnetosphere contains a significant population of planetary ions, primarily dominated by

oxygen ions. Because O^+ and heavier molecular ions (O_2^+, CO_2^+) carry the same charge as the solar wind protons, their escape into deep space cannot be explained by mass alone. Previous studies have suggested that this ion acceleration arises from magnetic field stresses, the the strongest stresses located near the center of the magnetotail (Dubinin et al., 1993).

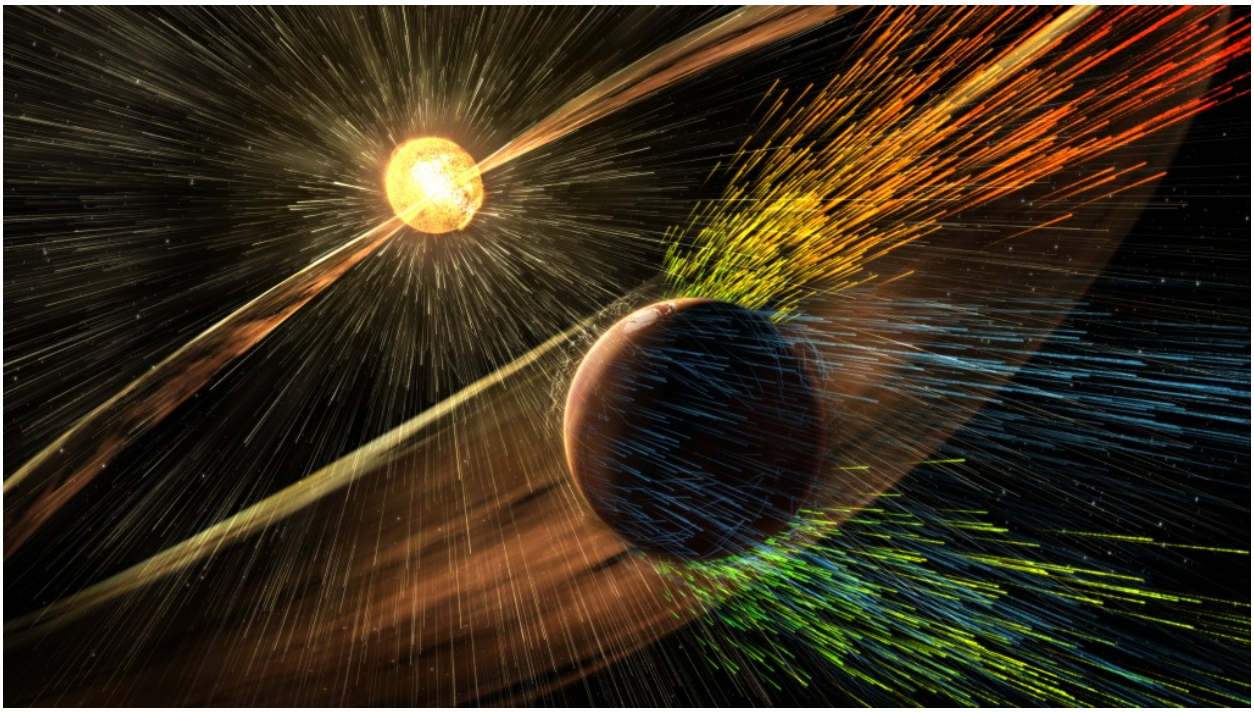


Figure 1.6: Artist depiction of a solar storm hitting Mars, stripping ions from its upper atmosphere. Image credit: NASA Goddard Space Flight Center.

1.6 Magnetotail Current Sheet Asymmetry

Mars exhibits a dawn-to-dusk asymmetry in its magnetotail current sheet region which has been identified in both magnetohydrodynamic (MHD) simulations and satellite observations.

1.6.1 Numerical Simulations

MHD simulations provide valuable insight into the dynamics of the Martian magnetosphere and the evolution of its atmosphere, capturing how the planet interacts with the solar wind under varying conditions. They allow systematic investigation of processes such as current

sheet formation, plasma transport, and magnetotail asymmetries that are difficult to study using satellite observations alone. Key MHD models used to study Martian magnetotail current sheet asymmetry are as follows:

1. Single fluid MHD
2. Multispecies MHD
3. Multifluid MHD

Single-fluid MHD calculations consider the planet as a perfectly conducting sphere embedded in the solar wind. Multispecies MHD models solve separate continuity equations for the solar wind and ionospheric ions, but assume that all ions have the same velocity and temperature Harnett and Winglee (2005). Detailed descriptions of the multispecies MHD model are provided in Chapter 2. Multifluid MHD also uses separate continuity equations, but all ions have individual velocities and temperatures. Below are several published MHD studies that either briefly highlight or cover in depth analyses of the magnetotail current sheet asymmetry.

The Ma et al. (2002, 2004) investigations used the multispecies MHD model, which solves individual densities for each ion species but a single velocity and temperature, to assess the effects of the crustal magnetic fields under nominal solar wind conditions. The largest crustal magnetic fields were pointed sunward (180°longitude), and the magnetotail current sheet region was shifted dawnward (Figure 1.7).

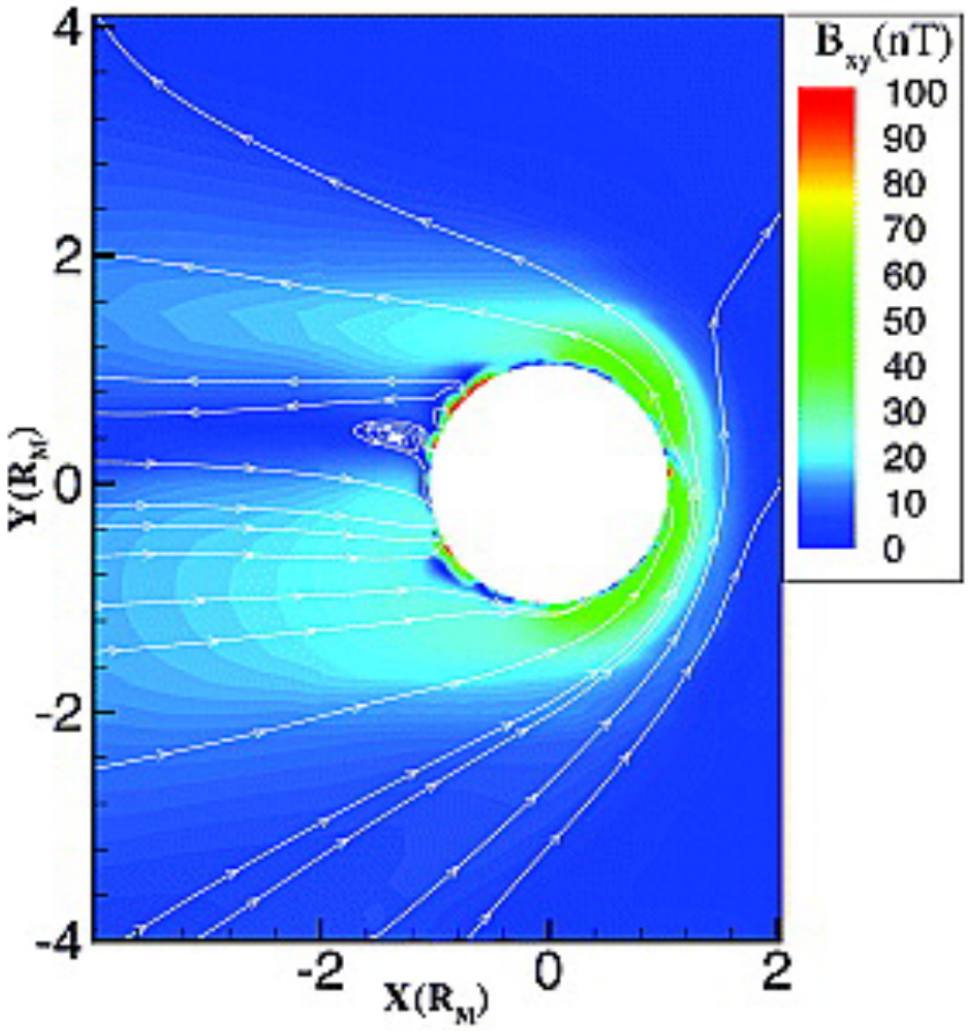


Figure 1.7: Magnetic field component B in the xy plane (Ma et al., 2002). The color plot shows the magnitude and the white lines with arrows indicate the vector direction of the magnetic field. In this figure, the magnetotail current sheet is shifted towards dusk ($+Y$), as this is the region where the magnetic field lobes intersect and are near zero.

Using multispecies MHD, Luhmann et al. (2015) discovered that the magnetic fields were rooted inside the Martian magnetotail, suggesting that the crustal magnetic fields could be

controlling the shape and size of the magnetotail lobes and current sheet. Analysis of the current sheet region revealed a dawnward shift (Figure 1.8).

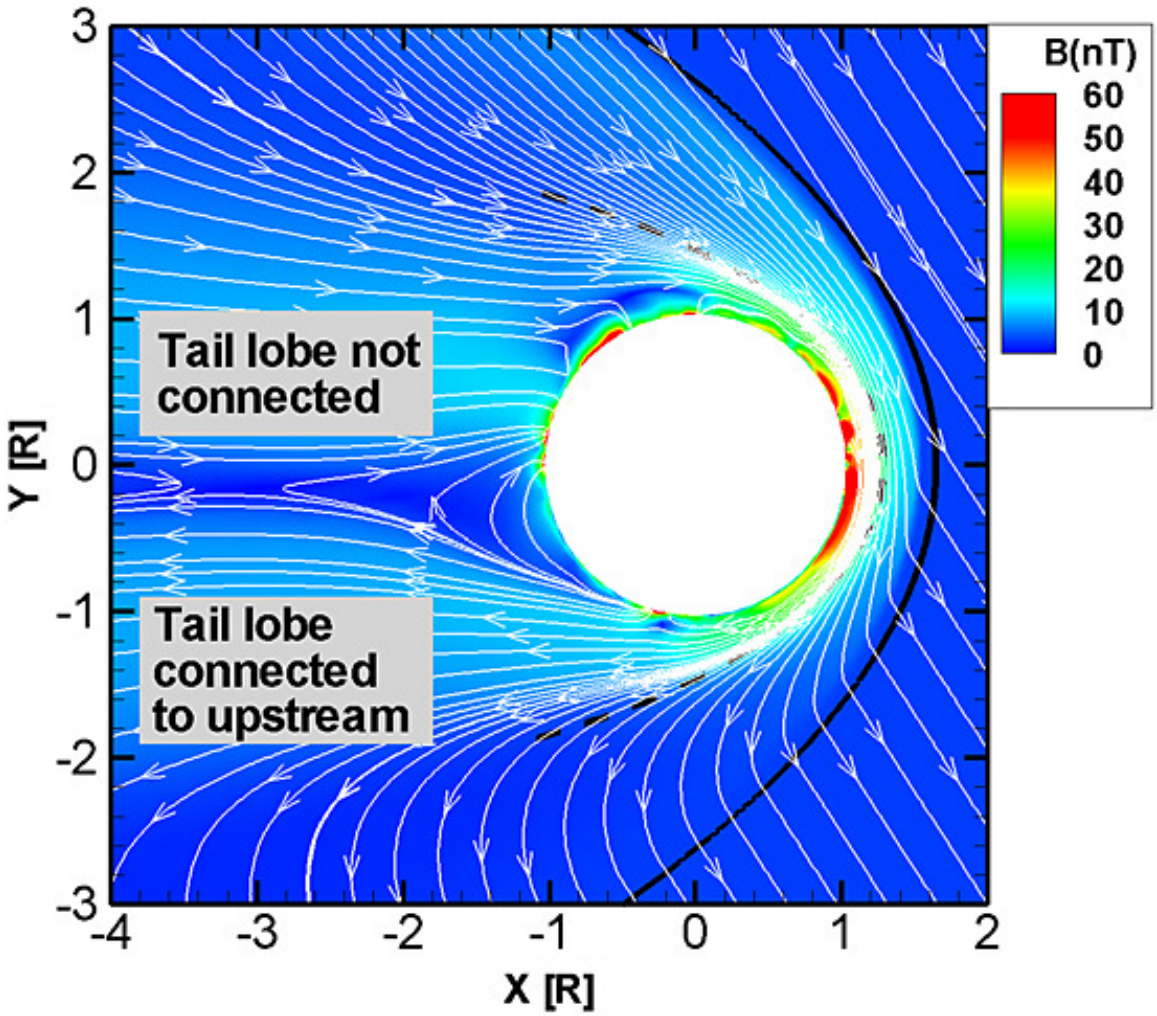


Figure 1.8: Magnetic field lines in the equatorial plane obtained from an MHD simulation of the Mars-solar wind interaction under nominal solar wind conditions and a Parker spiral IMF (Luhmann et al., 2015). The strongest crustal magnetic fields are at noon. The magnetotail current sheet is shifted dawnward.

Li et al. (2013) consisted of a robust current density examination in the tail region using a multispecies MHD code. A key result of this study revealed a well-formed current around the two magnetotail lobes, with the strongest current shifted towards dusk (Figure 1.9).

The multifluid MHD approach, which solves individual densities, velocities, and temperatures for the four major ion species, has also been inconsistent with the direction of the

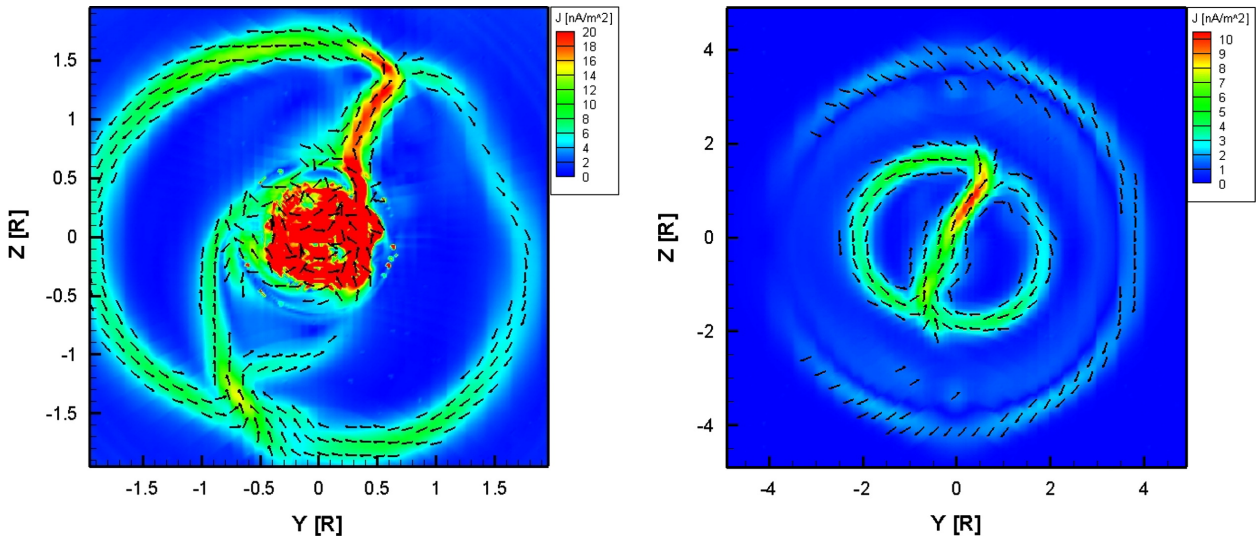


Figure 1.9: Current density J amplitude 1.1 R_M (left) and 2 R_M (right) downtail in the yz plane (Li et al., 2013). The color bar shows the magnitude of the current density and the black arrows show the 2-dimensional component direction in the yz plane.

current sheet shift. Najib et al. (2011) used the multifluid MHD model and found that the decoupling of the individual ions resulted in a dawnward shift of the magnetotail current sheet (Figure 1.10).

Xu et al. (2016) conducted an analysis of pressure and compositional boundaries from multifluid MHD simulation results to identify the pressure structure and composition boundaries at Mars. In the assessment, it was discovered that the magnetotail current sheet was shifted towards dusk. Liemohn et al. (2017) investigated the role of extreme ultraviolet (EUV) intensity at the current sheet by removing the crustal magnetic fields from the multifluid MHD simulation. It was determined that the ionosphere induces a dawnward shift at solar maximum and a duskward shift at solar minimum under the influence of seasons (Figure 1.11).

The differences in the multispecies and multifluid MHD results are not from a systematic difference in the code, as all of these results use the same respective MHD model with different upstream and planetary conditions. However, these results helped determine that location of the crustal magnetic fields and the ionosphere.

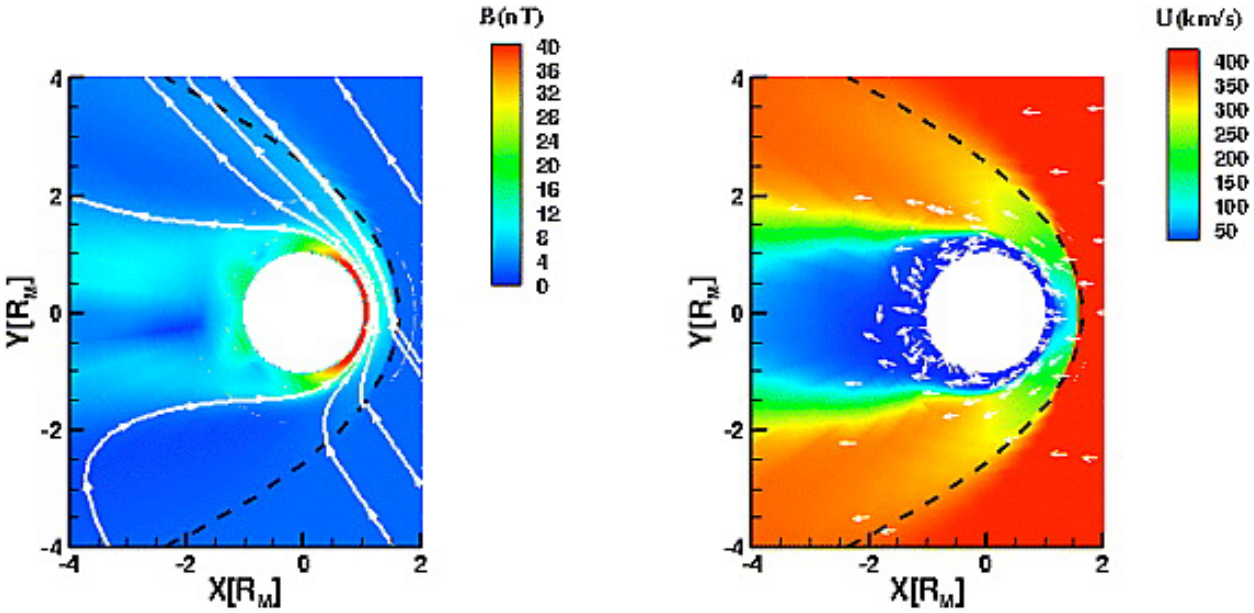


Figure 1.10: Calculated magnetic field (left) and average ion velocity (right) in the equatorial plane for solar minimum conditions (Najib et al., 2011). Color plots show the magnitudes and the white lines with arrows show the vector direction of the magnetic field. White arrows on the ion velocity plot show the direction of the velocity. The black dashed lines represent the mean bow shock location (Vignes et al., 2000). The magnetotail current sheet shifts towards dusk.

Brain et al. (2010) presented a robust comparison of the many numerical models that solve the solar wind interaction at Mars (Figure 1.12). This study was framed as a modeling challenge, and the codes were run with near identical inputs for direct comparison with one another. Two multispecies (Ma et al., 2004; Terada et al., 2009), one multifluid (Harnett and Winglee, 2003), and four hybrid models (Brecht and Ledvina, 2006; Kallio et al., 2008; Modolo et al., 2005; Bößwetter et al., 2004) were run in steady-state. This comparison found that MHD models were characterized by sharp transitions in pressure and ion density near boundaries and that the magnetotail region was a primary pathway for planetary ion escape. Though it was not determined which models are best for specific analyses of the Martian system, it was suggested that MHD models may be more useful for investigating interactions at a high spatial resolution as it is a more straightforward model that is not as computationally expensive as hybrid models. As such, multispecies and multifluid MHD

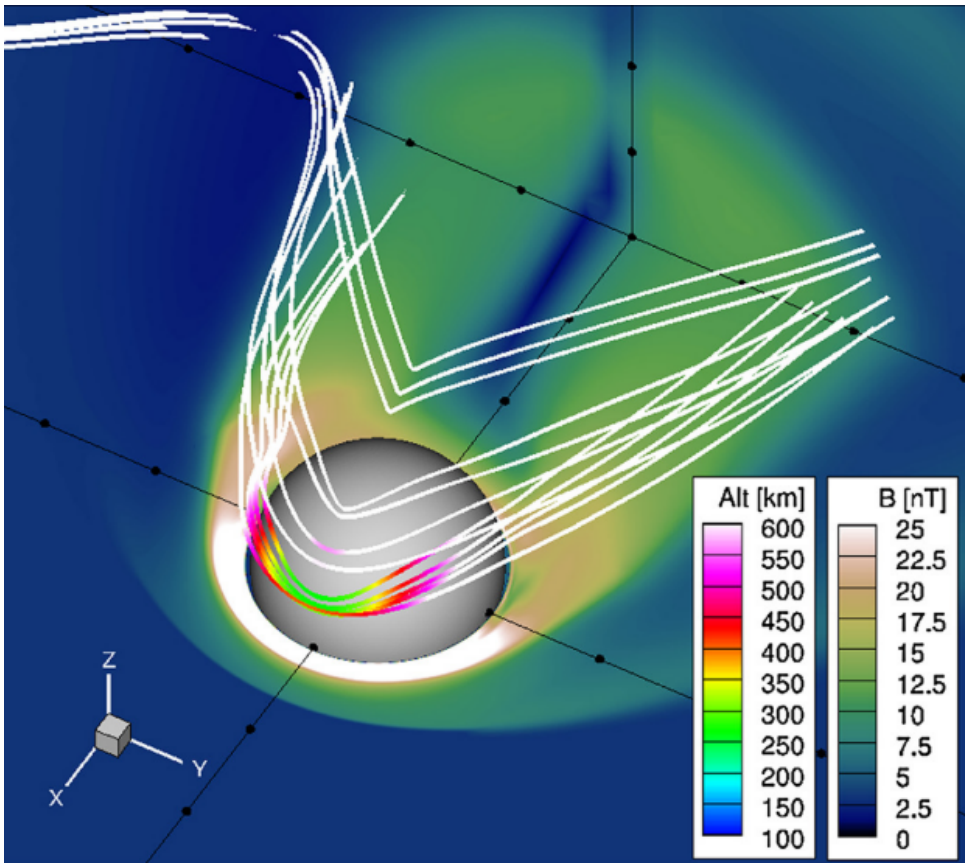


Figure 1.11: Magnetic field B intensity in the equatorial plane and the X=-4 R_M plane (Liemohn et al., 2017). The gray sphere is the surface of Mars, the blue-green-pink color bar represents the altitude and the second color bar represents the magnitude of the magnetic field. The view is from above the ecliptic plane in the afternoon sector with the Sun down and to the left. The dots along each axis are space 1 R_M apart. The magnetotail current sheet is shift towards dawn.

models are often selected to examine the magnetotail current sheet asymmetry.

The role of the seasonal influence on the magnetotail current sheet has not been thoroughly investigated in MHD simulations. This is primarily because numerical models simulate the solar wind interaction at the planet's mean orbital distance of 1.5 astronomical units (AU), overlooking the potential variations introduced by the orbital eccentricity and the seasonal differences associated with perihelion and aphelion.

The crustal field is also known to have a significant effect on planetary ion transport and acceleration. Because of its induced magnetosphere, ions that interact with solar wind

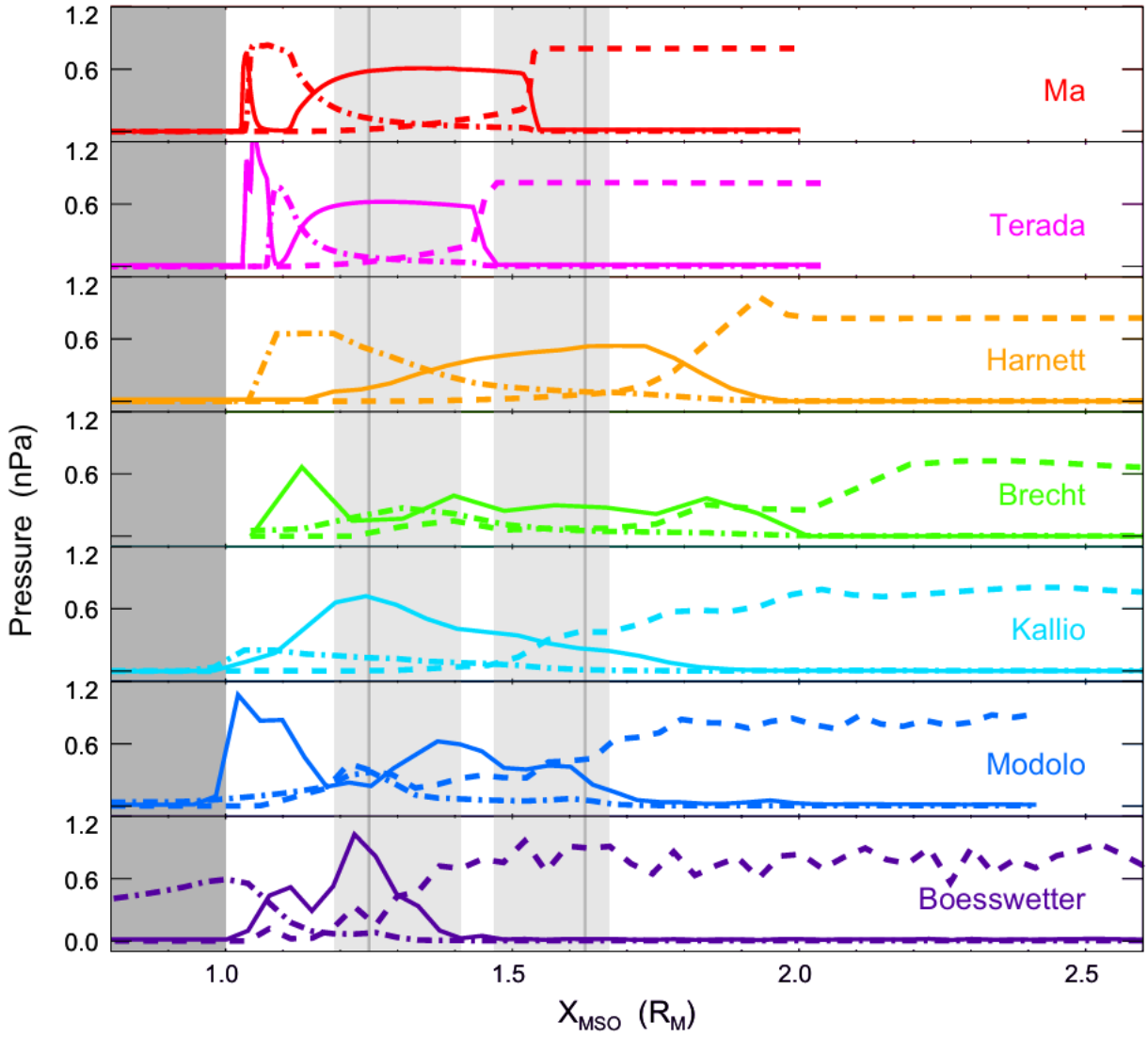


Figure 1.12: Pressure profiles for the seven participating models extracted along the subsolar line (Brain et al., 2010). MHD models are Ma (multispecies), Terada (multispecies), and Harnett (multifluid). Hybrid models are Brecht, Kallio, Modolo, and Boesswetter. Dashed lines indicate dynamic pressure, solid lines indicate plasma thermal pressure, dot-dashed lines indicate magnetic pressure. The darker shaded area in the initial region of the figure indicates regions interior to the planet.

can easily escape the Martian atmosphere. Particles are ionized and accelerated by the solar wind, allowing them to surpass the Martian escape velocity and flow outward into deep space. To understand this exchange, seven global plasma interaction models were compared with one another to observe similarities and differences in each of their results. Two of the models

were MHD models, one was a multifluid model, and four were a hybrid of both models. The MHD models provided very similar results for the subsolar pressure and particle densities while the results of the non-MHD models varied differently, However, the escape rate of the O^+ ions varied across all models. The magnetotail is one of the primary regions for ion outflow, so observations in the region may provide insight into the effect of the crustal field.

1.6.2 Satellite Observations

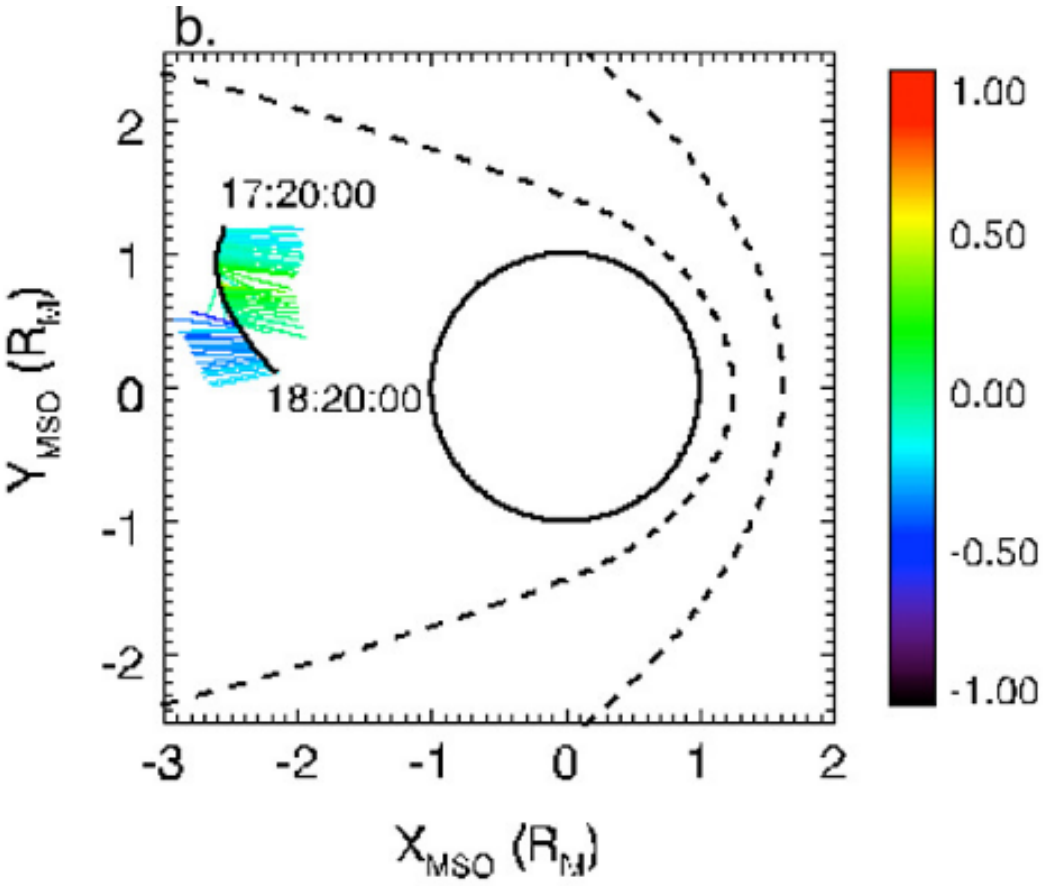


Figure 1.13: Portion of MAVEN's orbit on 5 May 2015 projected onto the equatorial ($X_{MSO} - Y_{MSO}$) plane (DiBraccio et al., 2015). Nominal induced magnetospheric boundary and bow shock positions are indicated by dashed lines. Normalized magnetic field vector projections are plotted along the trajectory where the color represents the normalized out-of-plane component. The color bar represents the magnetic field in the x-direction B_x. The magnetotail current sheet crossing is oriented in the $+Y$ direction, indicating a duskward shift for the observed case study.

The Mars Atmosphere and Volatile EvolutioN (MAVEN) mission was launched in November 2013 and arrived at Mars in September 2014, with a goal of understanding the role that ion loss to space over time has played the planet (Jakosky et al., 2015). DiBraccio et al. (2015) reported on the nature of the Martian magnetotail using magnetic field and plasma measurements from the MAVEN spacecraft (Figure 1.13). The case studies analyzed (1) the repetitive loading and unloading of tail magnetic flux as the field magnitude changed, (2) multiple current sheet crossings indicative of plasma sheet flapping, (3) tailward flowing high-energy planetary ions, and (4) signatures of magnetic flux ropes. Analysis of the current sheet crossings revealed that the magnetotail current sheet was shifted duskward for the observed case study.

1.6.3 Subsolar Longitude

Factors such as current sheet flapping (DiBraccio et al., 2017; Gao et al., 2018; Zhang et al., 2023), atmospheric ion composition (Li et al., 2023), spherical harmonic structure of the crustal magnetic fields (Gao et al., 2021), and the IMF (Romanelli et al., 2018; Nauth et al., 2024; Wang et al., 2024; Wen et al., 2025) have been shown to influence shifts in the magnetotail current sheet. However, the impact of subsolar longitude has not been thoroughly investigated in MHD simulations. Numerical models typically align the largest crustal fields on the dayside (Connerney et al., 2001).

Include a paragraph here about how the subsolar longitude changes with season

1.6.4 Model Grid Resolution

Numerical modeling has played an important role in studies of the solar wind interaction at Mars because it provides insight of plasma and field dynamics that cannot be obtained from sampled spacecraft measurements alone. Such models have been used to investigate a wide range of processes, including magnetic anomalies, IMF behavior (Wang et al., 2025),

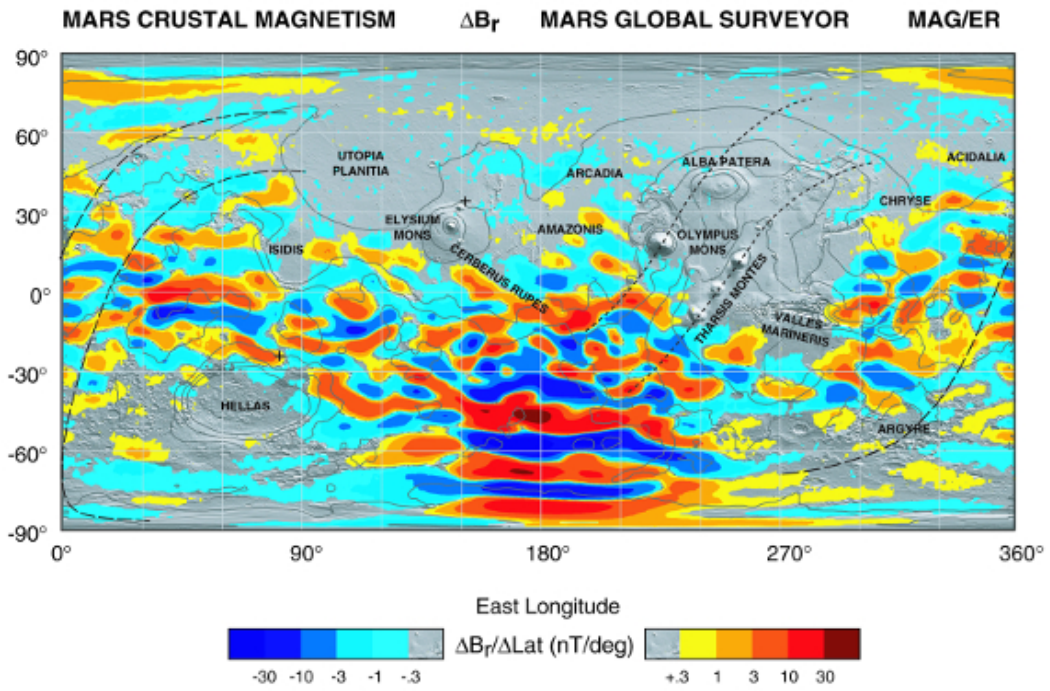


Figure 1.14: Map of the Mars crustal magnetism observed by MGS at 400 km (Connerney et al., 2005). Pixels are colored by the median value of the radial magnetic field component B_r observed within the 1°× 1°latitude/longitude range represented by the pixel. Colors are assigned in 12 sections spanning two orders of magnitude variation.

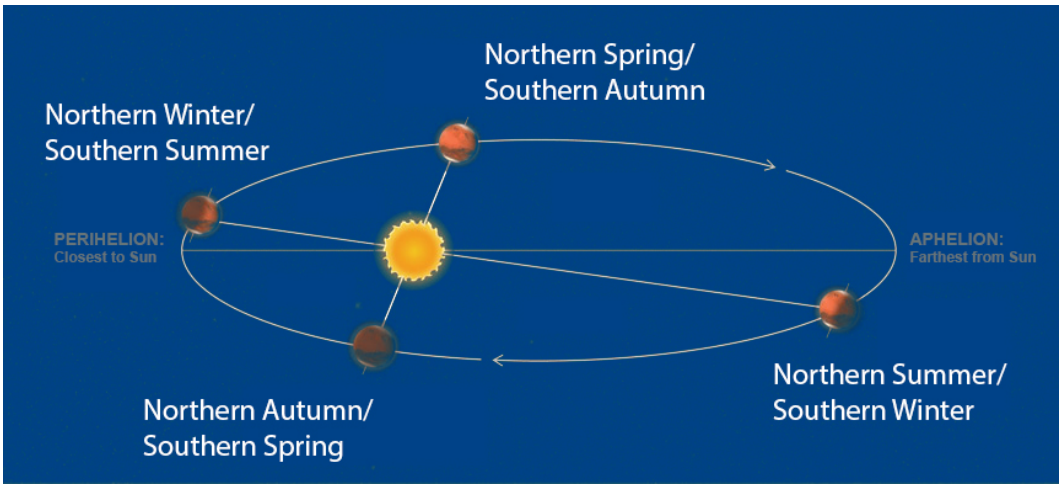


Figure 1.15: Seasons in the Martian orbit. Perihelion is where Mars is closest to the Sun (1.38 AU) and aphelion is where Mars is farthest from the Sun (1.67 AU). The respective seasons (northern winter/southern summer, northern autumn/southern spring, northern summer/southern winter, northern spring/southern autumn) are a result of the Martian tilt. Image credit: NASA/JPL-Caltech.

atmospheric escape (Ma and Nagy, 2007; Ma et al., 2015; Sakata et al., 2020), magnetic pileup (Wang et al., 2023) and crustal magnetic fields (Fang et al., 2010, 2015; Dong et al., 2015; Liemohn et al., 2017; Quartey and Liemohn, 2025).

MHD models generally capture large scale trends observed by spacecraft (Dong et al., 2015; Ma et al., 2015; Ledvina et al., 2017) . But as stated before, there are inconsistencies in data-model comparisons, and different model configurations can produce noticeably different results. Even simulations with identical upstream conditions show significant discrepancies, suggesting that other numerical choices such as grid resolution may influence physical processes. Prior to conducting data-model comparisons, it it essential to assess and identify MHD model configurations to ensure that the simulated results meaningfully represent the physical systems under study.

1.7 Objectives

To summarize, planets in the solar system generate intrinsic magnetic fields that prevent solar wind from impinging on their magnetospheres. Mars is one of the planets that does not have an intrinsic magnetosphere as a result of the Martian core solidification 4 billion years ago. Its induced magnetosphere allows solar wind to interact directly with its upper atmosphere and cause atmospheric ions to escape into deep space via the magnetotail. This interaction also causes the magnetotail current sheet to exhibit a dawn-dusk asymmetry. There is no conclusive answer as to what causes this behavior, but satellite observations and numerical modeling help identify what planetary structures are responsible. MHD simulations typically assess this interaction when the strongest crustal magnetic fields are on the dayside of Mars and assume the planet is at approximately 1.5 AU. However, both solar wind driving and the relative orientation of crustal magnetic fields vary with orbital position and subsolar longitude, potentially influence magnetotail current sheet structure. It is essential to examine how the magnetotail current sheet responds under different orbital configurations

and longitudes in MHD simulations. Before performing comparisons with MAVEN observations, the appropriate model configuration and parameter settings must first be established to ensure that simulated results reliably represent the physical system.

This dissertation aims to improve the MHD numerical model by addressing the following questions:

1. How does the magnetotail current sheet asymmetry under the influence of crustal magnetic fields and ionosphere vary with Martian season?
2. How does the magnetotail current sheet morphology change with subsolar longitude?
3. What grid configuration provides a reliable framework for data-model comparison with MAVEN observations?
4. Do the implemented modifications to the idealized MHD simulations agree with MAVEN observations?

1.8 Dissertation Outline

Chapter 2 provides an overview on the MHD model along with the solar wind conditions and grid configuration used in this work. Chapter 3 investigates how the magnetotail current sheet asymmetry varies with orbital position by implementing seasonal conditions (i.e. perihelion and aphelion) into the numerical model. Chapter 4 examines how the magnetotail current sheet structure evolves with local time by conducting simulations at each Martian local time hour and analyzing the resulting morphological variations. Chapter 5 evaluates the influence of grid configuration on magnetotail current sheet morphology through a grid parameter case study to determine an optimal setup for a data-model comparison with a MAVEN observation. Chapter 6 applies the selected model configuration to a case study of a MAVEN spacecraft pass through the magnetotail current sheet, assessing areas of agreement and disagreement between the simulation and in situ measurements. Finally, Chapter 7 sum-

marizes the key methodologies and finding from all studies, gives insight into the broader implications of this dissertation, and discusses the future work.

CHAPTER 2

Model Description and Numerical Methodology

2.1 Overview

Numerical models provide a global view of planetary plasma environments, helping to frame key scientific questions and offering insight into the physical processes that govern solar wind-planet interactions. As these models rely on different assumptions and levels of simplification, they are useful for assessing the relative importance of the different mechanisms controlling the system.

2.2 Ideal MHD Equations

Ideal MHD has proven effective for studying the solar wind interaction at Mars, largely because of its capability of reproducing key magnetospheric structures. In addition, many processes of interest like the global interaction of the solar wind with the Martian ionosphere and atmosphere are well described by fluid dynamics.

The continuity equation (Eq. 2.1) expresses the conservation of mass in a plasma. It states that the rate of change of mass density of a species ρ_s at a given point in space $\frac{\partial \rho}{\partial t}$ plus the net flux of mass out of the point $\nabla \cdot (\rho_s \mathbf{v})$ must sum to zero. In other words,

any increase in density at a location must be balanced by a net inflow of plasma and any decrease corresponds to a net outflow. This ensures that mass is not created or destroyed as the plasma moves through a system.

$$\frac{\partial \rho_s}{\partial t} + \nabla \cdot (\rho_s \mathbf{v}) = 0 \tag{2.1}$$

The momentum equation (Eq. 2.2) describes how the plasma's motion evolves under the influence of forces. The left-hand side represents the change in the momentum of a plasma element over time and its transport through space. On the right-hand side, the plasma is accelerated by pressure gradients and magnetic forces arising from currents and the magnetic field. In the magnetotail, this equation captures how the combined effects of plasma pressure and magnetic stresses shape the current sheet and control ion motion.

$$\rho \left(\frac{\partial \mathbf{v}}{\partial t} + \mathbf{v} \cdot \nabla \mathbf{v} \right) = -\nabla p + \mathbf{J} \times \mathbf{B} \tag{2.2}$$

The equation of state (Eq. 2.3) assumes plasma evolves adiabatically, meaning no heat is added or removed from a moving plasma element. The ratio stays constant along the motion of plasma meaning it heats up when compressed and cools when expanded.

$$\frac{d}{dt}(\frac{p_s}{\rho_s^{\gamma}}) = 0 \tag{2.3}$$

Electromagnetic fields in ideal MHD are governed by Maxwell's equations. Gauss' Law (Equation 2.4) states that electric fields arise from electric charge density. However, ideal MHD assumes quasi-neutrality, meaning ion and electron densities are nearly equal on macroscopic scales. As a result, the charge density is approximately zero. This implies that large scale electric fields arise from plasma motion across magnetic fields, as described by the ideal Ohm's Law (Eq. 2.5).

$$\nabla \cdot \mathbf{E} = 0 \tag{2.4}$$

$$\mathbf{E} + \mathbf{v} \times \mathbf{B} = 0 \tag{2.5}$$

Gauss' Law for magnetism (Eq. 2.6) states

$$\nabla \cdot \mathbf{B} = 0 \tag{2.6}$$

meaning the magnetic field lines are divergenceless as magnetic monopoles have never been observed. Magnetic field lines will always form continuous closed loops or extend from one region to another without beginning or ending at a point. In other words, magnetic field lines cannot start or stop in space, they must either close back on themselves or connect different regions of a system.

Faraday's Law (Eq. 2.7) states that time varying magnetic fields generate electric fields. The negative sign reflects Lenz's Law, indicating that the induced electric field acts to oppose change in the magnetic field. In ideal MHD, combining Faraday's Law with the ideal Ohm's Law links plasma motion to magnetic field evolution, forming the basis of the induction equation (Eq 2.8).

$$\nabla \times \mathbf{E} = -\frac{\partial \mathbf{B}}{\partial t} \tag{2.7}$$

$$\frac{\partial \mathbf{B}}{\partial t} = \nabla \times (\mathbf{v} \times \mathbf{B}) \tag{2.8}$$

Ampere's Law (Eq. 2.9) states that magnetic fields are generated by electric currents and

time varying electric fields. In ideal MHD, the displacement current is negligible because the plasma is highly conductive. This shows that the magnetic field is directly linked to currents in the plasma and governs how magnetic stresses drive plasma motion and shape structures.

$$\nabla \times \mathbf{B} = \mu_0 \mathbf{J} \tag{2.9}$$

These equations capture the large-scale dynamics of the Martian magnetosphere and magnetotail while providing a basis for interpreting numerical simulations.

2.3 Multispecies MHD

There are many questions of interest that are fluid in their behavior, specifically when addressing the influence of the solar wind interaction on the Martian ionosphere and atmosphere. Simulations in this work use a multispecies, single-fluid MHD model to describe the interaction between the solar wind and the Martian plasma environment. In this framework, the major ion species at Mars, H^+, O_2^+, O^+, CO_2^+, have individual continuity equations, allowing the model to distinguish between solar wind protons and planetary ions. While species densities evolve independently through source and loss processes, all ions share a common bulk velocity and electromagnetic field. The governing equations consist of the mass continuity equation for each species, a single-fluid momentum equation including magnetic forces, the induction equation for magnetic field evolution, and an equation of state relating pressure and density Powell et al. (1999); Ma et al. (2002, 2004). This approach capture large-scale plasma dynamics while retaining compositional effects that are critical for modeling the Martian magnetotail and planetary ion escape.

2.4 Space Weather Modeling Framework

The Space Weather Modeling Framework (SWMF) is a high-performance computational framework designed to model the coupled space environment across multiple physical domains (Gombosi et al., 2002, 2021). It provides a modular architecture in which different physics-based models can be combined to simulate processes spanning a wide range of spatial and temporal scales. These domains include the solar corona, planetary magnetospheres, heliosphere, and ionospheres, allowing researchers to investigate interconnected space weather phenomena within a unified system. The framework supports adaptive mesh refinement (AMR) and massively parallel computation, enabling efficient resolution of both global scale structures and localized plasma processes.

Figure 2.1 shows a schematic diagram of the SWMF and its core models (Gombosi et al., 2021). The SWMF provides high-performance computational capabilities for simulating space weather environments. Its solar/heliosphere models consist of the solar corona, inner heliosphere, solar flares, coronal mass ejections, and solar energetic particles. The magnetosphere domain includes the global magnetosphere, ring current, radiation belts, and plasmasphere. The upper atmosphere components encompass the ionosphere-thermosphere, ionospheric electrodynamics, and polar wind. The SWMF also supports several MHD variants, including ideal, resistive, Hall, multispecies, multifluid, semi-relativistic, and anisotropic formulations, along with several other codes.

The Block Adaptive Tree Solar wind Roe-type Upwind Scheme (BATS-R-US) code is a standalone component of the SWMF capable of simulating the solar wind interaction at Mars (Powell et al., 1999; Tóth et al., 2012). BATS-R-US is a high-performance, generalized MHD code with Adaptive Mesh Refinement (AMR), allowing it to efficiently resolve structure across a wide range of spatial scales. The code can be configured to solve the governing equations of ideal or resistive MHD and supports multispecies and multifluid treatments, making it suitable for modeling planetary ion populations and their interaction with the solar

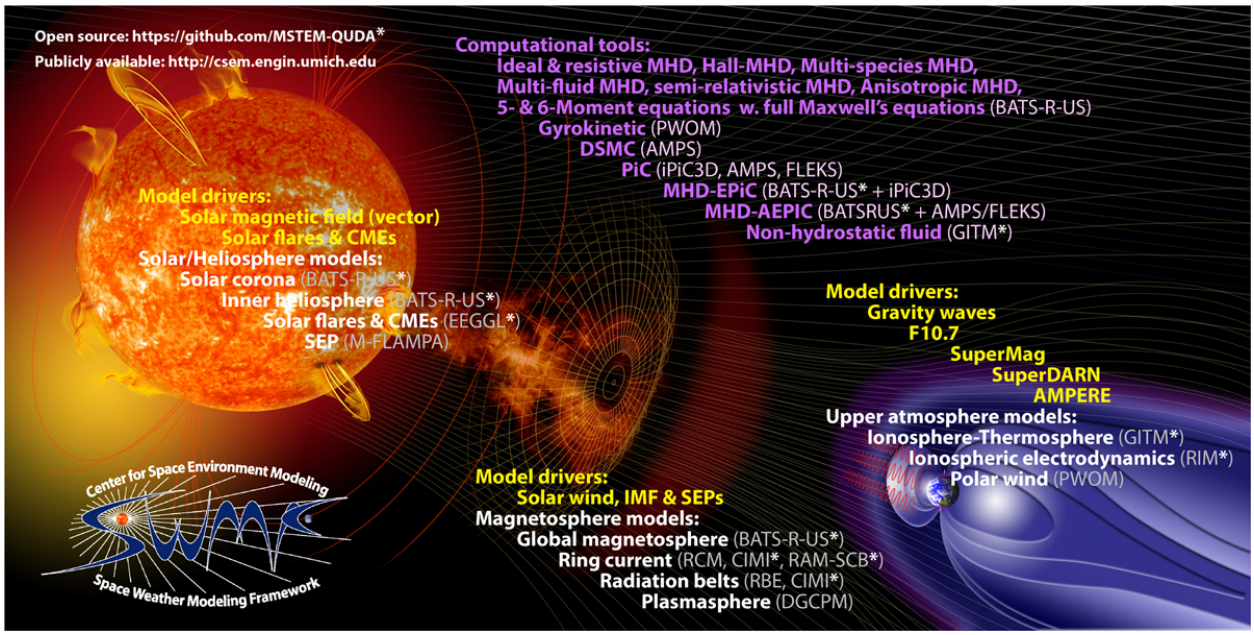


Figure 2.1: Schematic diagram of the SWMF and its various physics domains, and computational tools (Gombosi et al., 2021).

wind. BATS-R-US has been applied to a variety of physics domains, including planetary magnetospheres, the solar corona, and the heliosphere, and provides a flexible framework for coupling with other physics components of the SWMF. The BATS-R-US multispecies MHD code solves individual densities for the major Martian ion species, and all species share a single velocity and temperature. The model uses a 3-dimensional neutral atmosphere and the upper ionosphere is calculated based on photoionization, recombination, electron impact, and charge exchange (Powell et al., 1999; Schunk and Nagy, 2000; Fox and Sung, 2001; Gombosi et al., 2002).

While fully kinetic, hybrid, and multifluid MHD can capture detailed ion-scale physics, multispecies MHD provides a computationally efficient framework that accurate resolves the bulk dynamics of the magnetotail. By tracking the individual densities of H^+, O_2^+, O^+, and CO_2^+ ions while assuming a shared velocity and temperature, the model captures species-dependent effects that influence tail structure and asymmetry. The regions analyzed in this work focus on the large-scale magnetotail current sheet, and this approach sufficiently

resolves the primary drivers of and the Mars-solar wind interaction, allowing to answer the science questions with physical fidelity and tractable simulation times.

2.5 BATS-R-US Configuration

BATS-R-US uses a block-adaptive mesh with either Cartesian or generalized coordinates that include spherical, cylindrical, and toroidal grids (Tóth et al., 2012). The studies in all investigations use a non-uniform spherical grid, with the respective model configuration specified in each chapter.

The inner boundary of the code is set at 100 km altitude, near the bottom of the ionosphere, to simulate the plasma environment around Mars. A computational domain defined by -24 $R_M \leq x \leq 8$ R_M, -16 $R_M \leq y \leq 16$ R_M, -16 $R_M \leq z \leq 16$ R_M, where $R_M = 3396$ km is the radius of Mars, is used in all investigations. The IMF configuration is a 3 nT away sector Parker spiral that approaches Mars at a $\sim 57^\circ$ angle, and the Martian crustal fields are calculated based on the 60-order spherical harmonic model presented in Arkani-Hamed (2001). However, there are more recent maps that use MGS and MAVEN data (Langlais et al., 2019), which may yield better results for a data-model comparison.

The solar wind uses a proton density of 4 cm^{-3}, a velocity of 400 km/s in the negative x-direction, and a temperature of 3.5×10^5 K. Simulations are presented in the Mars-centered Solar Orbital (MSO) coordinate system, where X_{MSO} points from Mars to the Sun, Z_{MSO} is perpendicular to the Martian orbital plane, and Y_{MSO} completes the right-handed system. Simulations are steady-state, meaning Mars is fixated at a subsolar orientation and remains at this position for the entirety of the simulation runtime. Simulations are run for 30,000 iterations, where each iteration consists of solving the governing equation, updating the system state, and recalculating the variables.

Figure 2.2 shows an example of a BATS-R-US multispecies MHD simulation approaching steady-state. A magnetic field test point at (-2, 0, 0) R_M is tracked over 30,000 iterations. Early in the simulation, the magnetic field exhibits significant fluctuations. By 10,000 iterations, it stabilizes near 6 nT. Beyond this point, the magnetic field value oscillates slightly about this value through 30,000 iterations.

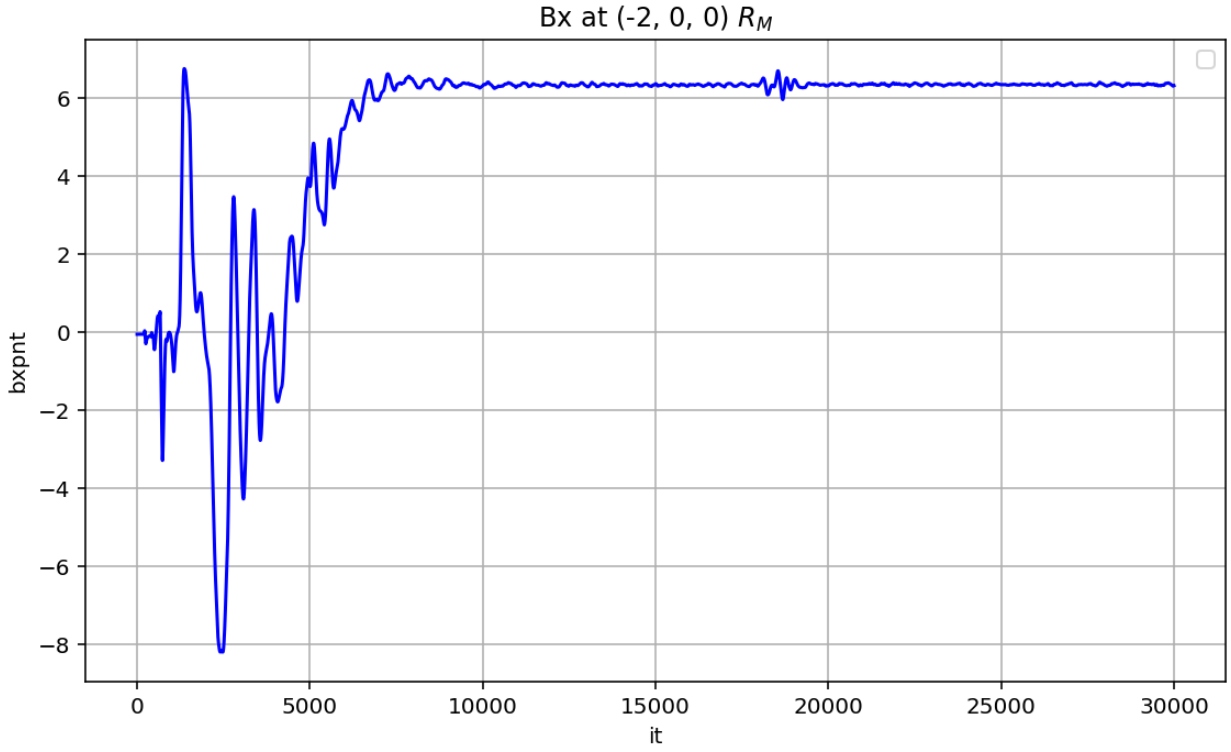


Figure 2.2: Example of simulation reaching steady-state. The BATS-R-US multispecies MHD magnetic field point B_x is sampled at (-2, 0, 0) R_M, and reaches a quasi-steady-state by 30,000 iterations. Though the result is oscillating, B_x is consistent at approximately 6 nT.

CHAPTER 3

Multispecies MHD Simulations of the Crustal Field Influence at the Mars Magnetotail Current Sheet

This chapter was published in *Journal of Geophysical Research: Space Physics* on 23 April 2025 (Quartey and Liemohn, 2025)

3.1 Introduction

The induced magnetosphere of Mars causes the IMF to interact directly with the upper atmosphere. This causes two lobes of opposite magnetic field strengths to form behind the planet. A current sheet forms at the region where the tail lobes intersect, allowing planetary ions to escape from the Martian atmosphere.

Several factors, including the IMF orientation, crustal magnetic fields, magnetic field structure, atmospheric ion escape, planetary rotation, and Martian season (e.g. perihelion and aphelion), are believed to influence the magnetotail current sheet shift. Despite these insights, the role of the seasonal influence on the current sheet has not been thoroughly investigated in MHD simulations. This is primarily because numerical models simulate the solar wind interaction at the planet's mean orbital distance of 1.5 AU, overlooking the potential variations introduced by the orbital eccentricity and the seasonal differences

associated with perihelion (1.38 AU) and aphelion (1.67 AU).

This investigation implements season in the multispecies MHD code. Because of the eccentricity of Mars's orbit around the Sun, which causes a ∼50% change in the solar photon flux reaching the planet (Peter et al., 2024), solar photon flux can affect the modeled structure of the Mars space environment. Previous studies have examined aspects of this, but not the full combination of season, solar cycle, and crustal field influences. Several simulations are presented to examine the behavior of the current sheet with and without the crustal sources to determine the impact that the crustal magnetic fields and ionosphere have on the current sheet.

3.2 Solar Condition Numerical Methodology

As stated in Chapter 2, the BATS-R-US inner boundary is set at 100 km altitude, near the bottom of the ionosphere, to simulate the entire plasma environment around the planet. The spherical grid ranges from the inner boundary to 8 R_M upstream, 24 R_M downstream, and 16 R_M on each side. The IMF configuration is a 3 nT away sector Parker spiral and the Martian crustal fields are calculated based on the 60-order spherical harmonic model presented in Arkani-Hamed (2001). The solar wind uses a proton density of 4 cm^{-3}, a velocity of 400 km/s in the negative x-direction, and a temperature of 3.5×10^5 K. The planet is fixated at a subsolar position of 180°W, 0°N, so the strongest crustal fields are oriented on the dayside of Mars (Acuña et al., 1999; Connerney et al., 2001). The simulations are run for 30,000 iterations to obtain a steady-state solution, meaning all quantities do not change with time (see Figure 2.2).

Table 3.1 shows the standard neutral temperature, neutral density, scale height, and ionization rate profiles present in the multispecies MHD code at solar maximum (Solar Max) and solar minimum (Solar Min). In the neutral density and scale height profiles, several ion species are followed by an x, h, or hx after their name. This indicates the location of the ion

species in the Martian atmosphere with x portraying the ion as it enters the hot exosphere, h representing the ion as it is inside the exosphere, and hx indicating the ion as it reaches the outer limit of the hot exosphere. The values presented in the table were modified to create new profiles that simulate the solar wind interaction at Mars with the solar cycle and season. The equations used to implement seasons within the multispecies MHD code are presented below. The surface area from the Sun to Mars is calculated using $4\pi r^2$, where r is the average distance between the two planetary bodies. Mars has an eccentric orbit, so the Mars-to-Sun varies depending on whether the planet is at perihelion or aphelion. To introduce seasons in the multispecies MHD code, the surface area at the average Mars-to-Sun distance was divided by the surface area at perihelion and aphelion respectively. These solutions are called R_P and R_A.

$$R_P = (1.5 \text{ AU})^2/(1.38 \text{ AU})^2 \tag{3.1}$$

$$R_A = (1.5 \text{ AU})^2/(1.67 \text{ AU})^2 \tag{3.2}$$

At 1.5 AU, the neutral temperature, neutral density, scale height, and ionization rate profiles vary depending on whether the Sun is at solar maximum or solar minimum. The difference between the solar maximum (y_{max}) and solar minimum (y_{min}) profiles is taken. A linear difference could yield negative solutions if the solar minimum variable is greater than the solar maximum variable, so a logarithm is used for the difference. This difference is called D.

$$D = \log_{10}(y_{max}/y_{min}) \tag{3.3}$$

The difference D is multiplied by the respective ratios R_P and R_A. These terms are called

S_P and S_A.

$$S_P = R_P * D \tag{3.4}$$

$$S_A = R_A * D \tag{3.5}$$

A delta term is created from these solutions. Subtracting the seasons S_P and S_A by the difference D returns two delta terms at perihelion and aphelion ΔP and ΔA. If the solar maximum value exceeds the solar minimum value, the delta term is positive; otherwise, delta is negative.

$$\Delta P = \pm(S_P - D) \tag{3.6}$$

$$\Delta A = \pm(S_A - D) \tag{3.7}$$

The delta term is incorporated into the initial y_{max} and y_{min} variables to establish seasons within the multispecies MHD code. Since a logarithm was used for the difference, y_{max} and y_{min} variables are log scaled. These terms are added or subtracted with the ΔP and ΔA terms and taken with respect to powers of ten. The final equations are presented below with the following variable names: P_{max} - solar maximum at perihelion, A_{max} - solar maximum at perihelion, P_{min} - solar maximum at perihelion, A_{min} - solar maximum at perihelion.

$$P_{max} = 10^{(log_{10}(y_{max}) \pm \Delta P)} \tag{3.8}$$

$$A_{max} = 10^{(log_{10}(y_{max})\pm\Delta A)} \tag{3.9}$$

$$P_{min} = 10^{(log_{10}(y_{min})\pm\Delta P)} \tag{3.10}$$

$$A_{min} = 10^{(log_{10}(y_{min})\pm\Delta A)} \tag{3.11}$$

Table 3.1 includes the neutral temperature, neutral density, scale height, and ionization rate profiles for the new profiles created with these equations. From left to right, the columns display the profiles for Solar Max, solar maximum at perihelion (PERMAX), solar maximum at aphelion (APHMAX), Solar Min, solar minimum at perihelion (PERMIN), and solar minimum at aphelion (APHMIN). The hydrogen ion scale height does not vary regardless of the solar condition because the formulation used to compute it yields the same value in each case.

3.3 Results

3.3.1 Crustal Field Influence

Figure 3.1 presents simulation results for the four cases PERMAX, APHMAX, PERMIN, and APHMIN with and without the crustal sources. Each figure shows the magnetic field in the x-direction B_x from -15 to 15 nT where red and blue indicate the positive and negative B_x respectively. The results are presented in the Mars-centered Solar Orbital (MSO) coordinates, where X_{MSO} points from Mars toward the Sun, Z_{MSO} is perpendicular to the Martian orbital plane, and Y_{MSO} completes the right-handed system. X_{MSO} ranges from -3 to 1 R_M and Y_{MSO} ranges from -2 to 2 R_M. The top row of figures indicates the simulation results containing the crustal magnetic fields at the subsolar position of 180°W, 0°N and the bot-

Table 3.1: Table of Neutral Temperature, Neutral Density, Scale Height, and Ionization Rate Profiles at the Different Points of the Solar Cycle and Martian Season

	Solar Max	**PERMAX**	**APHMAX**	**Solar Min**	**PERMIN**	**APHMIN**
Neutral Temperature (K)	134	137.3	130.5	117	119.9	114
			Neutral Density (cm $^{-3}$)			
CO_2	4.43×10^{12}	5.66×10^{12}	3.42×10^{12}	1.16×10^{12}	1.48×10^{12}	8.94×10^{11}
O	8.03×10^{9}	9.47×10^{9}	6.73×10^{9}	3.23×10^{9}	3.81×10^{9}	2.71×10^{9}
H	1.84×10^{6}	1.32×10^{6}	2.61×10^{6}	1.13×10^{7}	8.13×10^{6}	1.61×10^{7}
Oh	6.31×10^{4}	7.81×10^{4}	5.03×10^{4}	1.95×10^{4}	2.41×10^{4}	1.56×10^{4}
Ohx	3.96×10^{3}	4.71×10^{3}	3.30×10^{3}	1.52×10^{3}	1.81×10^{3}	1.27×10^{3}
Hx	7.36×10^{4}	1.17×10^{5}	4.49×10^{4}	9.49×10^{5}	1.51×10^{6}	5.79×10^{5}
Ox	5.17×10^{8}	5.19×10^{8}	5.15×10^{8}	5.27×10^{8}	5.28×10^{8}	5.24×10^{8}
CO_2x	8.08×10^{10}	9.71×10^{10}	6.65×10^{10}	2.22×10^{11}	2.67×10^{11}	1.83×10^{11}
			Scale Height (km)			
O	13.34	14.19	12.49	9.49	10.09	8.88
Ox	50.02	54.74	45.45	30.45	33.32	27.66
Oh	290.5	290.5	290.5	290.5	290.5	290.5
Ohx	2436.6	2436.6	2436.6	2436.6	2436.6	2436.6
CO_2	6.56	6.83	6.29	5.27	5.48	5.05
CO_2x	17.06	18.63	15.55	10.53	11.50	9.60
H	13.13	13.13	13.13	13.13	13.13	13.13
Hx	610.0	614.3	605.4	586.6	590.8	582.2
			Ionization Rate (s^{-1})			
$CO_2 + h\nu \rightarrow CO_2^+ + e^-$	7.30×10^{-7}	8.89×10^{-7}	5.92×10^{-7}	2.47×10^{-7}	3.01×10^{-7}	2.00×10^{-7}
$O + h\nu \rightarrow O^+ + e^-$	2.73×10^{-7}	3.35×10^{-7}	2.20×10^{-7}	8.89×10^{-8}	1.09×10^{-7}	7.16×10^{-7}
$H + h\nu \rightarrow H^+ + e^-$	8.59×10^{-8}	9.29×10^{-8}	7.90×10^{-8}	5.58×10^{-8}	6.03×10^{-8}	5.13×10^{-8}

tom row of figures does not include the crustal magnetic fields. Figure 3.2 shows simulation results of the magnetotail 2 R_M downtail in the Y_{MSO}-Z_{MSO} plane. These simulation results range from -3 to 3 R_M and present B_x from -10 to 10 nT.

At solar maximum, the magnetotail current sheet exhibits a duskward ($+Y$) shift. The current sheet in the PERMAX and APHMAX cases is initially near the Y=0 region at the inner boundary but shifts towards dusk as it moves further downtail. At solar minimum, the current sheet exhibits a dawnward ($-Y$) shift. Like the solar maximum simulations, it is initially near Y=0 for PERMIN and APHMIN but shifts towards dawn as it extends further downtail. When the crustal sources are removed from the simulation, the solar wind interaction at Mars remains realistic but is driven solely by the ionosphere. In these cases, the magnetotail current sheet remains symmetric along the Y=0 plane. The changes in the solar cycle and season do not appear to change the behavior of the current sheet.

Simulations including crustal magnetic fields exhibit a duskward shift. In Figure 3.2, the

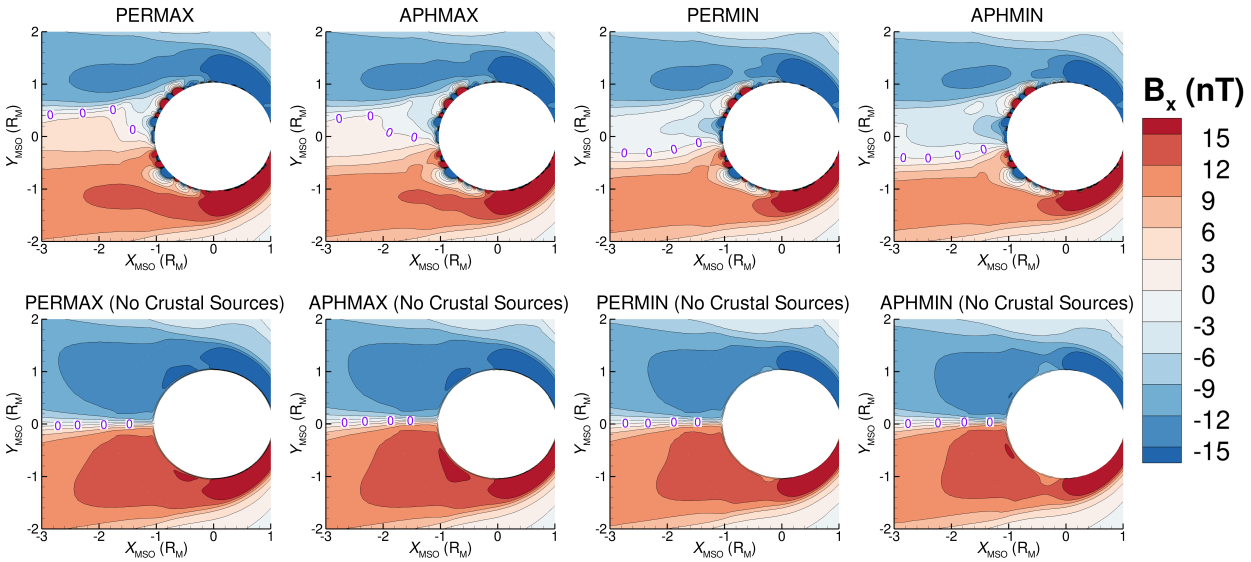


Figure 3.1: Magnetotail current sheet shift under the influence of the crustal magnetic fields and ionosphere. The top row shows the cases under the influence of crustal magnetic fields and the bottom row is without the crustal fields. The purple zeros indicate the magnetotail current sheet. Positive B_x is red and negative B_x is blue. PERMAX: Solar Maximum at Perihelion, APHMAX: Solar Maximum at Aphelion, PERMIN: Solar Minimum at Perihelion, APHMIN: Solar Minimum at Aphelion.

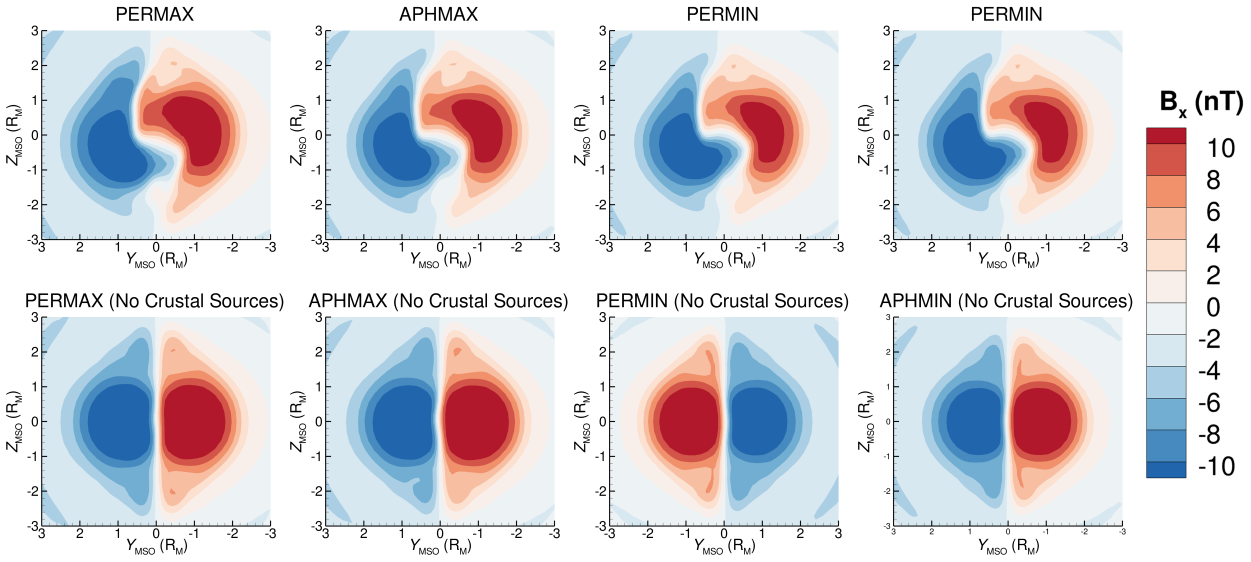


Figure 3.2: Magnetotail orientation viewed from the tail towards Mars (y-axis is flipped) at a slice of X_{MSO}=-2 R_M from -10 to 10 nT. The top row shows the cases under the influence of crustal magnetic fields and the bottom row is without the crustal fields. Results are shown in the Y_{MSO}-Z_{MSO} plane 2 R_M downtail.

magnetotail exhibits a twist in simulation with crustal sources. The current sheet shifts in the $+Y$ direction when located in the $+Z$ hemisphere and in the $-Y$ direction in the $-Z$ hemisphere, consistent with observations from DiBraccio et al. (2015, 2018, 2022). These studies analyzed thousands of MAVEN orbits to quantify the degree of magnetotail twisting and assess variations in response to crustal field location, Martian season, and downtail distance. It was discovered that the crustal field orientation presented ideal conditions for magnetic reconnection to occur, and a greater twist was observed at greater downtail distances. In the absence of crustal magnetic fields, the magnetotail remains symmetric.

Since the magnetotail current sheet in the non-crustal simulations does not exhibit a dawn-to-dusk asymmetry, it is concluded that the crustal magnetic fields exhibit more control over the shift of the current sheet than the ionosphere. The consistent lack of variation in the current sheet across all cases suggests that the ionosphere has a minimal impact on the asymmetry of the shift, which differes from the conclusion of one multifluid MHD study. Liemohn et al. (2017) investigated the current sheet behavior for the same simulation cases using the BATS-R-US multifluid MHD code without crustal sources. The results from that investigation showed that the ionosphere induces a systematic asymmetry in the magnetotail current sheet region, causing it to shift dawnward or duskward depending on the simulation case. The differences between the multispecies and multifluid simulations are presented in Section 3.3.4. While this study focuses on steady-state simulations, it should be noted that altering planetary rotation could influence magnetotail current sheet asymmetries. Time-dependent effects associated with rotation are not explored due to the computational cost of time-accurate simulations, and thus the potential impact of rotation remains an open question for future work.

3.3.2 Extreme Ionization Rates

Given that the magnetotail current sheet did not shift in cases without crustal sources, the next step is to assess whether ionization rates within the multispecies MHD code drive this

shift. This approach was selected because previous studies have shown that variations in ionization rates can influence the strength of the magnetosphere (Dong et al., 2014; Ma et al., 2015). This motivates an examination of whether ionization rates can also influence the magnetotail current sheet asymmetry. The ionization rates within the multispecies MHD code are adjusted by several orders of magnitude to determine what ionization rates cause the magnetotail current sheet to shift. For these simulations, the solar cycle and seasonal extremes PERMAX and APHMIN are the only cases presented. These simulations do not include the crustal magnetic fields.

Table 3.2: Table of Modified Ionization Rates for PERMAX and APHMIN

	PERMAX	PERMAX EX	APHMIN	APHMIN EX
$CO_2 + h\nu \rightarrow CO_2^+ + e^-$	8.89×10^{-7}	8.89×10^{-3}	2.00×10^{-7}	2.00×10^{-16}
$O + h\nu \rightarrow O^+ + e^-$	3.35×10^{-7}	3.35×10^{-3}	7.16×10^{-7}	7.16×10^{-16}
$H + h\nu \rightarrow H^+ + e^-$	8.59×10^{-8}	8.59×10^{-4}	5.13×10^{-7}	5.13×10^{-17}

Table 3.2 lists the ionization rates in the multispecies MHD source code and the changes made to the ionization rates. These are the only parameters changed within the multispecies MHD code. The leftmost column displays the ionization reactions and the initial ionization rates in the source code are shown in the following column in ions per second (s^{-1}). The values in this column resulted in the symmetric magnetotail current sheet seen in Figure 3.1. The PERMAX case started with its initial ionization rates determined in Table 3.1 and the ionization reactions were raised by one order of magnitude. The multispecies MHD code was run and if there was no change in the current sheet location the ionization rate was increased again. This process was repeated until the ionosphere dominated the Mars space environment. This procedure was also applied to the APHMIN case, but the ionization rates were reduced by one order of magnitude until there was a visible shift in the magnetotail current sheet.

Figure 3.3 shows the PERMAX and APHMIN non-crustal source cases with the adjusted ionization rates in Table 3.2. The top row of simulation results are plotted with the same

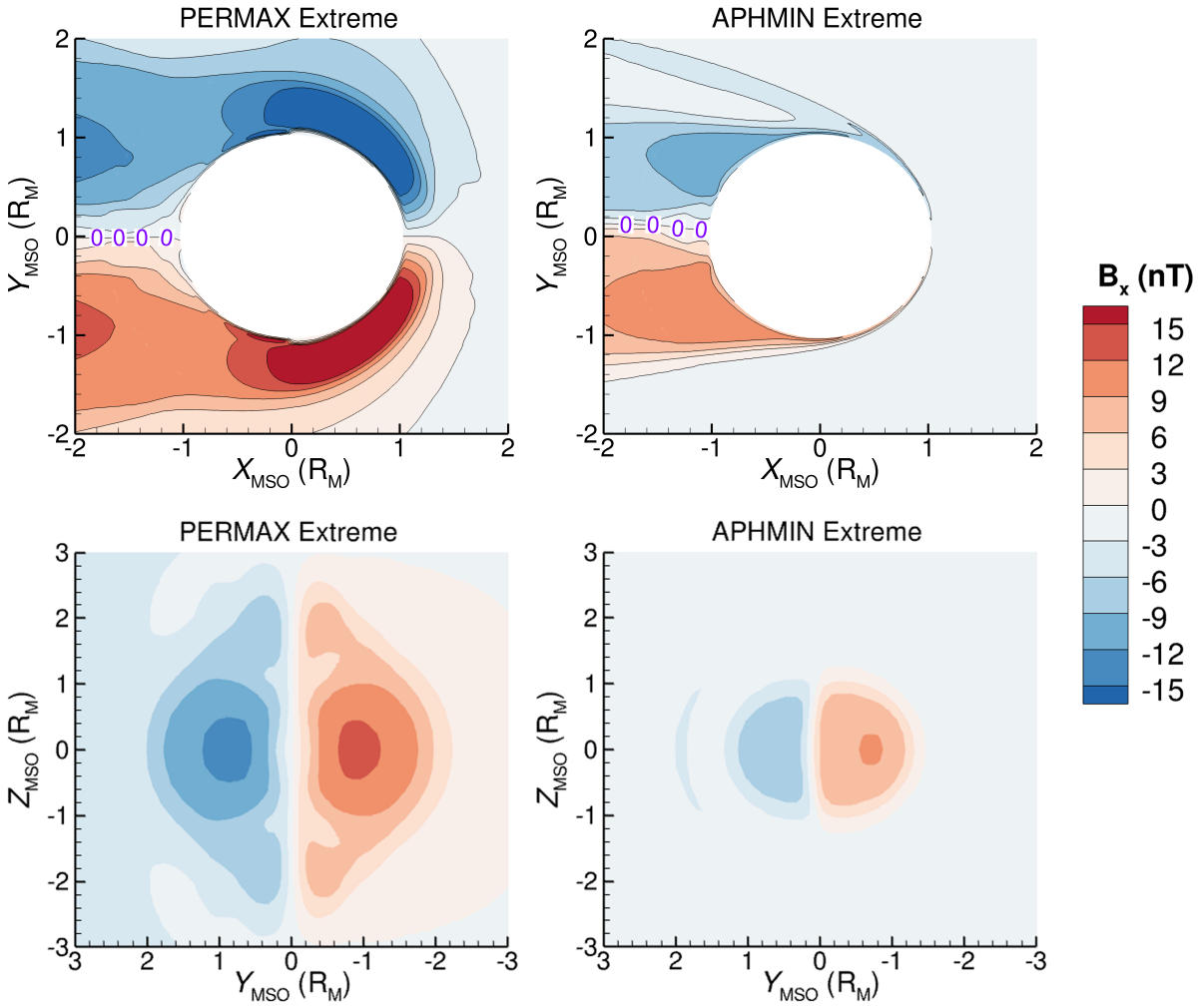


Figure 3.3: PERMAX and APHMIN cases with changes in the ionization rates for the X_{MSO}-Y_{MSO} (top row) and Y_{MSO}-Z_{MSO} (bottom row) planes. The tail slices are extracted at X_{MSO}=-2 R_M and all results are shown from -15 to 15 nT. These results do not include the crustal sources and the ionization rates were modified by several orders of magnitude until a shift in the magnetotail current sheet was present. Refer to Table 3.2 for specific adjustments in ionization rates.

conditions as Figure 3.1, but X_{MSO} ranges from -2 to 2 R_M. The bottom row is plotted with the same conditions as Figure 3.2, but B_x ranges from -15 to 15 nT. The ionization rates were four orders of magnitude greater than the initial PERMAX case, but the magnetotail current sheet remained symmetric along the Y=0 region. Although the current sheet did not shift, the ionosphere dominated the Martian environment and the magnetic field expanded outward. The ionization rates were not increased further, as this would make the ionosphere

too dominant and push the magnetic field away from the inner boundary. The APHMIN case displayed a weak $+Y$ shift and the ionization rates were nine orders of magnitude less than the original APHMIN values. The ionization rates were not reduced beyond this as the current sheet shift was discernible. The ionosphere is exceptionally weak as the IMF pushes against the inner boundary and slips behind the planet.

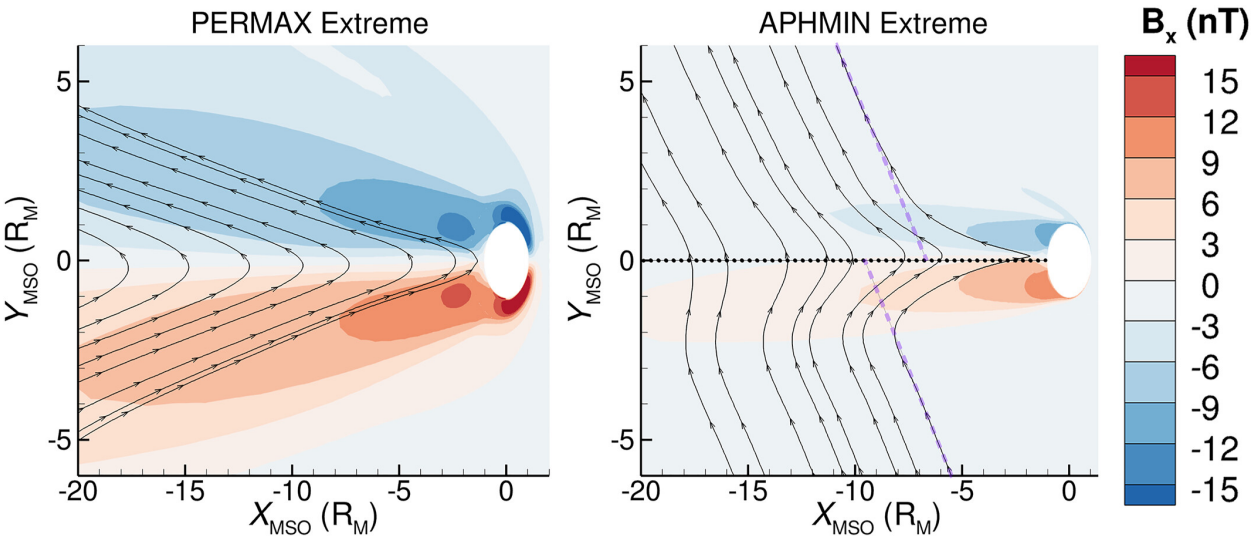


Figure 3.4: IMF behavior downtail in the extreme cases. The black dotted line on the APHMIN extreme case indicates Y=0 and the purple dashed lines indicate where the IMF reaches Y=0 on the dawn and dusk side assuming there is no curvature. The IMF slippage in the PERMAX extreme extends beyond the simulation domain, but the slippage in the APHMIN extreme is near 6 R_M.

While ionization rates significantly alter the behavior of the ionosphere, they do not influence the behavior of the magnetotail current sheet. As the ionization rates increased, the ionosphere and magnetic field became exceptionally stronger. Though the current sheet remained symmetric, the IMF began to build up on the Martian dayside, making it harder to slip past the planet. Figure 3.4 shows the IMF behavior behind Mars in both extreme cases. The PERMAX IMF exhibits very slow slippage, with the curvature of the field lines extending beyond the simulation domain. In contrast, the APHMIN case shows clear signs of slippage. The purple dashed lines indicate the initial IMF location before it begins to curve and reaches Y_{MSO}=0, positioned near X_{MSO}=-6 on the dusk side and X_{MSO}=-9 on the

dawn side. Using the applied solar wind velocity of 400 km/s (∼7 R_M/min), this implies that the slippage around Mars in the APHMIN extreme case takes less than half a minute (∼25 s). The slippage in the PERMAX extreme case takes at least 3 minutes, and perhaps much more. These simulations demonstrate that the ionization rates influence the magnetic field and ionosphere strength but do not contribute to the current sheet asymmetry unless adjusted by unreasonable orders of magnitude.

3.3.3 Dayside Ionosphere

As ionization rates showed no substantial impact on the current sheet asymmetry, the next step was to examine the influence of the dayside ionosphere on the shift. This approach was motivated by Liemohn et al. (2017), who found that the dayside ionosphere, consisting of the bow shock, magnetic pileup region, and magnetosheath, plays a role in driving the current sheet shift in multifluid MHD simulations. In the multispecies code, the atmospheric ion species (H^+, O_2^+, O^+, CO_2^+) have individual densities but share a single velocity and temperature. However, these ions have their own velocities and temperatures in the multifluid MHD code. The multispecies MHD simulations are used to examine the influence of the dayside ionosphere on the current sheet shift with and without the crustal magnetic fields.

Figure 3.5 presents the multispecies PERMAX, APHMIN, PERMIN, and APHMIN simulation results for the log-scaled density of O^+. The top row of plots contains the crustal magnetic fields while the bottom row does not. The ion density ranges from -3 to 3 log-scaled particles per cubic centimeter ($\log_{10}(cm^{-3})$)). The maximum O^+ values, now presented in linear scale, are as follows: PERMAX: 1170 cm^{-3}, APHMAX: 628 cm^{-3}, PERMIN: 252 cm^{-3}, APHMIN: 171 cm^{-3}. The change in peak dayside ionopsheric density for this species is nearly an order of magnitude, and the change is similar for the other ionospheric species (H^+, O_2^+, CO_2^+). This is large enough that if the dayside ionosphere plays a substantial role in the structure of the Mars magnetotail, then it should be seen in these simulation results. Like Figure 3.1, the planet remains fixed at a subsolar position of 180°W, 0°N, ensuring that

the strongest crustal fields are oriented on the dayside.

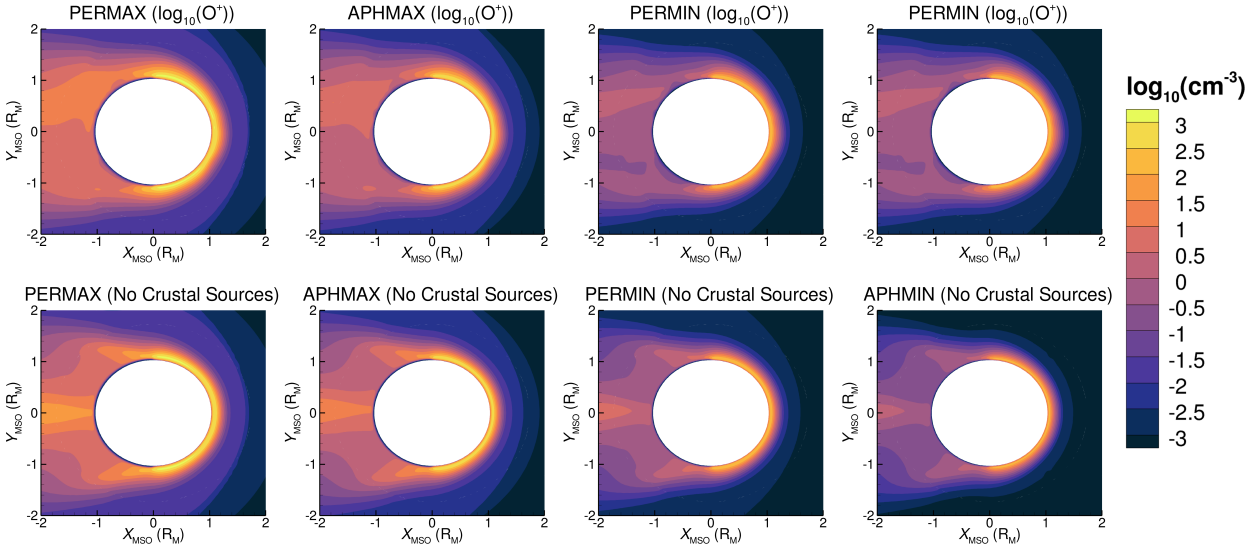


Figure 3.5: Multispecies MHD simulation output of the O^+ ion density in $\log_{10}$-scaled particles per cubic centimeter ($\log_{10}(cm^{-3})$) with and without crustal sources. The maximum O^+ values with and without the log scale are as follows - PERMAX: 3.04 $\log_{10}(cm^{-3})$ or 1170 cm^{-3}, APHMAX: 2.79 $\log_{10}(cm^{-3})$ or 628 cm^{-3}, PERMIN: 2.40 $\log_{10}(cm^{-3})$ or 252 cm^{-3}, APHMIN: 2.23 $\log_{10}(cm^{-3})$ or 171 cm^{-3}.

In the PERMAX case with crustal sources, there is an intense concentration of O^+ on the dayside. On the nightside, the O^+ is asymmetric along the dusk side of the planet. This is also true for the other cases that feature crustal fields, but the concentration of O^+ is weaker. The APHMAX O^+ concentration is not as strong as the PERMAX case, but the ion asymmetry is visible 2 R_M downtail. The $+Y$ asymmetry is also present in the PERMIN and APHMIN cases but is significantly weaker than the solar maximum cases. The results without the crustal magnetic fields change in O^+ accumulation but remain symmetric along the Y=0 plane on the nightside.

These results validate that there is no magnetotail current sheet shift when crustal sources are removed from the simulation. An interesting feature of the results including crustal sources is that the O^+ ion behavior correlates with the magnetotail current sheet asymmetry. Both results show a $+Y$ shift in all cases, suggesting that this ion may contribute to the behavior of the magnetotail current sheet.

3.3.4 MHD Model Comparison

The multispecies MHD simulations presented in this investigation do not agree with the current sheet structure in one multifluid MHD simulation. The Liemohn et al. (2017) study omitted crustal fields from the multifluid MHD simulations and discovered that the current sheet shifted dawnward for PERMAX and APHMAX but duskward for PERMIN and APHMIN. An MHD model comparison is performed to identify the similarities and differences between the two codes.

Figure 3.6 plots the dawn-dusk, nightside, and dayside O^+ density profiles for the following MHD model simulations: multispecies MHD with crustal fields (red), multispecies MHD without crustal fields (orange), multifluid MHD results from Liemohn et al. (2017), which do not include crustal fields (green), and the multifluid MHD simulation results from the MAVEN database which include crustal fields (blue). All simulation results use PERMAX results but the multifluid MHD results from the MAVEN database. The results from this database do not include seasons, so the solar maximum case is used in this comparison.

The dawn-dusk profile plots extract the simulation data for each model 2 R_M downtail and plot the log-scaled O^+ ion density against the Y_{MSO} plane in R_M. This profile uses ranges from -2 to 3 $\log_{10}(cm^{-3})$ for the density and -2 to 2 R_M for Y_{MSO}. The nightside and dayside profiles extract the simulation data for the models at the Y_{MSO}=0 line and plot the log-scaled O^+ ion density against the altitude in kilometers. The nightside altitude is reversed to show the behavior of O^+ as it approaches the inner boundary. These profiles use a uniform scale of -5 to 5 $\log_{10}(cm^{-3})$ for the density and ∼100 to ∼1600 km for the altitude.

The multifluid MHD results from Liemohn et al. (2017) are at least one order of magnitude higher than the rest of the simulation results in the dawn-dusk profile, likely due to the model configuration. As O^+ transitions from dawn to dusk, its concentration peaks near Y_{MSO}=0 in all results. This is also true in the nightside results. As O^+ approaches the inner boundary, the multifluid simulation surges upward before promptly declining. The multifluid

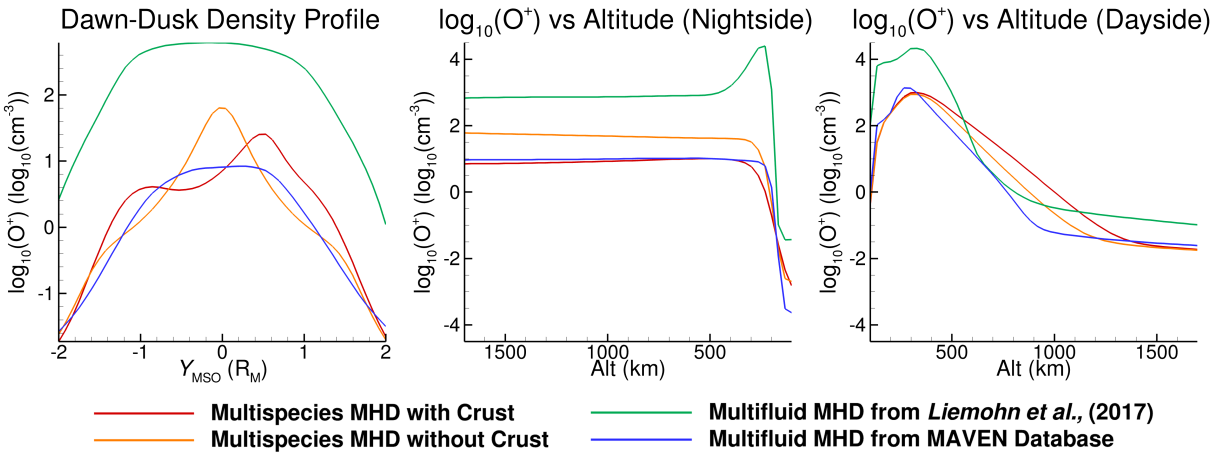


Figure 3.6: MHD model comparison of the dawn-dusk (left), nightside (middle), and dayside (right) log-scaled O^+ profiles. The dawn-dusk profile extracts the simulation data for each model along the X_{MSO}=-2 line and is plotted against the Y_{MSO} plane. The nightside and dayside profiles plot the O^+ ion density against altitude. The nightside altitude is reversed to show the behavior of the O^+ ion as it starts downtail and approaches the inner boundary. All simulations show the PERMAX case except the Multifluid MHD simulations from the MAVEN databse, which uses the average Mars-to-Sun distance of 1.5 AU at solar maximum.

O^+ density is also greater on the dayside, but there is a notable decrease in O^+ around 800 km before the decline becomes less rapid.

Regardless of the crustal source influence, the multispecies MHD results show similar behavior to the MAVEN multifluid MHD simulations. The multifluid MHD simulation from Liemohn et al. (2017) should be comparable to the MAVEN multifluid MHD simulation database, as both use the same multifluid MHD code. The difference between both simulations is significant enough to determine that the results found in the Liemohn et al. (2017) may not be reasonable because of the ionospheric settings used in these runs. The MAVEN multifluid MHD simulations do not include season which may explain the differences between the two results. The multifluid MHD asymmetry is caused by the chemistry and physics of the upper atmosphere (Dong et al., 2015), which is a factor as to why the solution is unique compared to the rest of the MHD simulations. Multifluid MHD also resolves more physics, making it a more realistic model. For better model comparison, the new seasonal variation equations implemented for the multispecies MHD code in this study should be introduced

in the BATS-R-US multifluid MHD code.

3.4 Summary and Conclusions

Formulas implementing seasons were incorporated into the BATS-R-US multispecies MHD code, making it possible to simulate the solar wind interaction at Mars for the following cases: solar maximum at perihelion (PERMAX), solar maximum at aphelion (APHMAX), solar minimum at perihelion (PERMIN), solar minimum at aphelion (APHMIN). The influence of the crustal source was simulated in each of these cases, and it was shown that the crustal magnetic fields are responsible for a duskward ($+Y$) shift in the Martian magnetotail current sheet. When crustal sources were removed from the simulation, the solar wind interaction at Mars was driven by the ionosphere. The current sheet was symmetric along Y_{MSO}=0 in cases omitting the crustal sources, and it was concluded that the crustal magnetic fields exert more control over the current sheet shift than the ionosphere.

Given that the current sheet was symmetric in the cases excluding crustal magnetic fields, the ionization rates for the PERMAX and APHMIN cases were adjusted in an attempt to induce a shift. The ionization rates in the PERMAX case were increased by four orders of magnitude, but the current sheet did not shift. The ionization rates in the APHMIN case were reduced by nine orders of magnitude, and the current sheet shifted slightly towards the $+Y$ region. The ionization rates significantly influence the strength of the ionosphere and magnetic fields but do not influence the current sheet shift unless they are modified to extreme orders of magnitude.

The O^+ concentration was examined on the dayside with and without crustal sources, and it was discovered that the dayside ionosphere only contributes to a degree of magnetotail current sheet asymmetry when crustal sources are included in simulations. It was also concluded that there may be a correlation between the O^+ ion and magnetotail current sheet as both exhibit a $+Y$ shift in similar regions of the Mars space environment. Future

studies should investigate the influence of the Martian longitudinal orientation (explored in Chapter 4) and tilt and more robustly compare the multispecies MHD results to existing MAVEN observations for better data-model comparison.

The Martian magnetotail current sheet plays a crucial role in the solar wind interaction with the induced magnetosphere, influencing key processes such as atmospheric escape and magnetic field dynamics. By incorporating seasonal variations into the BATS-R-US multi-species MHD code, this investigation provides new insights into the behavior of the current sheet, enhancing our understanding of its structure and variability. These findings contribute to a broader understanding of the Mars space environment and its long-term atmospheric evolution.

CHAPTER 4

Rotational Influence on the Martian Magnetotail Current Sheet: A Multispecies MHD Study

This chapter was published in *Journal of Geophysical Research: Space Physics* on 26 March 2026 (Quartey et al., 2026)

4.1 Introduction

Liemohn et al. (2017) employed a simplified multifluid MHD approach that omitted crustal magnetic fields from the simulation. Results from this study determined that the magnetotail current sheet asymmetry was heavily influenced by the ionosphere, with a dawnward shift at solar maximum and a duskward shift at solar minimum. In contrast, Quartey and Liemohn (2025) incorporated Mars' orbital variations into the BATS-R-US multispecies MHD code. Results from the study found that the ionosphere had no significant influence on the magnetotail current sheet as it remained symmetric about the $Y = 0$ plane regardless of the Martian orbital period and solar activity. However, all simulations assumed a fixed subsolar orientation of 180°W, 0°N, where the strongest crustal magnetic fields were oriented on the dayside of the planet.

Factors such as current sheet flapping (DiBraccio et al., 2017; Gao et al., 2018; Zhang

et al., 2023), atmospheric ion composition (Li et al., 2023), spherical harmonic structure of the crustal magnetic fields (Gao et al., 2021), and IMF (Romanelli et al., 2018; Nauth et al., 2024; Wang et al., 2024; Wen et al., 2025) have been shown to influence shifts in the magnetotail current sheet. Despite these insights, the impact of subsolar longitude has not been thoroughly investigated in MHD simulations. This is primarily because most numerical models fix the subsolar point at 180°W, 0°N, aligning the strongest crustal fields on the dayside (Connerney et al., 2001). Ma et al. (2014, 2015) used a time-dependent MHD model to compare with MAVEN Jakosky et al. (2015) observations, but these analyses primarily focused on the plasma interaction process on the dayside of the planet, leaving magnetotail dynamics under different subsolar longitudes unexplored.

This study investigates the magnetotail current sheet asymmetry across multiple local time sectors to examine how the crustal fields influence magnetotail current sheet dynamics across different longitudinal regions of Mars.

4.2 Model Setup

The simulation domain spans from $-24\ R_M < x < 8\ R_M$, $-16\ R_M < y < 16\ R_M$, $-16\ R_M < z < 16\ R_M$. The effective grid near the inner boundary is non-uniform, with a radial resolution on the order of several tens of kilometers and angular resolutions of a few degrees in longitude and latitude. Even though the grid resolution near the inner boundary is coarser than the 5 km or finer resolution in many recent previous utilizations of the Mars BATS-R-US model (Ma et al., 2014, 2019; Sun et al., 2023, 2024, 2025), ensuring that structures analyzed in this investigation are well resolved. The IMF is initialized as a 3 nT away sector Parker spiral (B_x=-1.67 nT, B_y=2.48 nT, B_z=0), and the resulting convective electric field points northward, producing stronger acceleration in the northern ionosphere. The crustal fields are calculated based on the 60-order spherical harmonic model described in detail by Arkani-Hamed (2001), and nominal solar wind conditions are used. Rotating the planet in

15° increments samples the magnetotail behavior across all local time sectors, capturing the influence of crustal magnetic fields at various planetary longitudes.

The configuration and setup used by Sun et al. (2023, 2024) highligh several recent developments in BATS-R-US such as the implementaiton of a point-implicit numerical scheme and other modifcations, but they do not include the Chapman function (Ma et al., 2019). These studies are referenced here to provide context for recent model advancements, but their specific configuration is not implemented in this work.

In constrast, this study uses a fully explicit scheme, in which variables are updated using known values from the previous time step. The grid is non-uniformly spaced, with a radial resolution of ∼5 km at the inner boundary and gradually coarsening with distance to the tail, to balance accuracy and computational efficiency. This configuration is tested against multiple resolutions to assess how resolution influences near-tail structures. All simulations are run for 30,000 iterations until a steady-state solution is reached, and the selected solar condition in this study is PERMAX.

4.3 Results

4.3.1 Magnetic Field Subsolar Longitude Orientation

Figure 4.1 presents results from eight steady-state PERMAX simulations, with the subsolar longitude rotated from 0°W to 105°W in 15°increments. Each panel displays the x-component of the magnetic field B_x from -15 to 15 nT. Red indicates positive B_x, and blue indicates negative B_x. The results are shown in MSO coordinates, where X_{MSO} points from Mars toward the Sun, Z_{MSO} is perpendicular to the Martian orbital plane, and Y_{MSO} completes the right-handed system. The plotted domain ranges from -4 to 2 $\mathrm{R_M}$ in the x-direction and -3 to 3 $\mathrm{R_M}$ in the y-direction. The purple zeros mark where B_x is zero, indicating the location of the magnetotail current sheet.

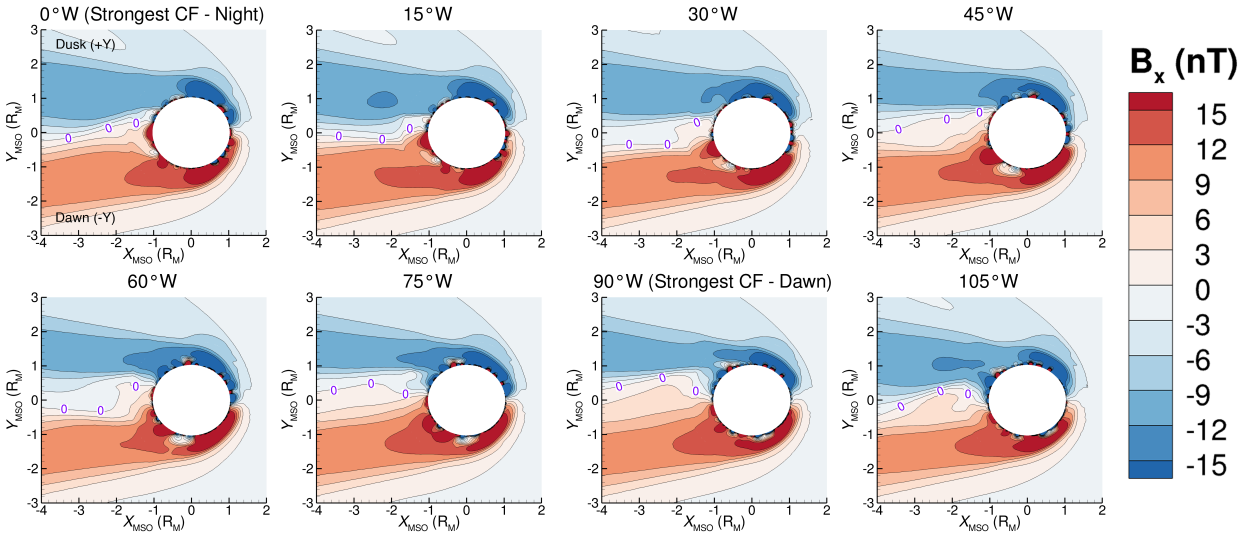


Figure 4.1: Magnetotail current sheet behavior for subsolar longitudes from 0°W to 105°W in 15°increments. Purple zeros indicate where B_x= 0 nT, showing the location of the magnetotail current sheet. At 0°W, the strongest crustal fields (CF) are on the night side. This case also shows that dawn is in the $-Y_{MSO}$ region and dusk in the $+Y_{MSO}$ region. At 90°W, the strongest crustal fields are on the dawn side.

At 0°W, where the strongest crustal magnetic fields are on the night side, and 15°W, the magnetotail current sheet shifts from near the origin toward dawn as it extends downtail. At 30°W and 60°W, the current sheet begins on the dusk side and abruptly shifts dawnward around $X= -2$. At 45°W, the current sheet starts on the dusk side and gradually moves towards the origin with increasing downtail distance. At 75°W and at 90°W, where the strongest crustal fields are at dawn, the current sheet remains consistently duskward. At 105°W, the magnetotail current sheet initially shifts slightly duskward before trending dawnward farther downstream. The largest displacements at $X= -4$ occur at 30°W and 90°W, where the current sheet is roughly $\pm$0.4 R_M.

Figure 4.2 presents B_x results from 120°W to 225°W. At 120°W, the magnetotail current sheet shifts from dawn to dusk and back to dawn as it extends downtail. At 135°W and 150°W, it remains entirely on the dawn side. At 165°W, the current sheet begins at dawn and progressively shifts duskward with increasing downtail distance. At 180°W, where the strongest crustal magnetic fields are on the day side, the current sheet is completely

duskward, a trend also seen at 195°W and 225°W. At 210°W, the current sheet is mostly duskward, but transitions to the dawn side near $X = -3$ R_M. The greatest dawnward displacement at $X = -4$ R_M occurs at 135°W, where the current sheet is approximately -0.4 R_M. The largest duskward displacements are found at 180°W, 195°W, and 225°W, all of which are roughly 0.2 R_M.

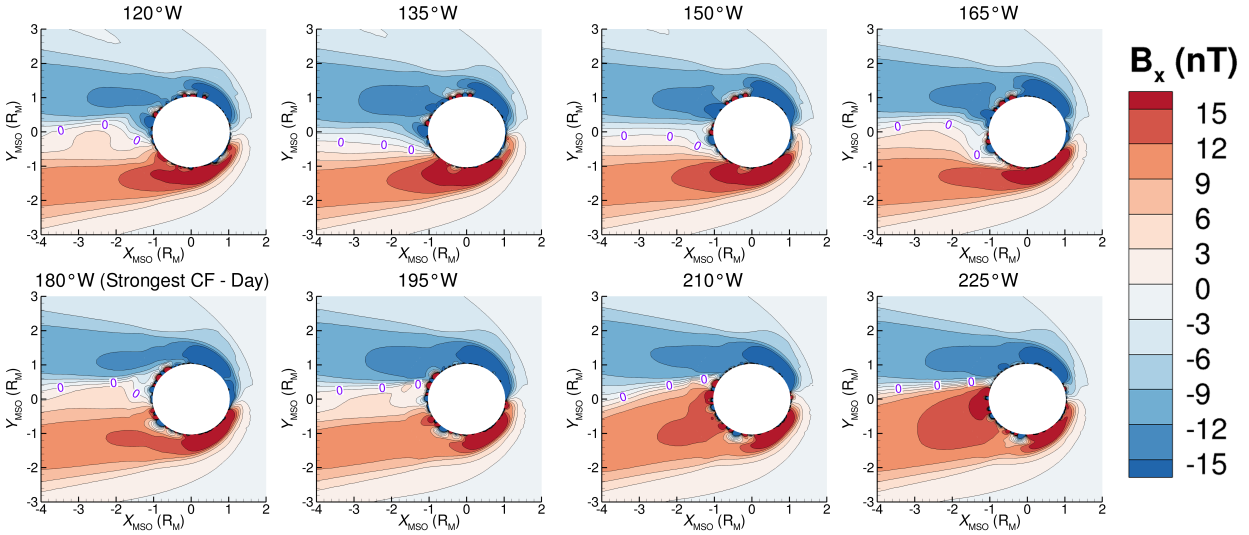


Figure 4.2: Magnetotail current sheet behavior from 120°W to 225°W. At 180°W, the strongest crustal fields (CF) are located on the dayside.

Figure 4.3 presents B_x from 240°W to 345°W. The magnetotail current sheet is entirely on the dusk side at 240°W, 255°W, and 270°W, and entirely on the dawn side at 285°W, 300°W, 315°W, 330°W, and 345°W. The largest dawnward displacement at $X = -4$ R_M occurs at 330°W, where the current sheet reaches approximately -0.4 R_M. The greatest duskward displacement occurs at 255°W, where the magnetotail current sheet reaches approximately 0.4 R_M.

Figure 4.4 shows a schematic summary of the magnetotail current sheet shift at each subsolar longitude. In summary, seven longitudes were completely dawnward, nine were completely duskward, and eight exhibited a dawn-dusk transition, indicating that the magnetotail current sheet configuration is strongly dependent on longitude and influenced by the

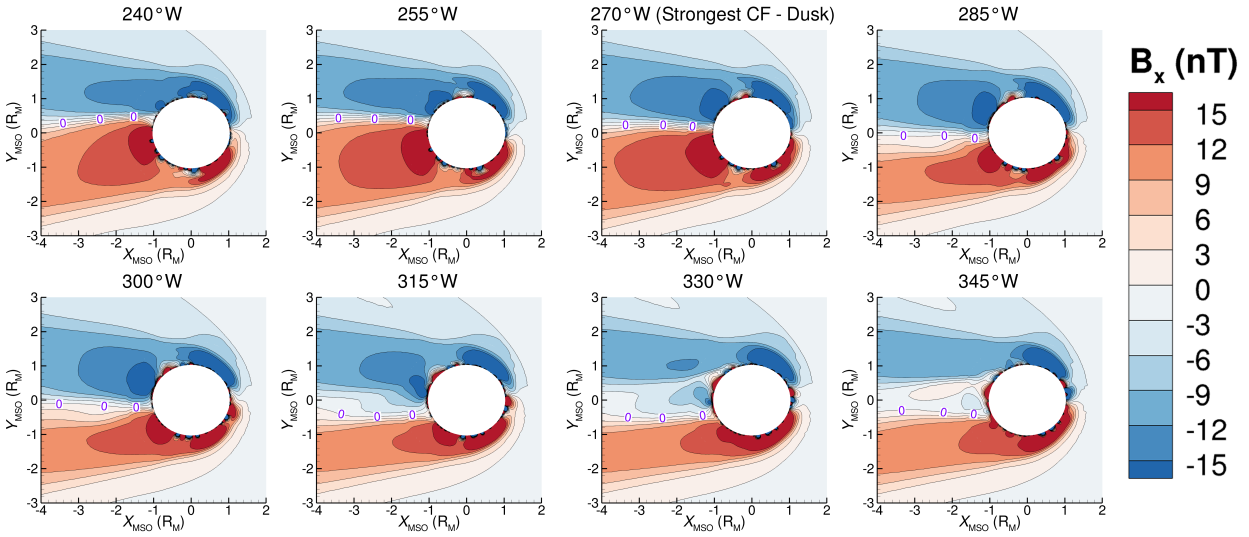


Figure 4.3: Magnetotail current sheet behavior from 240°W to 345°W. At 270°W, the strongest crustal fields (CF) are at dusk.

distribution of crustal magnetic fields.

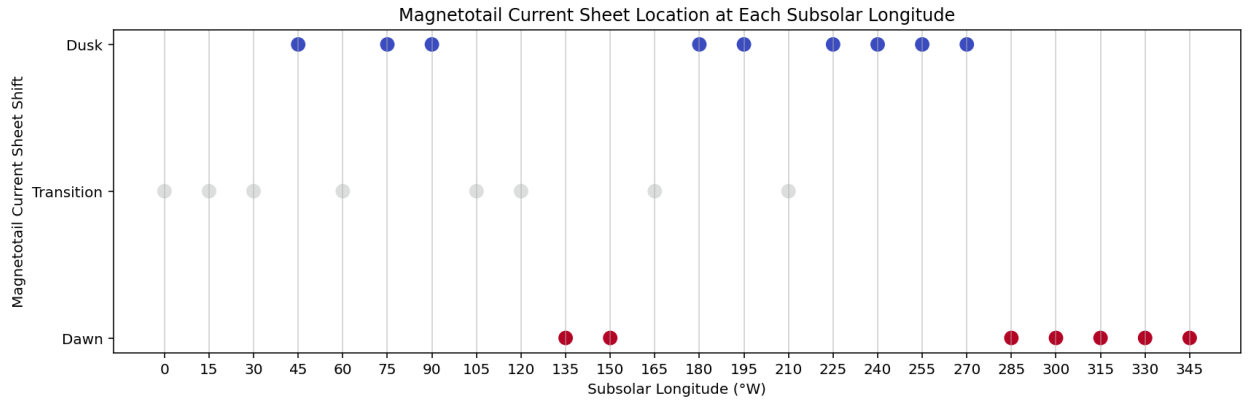


Figure 4.4: Schematic summary of the magnetotail current sheet location at each subsolar longitude. Blue and red indicate that the magnetotail current sheet is entirely dawnward and duskward, while gray indicates that it transitions between dawn and dusk.

Notably, the magnetic field structure is more spatially extended from 0°W to 195°W, while it is more compressed from 210°W to 345°W. This behavior is primarily driven by crustal field orientation but may also be influenced by broader features of the Mars space environment. In all figures, variations in B_x strength are delineated by contour lines. The contour line distribution in Figure 4.1 spans both the dawn and dusk sides of the magnetotail. In contrast,

Figure 4.3 shows more condensed B_x cases, as the contour lines are clustered predominantly on either the dawn or dusk side. These results indicate that the crustal magnetic field orientation plays a significant role in the position and extent of the magnetotail current sheet.

4.3.2 Current Density

Variations in the magnetic field structure across subsolar longitudes revealed a more spatially extended configuration from 0°W to 195°W and a more compressed one from 210°W to 345°W. To investigate the drivers of this behavior, the total current density J is examined, as it provides a proxy for the distribution of magnetic forces throughout the magnetotail. Figure 4.5 presents the total current density in the $X_{MSO} - Y_{MSO}$ plane at 0°W, 90°W, 180°W, and 270°W, when the strongest crustal fields are at night, dawn, day, and dusk. The current density ranges from 0 to 20 nanoamperes per square meter (nA/m^2), and the plotted domain spans from -4 to 2 R_M in the x-direction and -3 to 3 R_M in the y-direction.

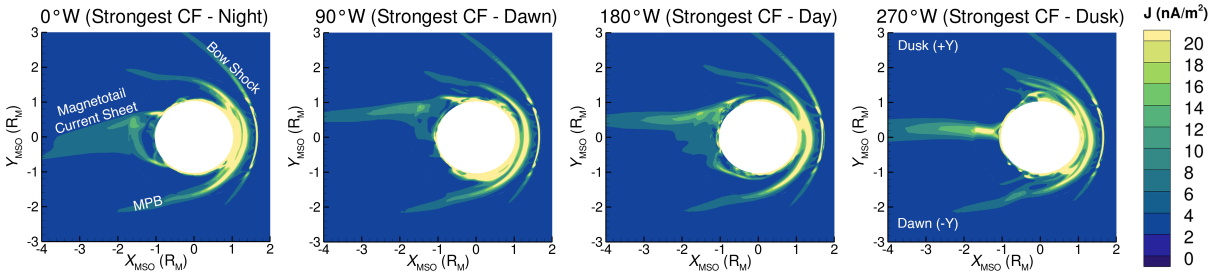


Figure 4.5: Total current density J for cases where the strongest crustal fields are on the night (0°W), dawn (90°W), day (180°W), and dusk (270°W) sides of Mars. Key structures such as the bow shock, MPB, and magnetotail current sheet have been label on the the 0°W case while dawn and dusk are labeled on the 270 °W case. Current density ranges from 0 to 20 nanoamperes per square meter (nA/m^2).

At 0°W, strong current structures appear on both the dawn and dusk sides near $X = -1$ R_M, merging into a unified structure near $X = -1.25$ R_M. At 90°W, the current density is predominantly shifted towards dusk. At 180°W, strong current structures are present on both regions, but the distribution noticeably favors dusk. At 270°W, the current density

is concentrated on the dusk side, with the strongest current between X=-2 and -1 R_M, gradually broadening along Y further down the tail.

These results suggest that the magnetotail current sheet may be bifurcated, meaning it consists of two spatially distinct current areas separated by a low current region, depending on the orientation of the crustal magnetic fields. This claim is supported by the presence of current density on both the dawn and dusk regions at 0°W, 90°W, and 180°W. To further investigate this behavior, Figure 4.6 presents downtail slices at $X = -2$ R_M in the $Y_{MSO} - Z_{MSO}$ plane for the cases shown in Figure 4.5. The current density now ranges from 0 to 0.01 nA/m^2, and the result is viewed from the tail towards the planet. This is the same style of plot done in the observational studies of DiBraccio et al. (2018, 2022). While the system is three-dimensional, examining the peak current density in each slice highlights the regions of strongest current. There are locations where electromagnetic forces are largest and where effects such as atmospheric escape could be the most pronounced.

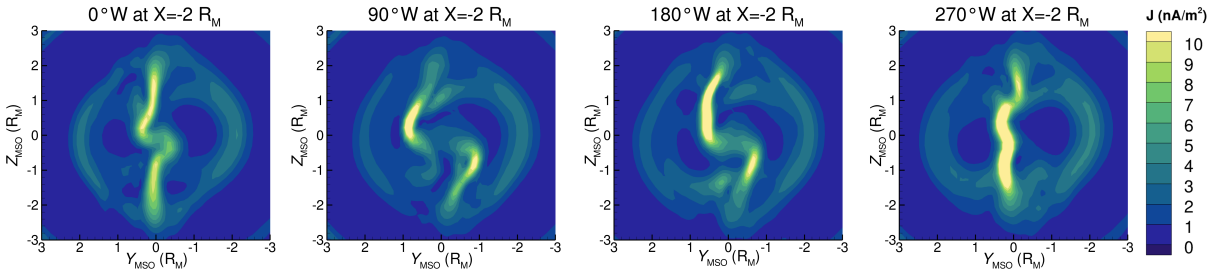


Figure 4.6: Total current density at a downtail slice of $X = -2$ R_M. The current density ranges from 0 to 10 nA/m^2. The slice shown here is representative of the current sheet structure shown in Figure 4.5.

At 0°W, two distinct current structures are split along the equatorial plane ($Z = 0$ R_M), with stronger current concentrated in the $+Y$ region, indicating a duskward shift. At 90°W, the separation between the current structures becomes more pronounced, with the current density shifted towards dusk near Y= 1 R_M. The current density is also bifurcated at 180°W, along Z= 0 R_M, with enhanced current near the $+Y$ region, indicating a duskward shift. In contrast, at 270°W, the current density is uniform, lacking the bifurcation seen in other

sectors. These slice extractions support the conclusion that the crustal field orientation plays a key role in the magnetotail current sheet bifurcation.

Figure 4.7 presents heatmaps of the total current density for all 24 subsolar longitudes at $X = -2$ R_M. At each downtail distance, current density values along $Y = [-1,\ 1]$ R_M at the aforementioned X_{MSO} values were extracted for all 24 subsolar longitudes. These profiles were combined to form heatmaps that compactly visualize current density behavior across all subsolar longitudes, eliminating the need to display 24 individual current density plots. The current density values are extracted along the y-axis from -1 to 1 R_M at 11 uniformly spaced data points. The x-axis of the heatmap corresponds to the subsolar longitude, and the color bar represents current density from 0 to 20 nA/m^2. Figure 4.8 shows a schematic summary of the current density structure at each subsolar longitude. Green shows that the magnetotail current sheet is bifurcated while purple shows that it is uniform.

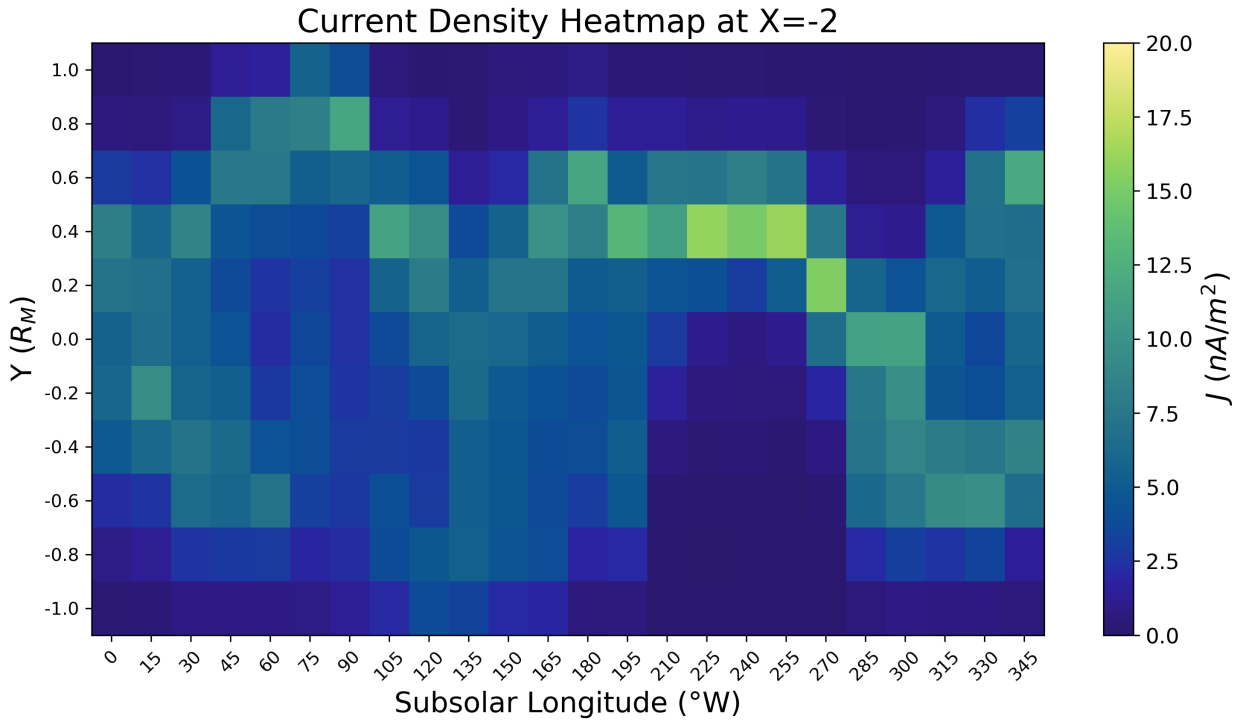


Figure 4.7: Current density heatmap at $= -2$ R_M. The x-axis shows the subsolar longitude in degrees west (°W), and the y-axis shows Y_{MSO} from -1 to 1 R_M. The color bar shows the current density from 0 to 0.02 nanoamperes per square meter (nA/m^2).

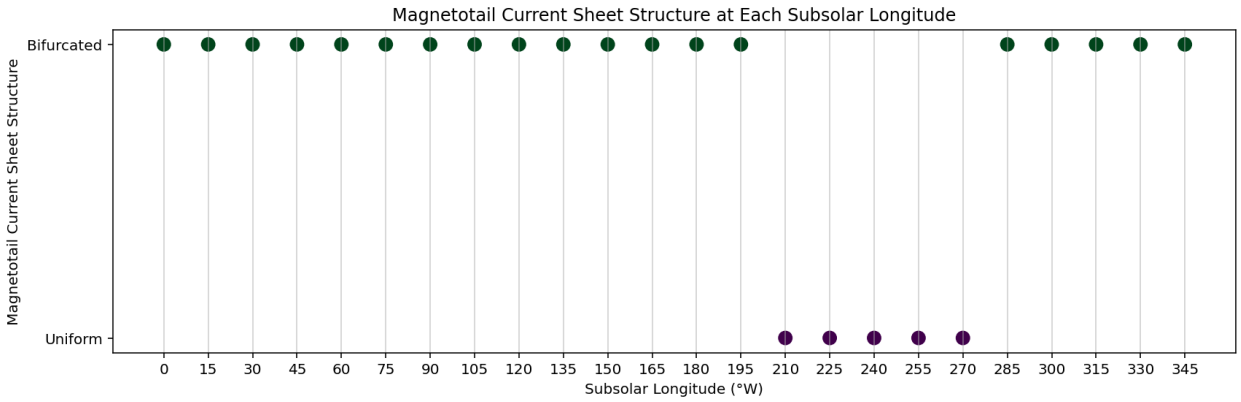


Figure 4.8: Schematic summary of the current density structure at each subsolar longitude. Green indicates that the magnetotail current sheet is bifurcated, and purple indicates that it is uniform.

The current density is present on both the dawn and dusk regions from 0°W to 195°W. At most longitudes, the current is stronger and more prevalent on the dusk side, suggesting that the current density is typically duskward. From 210°W to 315°W, the current density becomes more uniform and is shifted toward dusk. The bifurcation reappears from 330°W to 345°W. As the current density decreases in magnitude farther downtail, bifurcation becomes more apparent.

The region of current density uniformity most consistently appears from 210°W to 270°W, suggesting that the magnetotail current sheet tends to be uniform when the strongest crustal magnetic fields are near dusk. This behavior is likely driven by the orientation of the crustal magnetic fields, which may suppress the formation of a bifurcated current sheet. However, additional simulations exploring other variables may help further explain this behavior. Overall, these results indicate that the magnetotail current sheet exhibits bifurcation or uniformity depending on the orientation of the crustal magnetic fields.

4.3.3 Mass Flux

Following the analysis of current density, and to investigate the cause of the uniformity from 210°W to 270°W, mass flux was examined to identify regions of significant plasma motion,

providing insight into areas where strong electromagnetic forces are most influential. In this single-fluid MHD framework, mass flux measures the bulk plasma motion, indicating where mass and the associated kinetic energy are being transported through the magnetotail rather than particle motion strictly along magnetic field lines. Differences in this flow may help explain the current sheet uniformity. Figure 4.9 shows the mass flux in the $X_{MSO} - Y_{MSO}$ plane at 0°W, 90°W, 180°W, and 270°W from 1.0×10^8 to 2.0×10^9 atomic mass units per square centimeter seconds (amu/cm$^2 \cdot$ s). As in previous figures, the plotted domain ranges from -4 to 2 R_M in the x-direction and -3 to 3 R_M in the y-direction.

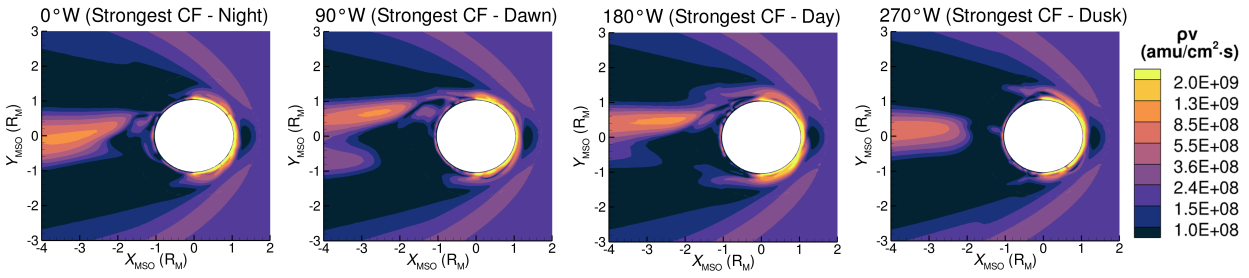


Figure 4.9: Mass flux ρv at 0°W, 90°W, 180°W, and 270°W. Mass flux is calculated as the product of the total ion density and scalar velocity, with values ranging from 1.0×10^8 to 2.0×10^9 atomic mass units per square centimeter seconds (amu/cm$^2 \cdot$ s).

At 0°W, enhanced mass flux is located on both the dawn and dusk flanks of the magnetotail, peaking between $X = -3$ R_M and $X = -4$ R_M. At 90°W and 180°W, mass flux is enhanced primarily on the dusk side, peaking between $X = -2$ R_M and $X = -3$ R_M. At 270°W, mass flux remains slightly shifted towards dusk, but its distribution is more uniform across the magnetotail. Figure 4.10 presents mass flux heatmap slices at $X = -1.5$ R_M, $X = -2$ R_M, $X = -3$ R_M, and $X = -4$ R_M. Like Figure 4.7, the x-axis represents the subsolar longitude in degrees west, and the y-axis represents the Y_{MSO} region from -1 to 1 R_M.

At $X = -1.5$ R_M, the mass flux is relatively weak and concentrated on the dusk side at most subsolar longitudes. Moving downtail, the overall mass flux increases. The duskward preference remains at $X = -2$ R_M, but the mass flux begins to appear on both flanks by the time it reaches $X = -3$ R_M. Despite this, it still favors dusk. At $X = -4$ R_M, strong

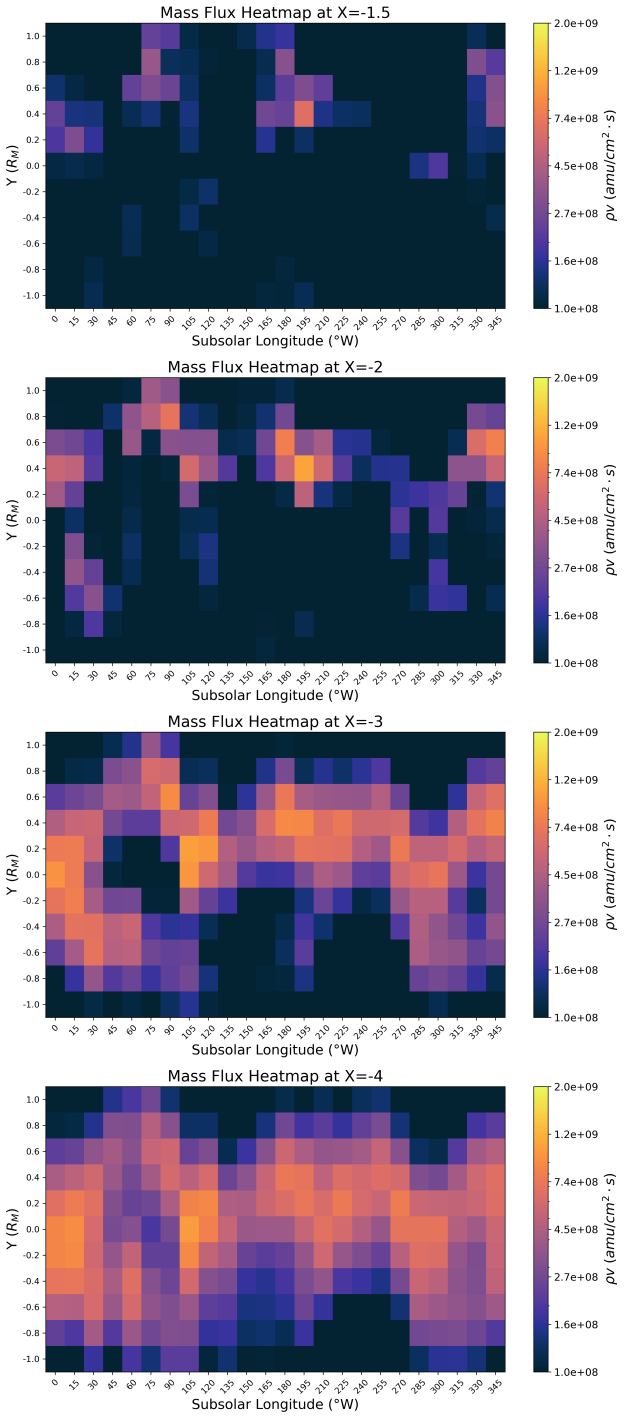


Figure 4.10: Mass flux heatmap slices at $X = -1.5$ $\mathrm{R_M}$, $X = -2$ $\mathrm{R_M}$, $X = -3$ $\mathrm{R_M}$, and $X = -4$ $\mathrm{R_M}$. The x-axis represents the subsolar longitude in degrees west (°W), and the y-axis represents the Y_{MSO} coordinate from -1 to 1 $\mathrm{R_M}$. Mass flux ranges from 1.0×10^8 to 2.0×10^9 atomic mass units per square centimeter seconds (amu/cm$^2 \cdot$ s).

fluxes are present on both sides at every subsolar longitude, suggesting a more balanced distribution at this distance.

A consistent feature across all subsolar longitudes is that mass flux is weaker near $X = -1.5$ R_M. This reflects wake conditions behind Mars, where reduced bulk flow speeds dominate over the higher ion densities near the planet, resulting in lower flux. As the flow progresses downtail, velocities increase while densities decrease, and the combined effect leads to stronger mass flux further downtail. Across the longitudes presented, mass flux generally favors dusk largely due to higher flow speed despite lower densities, whereas the dawn side exhibits slower flows with higher densities. These trends are consistent with the asymmetries found in the magnetic field and current density, linking regions of enhanced plasma transport with regions of strong electromagnetic force.

Figure 4.11 presents a slice of the mass flux taken at $X = -2$ R_M, $X = -3$ R_M and $X = -4$ R_M in the $Y_{MSO} - Z_{MSO}$ plane. Like Figure 4.6, the domain spans from -3 to 3 R_M in both axes, and the y axis is viewed from the tail towards Mars to highlight the twist in the mass flux structure.

The mass flux is bifurcated in all cases at $X = -2$ R_M. When the strongest crustal magnetic fields are at 0°W and 270°W, the bifurcation occurs near the equatorial plane ($Z = 0$ R_M). The mass flux remains bifurcated at $X = -3$ R_M, though it begins to converge at 0°W and 270°W. In contrast, the structures are relatively far apart at 90°W and 180°W. By $X = -4$ R_M, the mass flux has merged into a single sheet at 0°W and 270°W. However, two distinct structures persist at 90°W, indicating that the convergence is incomplete when the strongest crustal fields are on the dawn side of Mars. At 180°W, the mass flux appears close to uniform but shows a weak enhancement toward the southern region. Table 4.1 lists the peak northern, southern, and central mass flux values at the corresponding downtail distances for each case.

At 0°W, $X = -2$ R_M, the mass flux peaks in the southern region at approximately 2.2×10^9

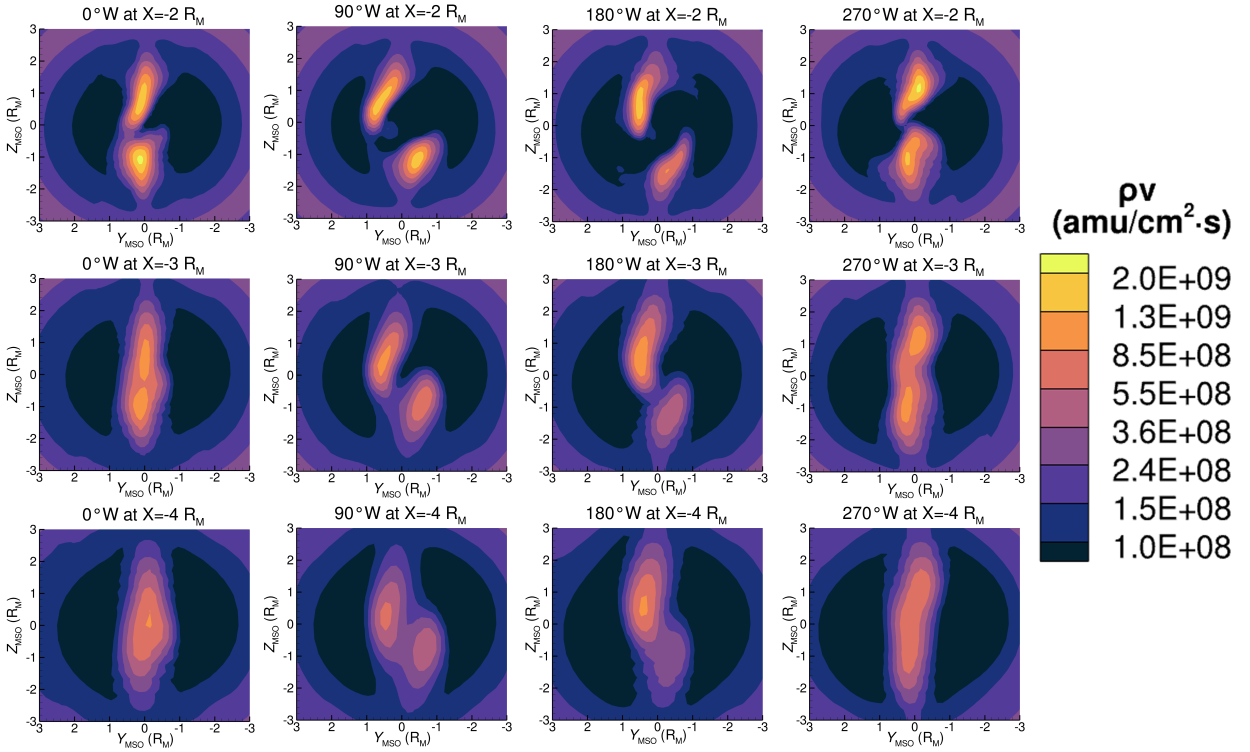


Figure 4.11: Downtail slices of the mass flux at $X = -2$ $\mathrm{R_M}$, $X = -3$ $\mathrm{R_M}$ and $X = -4$ $\mathrm{R_M}$ along the current sheet.

amu/cm$^2 \cdot$ s. The flux is an order or magnitude weaker at the equatorial plane, reaching roughly 2.5×10^8 amu/cm$^2 \cdot$ s. As the flow moves downtail, the mass flux begins to weaken. In contrast, the mass flux increases in the $X_{MSO} - Y_{MSO}$ plane as it moves further downtail. A full understanding of this behavior would require the examination of the three-dimensional distribution, but the focus of this study is on the two-dimensional slices, as downtail evolution is the primary interest of this section. At 0°W, $X = -3$ $\mathrm{R_M}$, the peak mass flux shifts to the northern region, reaching approximately 1.0×10^9 amu/cm$^2 \cdot$ s. The central region also exhibits elevated values, likely due to the convergence of the mass flux structures. By $X = -4$ $\mathrm{R_M}$, the distribution becomes uniform, with a single mass flux peak near the northern region at 8.3×10^8 amu/cm$^2 \cdot$ s, and no distinct central or southern structures present. This trend is also seen at 270°W.

At 90°W, $X = -2$ $\mathrm{R_M}$, the peak mass flux occurs in the southern region at approximately

Table 4.1: Peak northern, central, and southern region mass fluxes at 0°W, 90°W, 180°W, and 270°W

0°W (amu/cm² · s)			
Region	**X=-2**	**X=-3**	**X=-4**
North	1.7×10^9	1.0×10^9	8.6×10^8
Center	2.5×10^8	8.3×10^8	—
South	2.2×10^9	1.1×10^9	—
90°W			
Region	**X=-2**	**X=-3**	**X=-4**
North	1.6×10^9	1.0×10^9	6.4×10^8
Center	1.3×10^8	2.1×10^8	2.9×10^8
South	1.7×10^9	8.1×10^8	5.2×10^8
180°W			
Region	**X=-2**	**X=-3**	**X=-4**
North	1.6×10^9	1.2×10^9	9.2×10^8
Center	7.1×10^7	1.8×10^8	—
South	8.4×10^8	5.4×10^8	3.2×10^8
270°W			
Region	**X=-2**	**X=-3**	**X=-4**
North	2.1×10^9	1.2×10^9	—
Center	1.5×10^8	7.6×10^8	7.7×10^8
South	1.4×10^9	1.0×10^9	—

1.7×10^9 amu/cm$^2 \cdot$ s, though the southern and northern regions are relatively close in value. By $X = -3$ R_M, the peak shifts to the northern region, reaching 1.0×10^9 amu/cm$^2 \cdot$ s. At $X = -4$ R_M, the northern and southern fluxes are comparable, with the northern peak at 6.4×10^8 amu/cm$^2 \cdot$ s and the southern value only slightly lower. A similar trend is seen at 180°W.

In all examined subsolar longitudes, the strongest mass flux occurs near the polar regions, suggesting that enhancements at high latitudes may contribute to the observed bifurcation. These high latitude regions are also where electromagnetic forces can effectively accelerate plasma along open or weakly confined field structures, making them important for plasma transport and potential atmospheric escape. To assess whether these enhancements arise from the influence of crustal magnetic fields, a non-crustal field case was examined. Figure 4.12 shows the resulting mass flux at $X = -2$ R_M, $X = -3$ R_M, and $X = -4$ R_M in the $Y_{MSO}-$

Z_{MSO} plane. In the absence of crustal magnetic fields, the mass flux is remarkably stronger. This can be understood in terms of the reduced magnetic confinement of the plasma. Crustal fields introduce more complex magnetic topology, which can inhibit plasma transport and reduce the efficiency of outflow into the magnetotail. When these fields are removed, the magnetic field becomes more uniformly draped by the solar wind, allowing plasma to flow more freely downstream, resuling in an increase in the net mass flux.

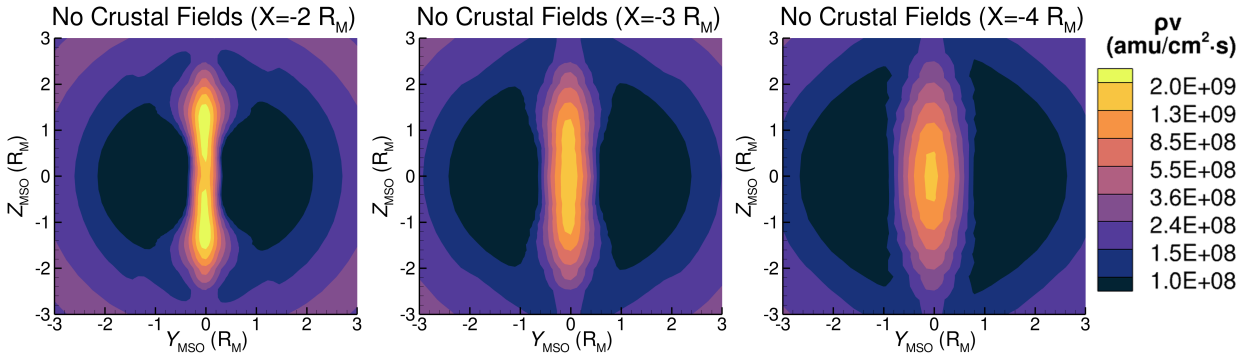


Figure 4.12: Downtail mass flux slices at $X = -2$ R_M, $X = -3$ R_M and $X = -4$ R_M without crustal magnetic fields.

At $X = -2$ R_M, the mass flux is nearly evenly distributed in both regions, with peaks at roughly 3.0×10^9 amu/cm$^2 \cdot$ s respectively. A small gap appears at the equatorial plane, where the mass flux decreases to 1.6×10^9 amu/cm$^2 \cdot$ s. By $X = -3$ R_M, the flux has merged with a central peak at 1.6×10^9 amu/cm$^2 \cdot$ s, with surrounding regions only slightly weaker.

In the absence of crustal magnetic fields, the mass flux bifurcation is not nearly as pronounced as it is in the cases with the crustal fields included, but it still exists. The persistence of the greatest flux near the polar regions suggests that this variable plays a significant role in the magnetotail current sheet asymmetry. Overall, the spatial variations in peak mass flux highlight where plasma transport is most concentrated, and these regions align with the bifurcated structure of the magnetotail current sheet

4.4 Brief Grid Configuration Case Study

Across the 24 subsolar longitudes analyzed, variations in the magnetotail current sheet are evident in the magnetic field, current density, and mass flux. While these differences likely arise from physical processes, others may stem from the numerical effects of the BATS-R-US model. To evaluate this, multiple grid configurations and numerical implementations are tested to determine their influence on the magnetotail current sheet structure.

Table 4.2 outlines the grid resolutions and numerical implementations used for the test cases in this section. All cases are steady-state PERMAX runs executed for 30,000 iterations at a subsolar longitude of 180°W, where the strongest crustal magnetic fields are located on the dayside.

Table 4.2: Inner boundary grid resolution and model options used in each case study

	Case 1	**Case 2**	**Case 3**	**Case 4**	**Case 5**
Grid Geometry	Stretched	Stretched	Adaptive	Stretched	Adaptive
Inner Boundary Res.	Coarse	Coarse	Fine	Intermediate	Coarse
Model Options	Excluded	Included	Included	Included	Included

Cases 1 and 2 use a non-uniform spherical logarithmic grid with relatively coarse resolution at the inner boundary, characterized by radial spacing on the order of tens of kilometers and angular spacing of a few degrees. Case 1 excludes the Chapman function, impact ionization, and charge exchange options, but all other cases do. Cases 3 and 5 use a non-uniform generalized spherical grid with fine resolution, with radial spacing of ∼5 km and angular spacing of a few degrees. Case 4 uses an intermediate-resolution logarithmic grid, with radial spacing of ∼20 km and similar angular spacing as all other cases. These variations allow assessment of how numerical schemes and grid type influence near-tail structures.

Figure 4.13 presents the B_x component of the magnetic field for all five cases, displayed in the $X_{MSO} - Y_{MSO}$ plane. Each case ranges from -4 to 2 R_M in the x-direction and -3 to 3 R_M in the y-direction.

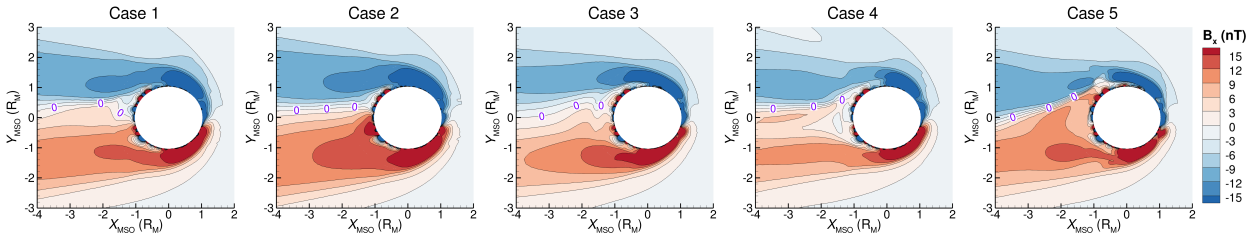


Figure 4.13: Grid configuration cases simulated at 180°W. For grid structure, resolution, and numerical model options, refer to Table 4.2.

The magnetotail current sheet remains consistently duskward across the simulation domain in Cases 1, 2, and 4. In Case 3, the current sheet is predominantly duskward near Mars but gradually moves closer to Y_{MSO}= 0 farther downtail. In Case 5, the magnetotail current sheet is mostly duskward but exhibits a slight shift toward dawn in the far tail.

All five cases exhibit a duskward shift, though the extent and consistency vary. Case 5 shows the largest deviation, with the current sheet beginning on the dusk side and transitioning towards dawn farther downtail. This behavior suggests that while the grid resolution and numerical implementations can influence the detailed morphology of the current sheet, these effects are secondary to the broader trend of duskward asymmetry. Case 5 combines a generalized grid with coarser resolution, offering a balance between physical fidelity and computational efficiency. The grid configurations will be examined in more detail in a forthcoming case study, and the Case 5 model configuration will be used in future studies aimed at enhancing model realism, enabling more robust comparisons with MAVEN observations in Chapter 6.

4.5 Conclusion

This study utilizes the BATS-R-US multispecies MHD code to perform 24 steady-state simulations spaced at 15° intervals to investigate how the magnetotail current sheet dynamics vary across Mars. Using the PERMAX case developed in Quartey and Liemohn (2025), the current sheet was found to be entirely dawnward at seven subsolar longitudes longitudes,

entirely duskward at nine, and alternating between dawn and dusk in the remaining eight (see Figure 4.4 for schematic summary). The magnetic field is more spatially extended at subsolar longitudes from 0°W to 195°W, and more compressed between 210°W and 345°W, suggesting that the crustal field orientation plays a key role in determining the position and extent of the magnetotail current sheet.

The current density was examined at each subsolar longitude, as it provides a diagnostic of how magnetic forces are distributed throughout the magnetotail. Results showed that the magnetotail current sheet is typically bifurcated between 0°W and 195°W, but uniform between 210°W and 270°W, corresponding to configurations where the strongest crustal magnetic fields are oriented towards the dusk side of Mars. These findings confirm that the current sheet morphology depends on the crustal field orientation, exhibiting either bifurcation or uniformity accordingly.

To further investigate the region of uniformity between 210°W and 270°W, the mass flux was examined to indicate where plasma is concentrated and transport is most active. By examining where the strongest crustal fields are on the night (0°W), dawn (90°W), day (180°W), and dusk (270°W) sides of Mars, it was found that the flux is bifurcated at each of these subsolar longitudes. However, at 0°W and 270°W, the mass flux converges farther downtail. These findings suggest that plasma transport is typically concentrated and corresponds to the twin-layer structure of the magnetotail current sheet.

The magnetotail current sheet is a fundamental component governing the interaction between the solar wind and the planet's hybrid magnetosphere, impacting atmospheric loss and magnetic topology. By simulating the solar wind interaction at multiple subsolar longitudes, this study offers novel insights into the morphology and spatial variability of the current sheet. These results contribute to a broader understanding of the Mars space environment and its implications for atmospheric evolution.

CHAPTER 5

Sensitivity of Mars Multispecies MHD Simulations to Model Configuration Choices

This chapter was submitted for review in *Earth and Space Science* on 9 March 2026

5.1 Introduction

MHD models solve a set of equations for the plasma, consisting of the continuity, momentum, and energy for the major ion species. In multispecies MHD models, each ion species has its own density but they all share one velocity and temperature. This approach can capture overall plasma behavior but cannot resolve species specific dynamics on Mars. Multifluid MHD models on the other hand solve separate continuity, momentum, and energy equations for each species, giving each ion its own density, velocity, and temperature. This allows multifluid models to capture features such as polar plumes (Dong et al., 2015), tail ion composition (Fang et al., 2010), ionospheric escape rate differences (Ma et al., 2019), and species dependent tail speeds (Najib et al., 2011). Small scale structures such as thin current sheets or sharp boundaries may not be fully resolved due to finite resolution and numerical diffusion (Powell et al., 1999; Tóth, 2000).

MHD models generally capture large scale trends observed by spacecraft (Dong et al., 2015; Ma et al., 2015; Ledvina et al., 2017) . However, there are inconsistencies in data-model

comparisons, and different model configurations can produce noticeably different results. Even simulations with identical upstream conditions show significant discrepancies (Brain et al., 2010; Egan et al., 2018; Sun et al., 2024), showing how differences in numerical model settings influence physical effects and spatial or temporal scales.

This study presents a focused case analysis using a baseline multispecies MHD configuration and varies each parameter to assess the changes in the magnetotail current sheet.

5.2 Model Description and Configurations

5.2.1 BATS-R-US Multispecies MHD Code

Once again, the BATS-R-US simulation domain ranges from -24 $R_M < x < 8$ R_M, -16 $R_M < y < 16$ R_M, -16 $R_M < z < 16$ R_M. The effective grid resolution near the inner boundary is non-uniform, with a radial resolution of ∼8 km and angular resolutions of ∼2°. The IMF is initialized as a 3 nT away sector Parker spiral, and the crustal fields are calculated based on the 60-order spherical harmonic model described in detail by Arkani-Hamed (2001). Nominal solar wind conditions are used, and all simulations are run for 30,000 iterations until a steady-state solution is reached. The solar condition used in this study is PERMAX (Quartey and Liemohn, 2025). Mars is fixated at 180°W, 0°N, where the strongest crustal magnetic fields are on the dayside (Connerney et al., 2001).

5.2.2 Baseline Configuration

To test the influence of model configuration choices, a baseline configuration is constructed using the spherical generalized grid with user-defined point spacing (Ma et al., 2019). The root level resolution corresponds to 104 × 80 × 40 cells across the domain, yielding a resolution of ∼8 km at the inner boundary radially and ∼2°angularly.

In BATS-R-US, refinement increases spatial resolution by making grid cells smaller. Each

refinement level halves the cell size, providing finer detail where needed. At Mars, three refinement controls are used:

1. Initial refinement - sets the resolution in selected regions at the start of the simulation.
2. Global refinement - increases resolution throughout the entire simulation domain.
3. Inner boundary refinement - increases resolution at the innermost spherical boundary.

Refinement levels are applied in order, so higher refinement can only take effect where lower levels are already present. In the baseline configuration, there are no levels of initial and global refinement and one level of inner boundary refinement. Increasing the global and inner boundary refinements do not change the local resolution unless there is at least one level of initial refinement. The baseline configuration settings used in this investigation are summarized in Table 5.1.

Table 5.1: Baseline configuration settings and corresponding inner boundary grid resolution

Setting	**Default**
Grid geometry	Spherical generalized grid
Radial resolution Δ r (km)	8
Longitudinal resolution Δ ϕ (°)	2
Latitudinal resolution Δ θ (°)	2
Initial refinement levels	0
Global refinement levels	0
Inner boundary refinement levels	1

5.2.3 Grid Configuration Adjustments

Minor adjustments are made to the baseline configuration to test the sensitivity of the results. Table 5.2 shows the grid configurations used in this investigation and the corresponding grid resolution based on the changes made. For each case, only one adjustment is made to the baseline and all other settings remain the same.

Case 2 switches the grid geometry from the generalized to a logarithmic grid, which is also used in the Quartey and Liemohn (2025) investigation. The radial resolution is refined Case

3 and coarsened in Case 4. The longitudinal resolution is refined in Case 5 and coarsened in Case 6. The latitudinal resolution is refined in Case 7 and coarsened in Case 8. The initial refinement level is increased by one level in Case 9. The adjustments to the global and inner boundary refinements are not presented in this study as these results are identical to the baseline. All results are in MSO coordinates.

Table 5.2: Grid configuration adjustments and corresponding inner boundary grid resolution

Case	**Adjustment**	**Δ r (km)**	**Δ ϕ (°)**	**Δ θ (°)**
1	Baseline	8	2	2
2	Logarithmic grid	65	2	2
3	Radial refinement	4	2	2
4	Radial coarsening	10	2	2
5	Longitudinal refinement	8	1	2
6	Longitudinal coarsening	8	3	2
7	Latitudinal refinement	8	2	1
8	Latitudinal coarsening	8	2	5
9	Initial refinement	4	1	1

Figure 5.1 compares the meshes of the baseline (left) to the logarithmic grid (right). The rows display the inner and outer boundary meshes respectively. All other grid settings are identical to the configurations presented in Table 5.1.

The inner boundary baseline grid configuration is ∼8 km radially and 2°angularly. The logarithmic grid has a coarse inner boundary resolution (∼65 km radially, 2°angularly), suggesting that it is not properly solving the ionosphere. At the outer boundary, the logarithmic grid is slightly finer (∼1800 km vs ∼1900 km), which makes is better suited for capturing far tail dynamics of the magnetotail.

Initial refinement also alters the grid structure by expanding the refined region outward from the inner boundary rather than increasing the refinement at the boundary. Figure 5.2 compares this initial refinement mesh to the baseline. As shown in Table 5.2, the initial refinement grid configuration is ∼4 km radially and ∼1°angularly, making it the finest overall grid resolution in all tested cases.

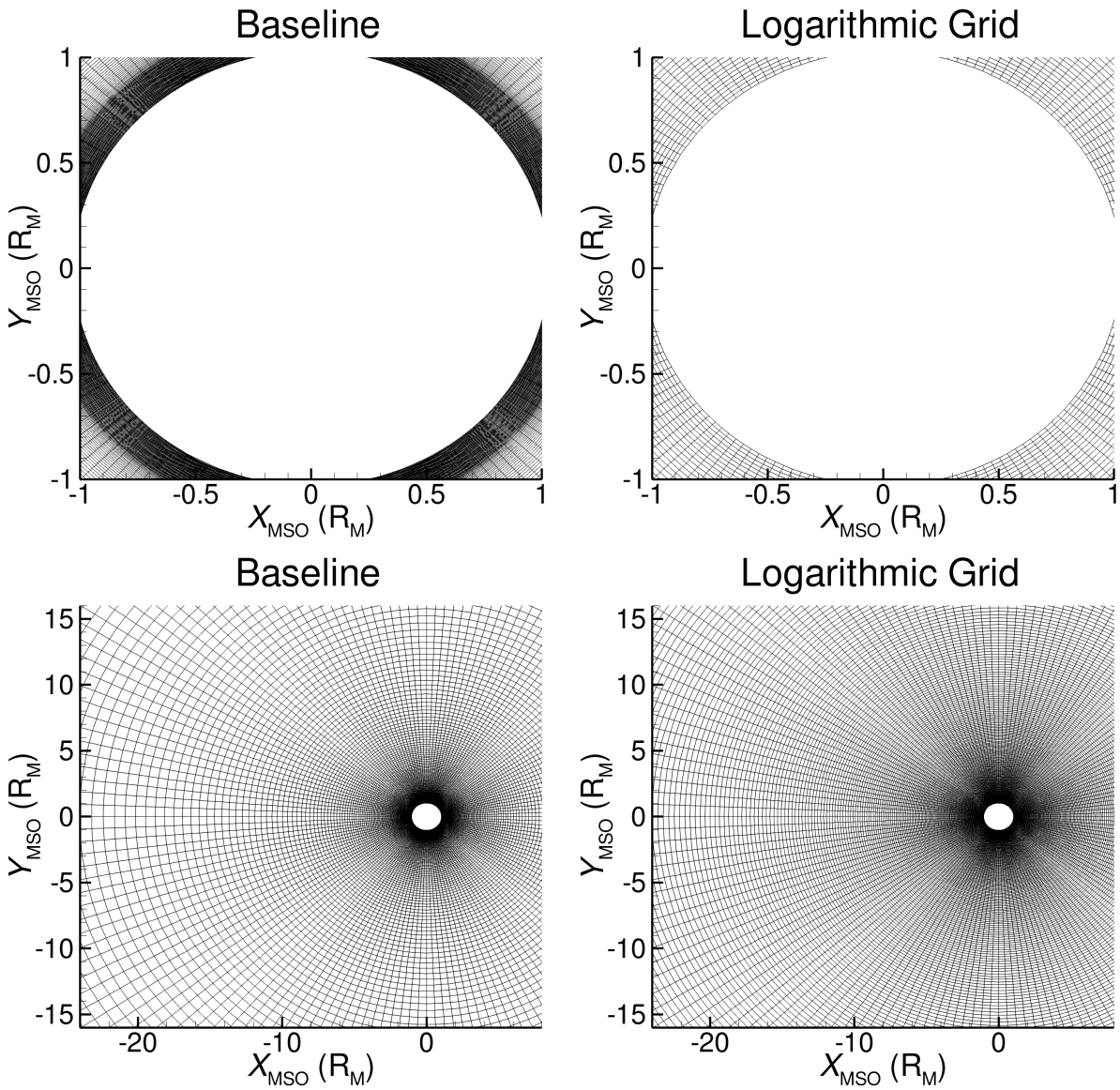


Figure 5.1: Comparison of the baseline (left column) and logarithmic grid (right column) at the inner (top row) and outer (bottom row) boundaries. Grid blocks and refinement levels are identical for both runs.

5.3 Results

5.3.1 Magnetic Field

Figure 5.3 shows a magnetic field comparison of all the adjustments described in Table 5.2. Each case shows the x-component of the magnetic field B_x from -15 to 15 nT with red

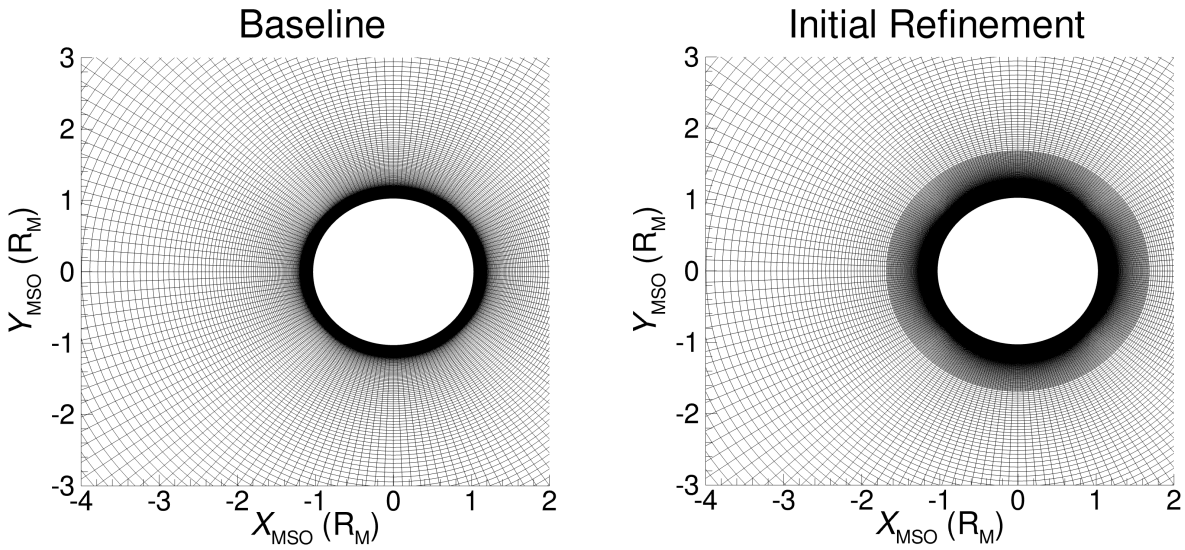


Figure 5.2: Comparison of the baseline (left) and initial refinement (right). X_{MSO} ranges from -4 to 2 R_M and Y_{MSO} from -3 to 3 R_M.

indicating positive B_x and blue negative B_x respectively. X_{MSO} ranges from -4 to 2 R_M and Y_{MSO} from -3 to 3 R_M. The magnetotail current sheet is where $B_x = 0$, indicated by the purple zeros on each case.

The baseline (Case 1) exhibits a dawnward shift throughout the simulation domain. This behavior contrasts the logarithmic grid geometry (Case 2), where the magnetotail current sheet is completely duskward. In addition, the magnetic field strength is significantly enhanced further downtail using the logarithmic grid. The refined radial resolution (Case 3) produces a slightly dawnward shift, yielding an almost symmetric current sheet. The coarsened radial resolution (Case 4) concentrates the magnetotail current sheet on the dusk side of Mars. Variations in longitudinal resolution (Cases 5 and 6) have a minimal effect on the current sheet compared to the baseline, as both cases show a weak duskward displacement. Refined latitudinal resolution (Case 7) results in an entirely duskward current sheet, closely resembling Case 4. The coarsened latitudinal refinement (Case 8) produces the largest dawnward displacement, near -0.6 R_M. Finally, incorporating initial refinement (Case 9) leads to an overall duskward shift, with small-scale fluctuations near the planet.

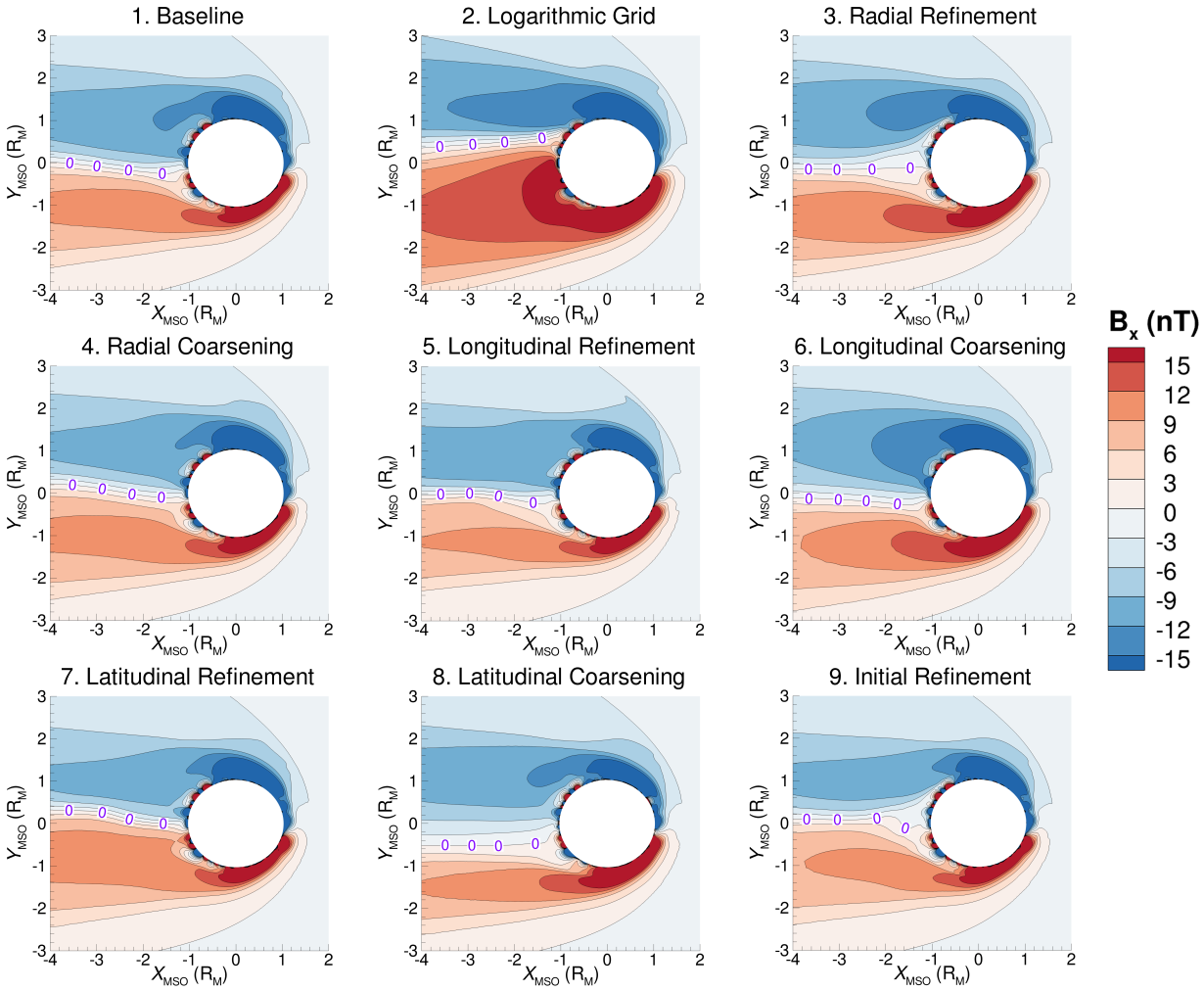


Figure 5.3: Magnetic field in the x-direction for all cases shown in Table 5.2. The magnetotail current is is located where B_x= 0 nT, indicated by the purple zeros on each case.

Across all cases, a consistent trend emerges in which reduced grid blocks in any direction correlate with a systematic dawnward shift of the magnetotail current sheet. Conversely, simulations with refined resolution tend to exhibit increased spatial fluctuations in the current sheet location rather than a uniform shift. Despite these variations, the magnetotail current sheet in most cases converges towards the central tail region as it approaches X=-4 R_M, remaining close to the Y=0 downstream.

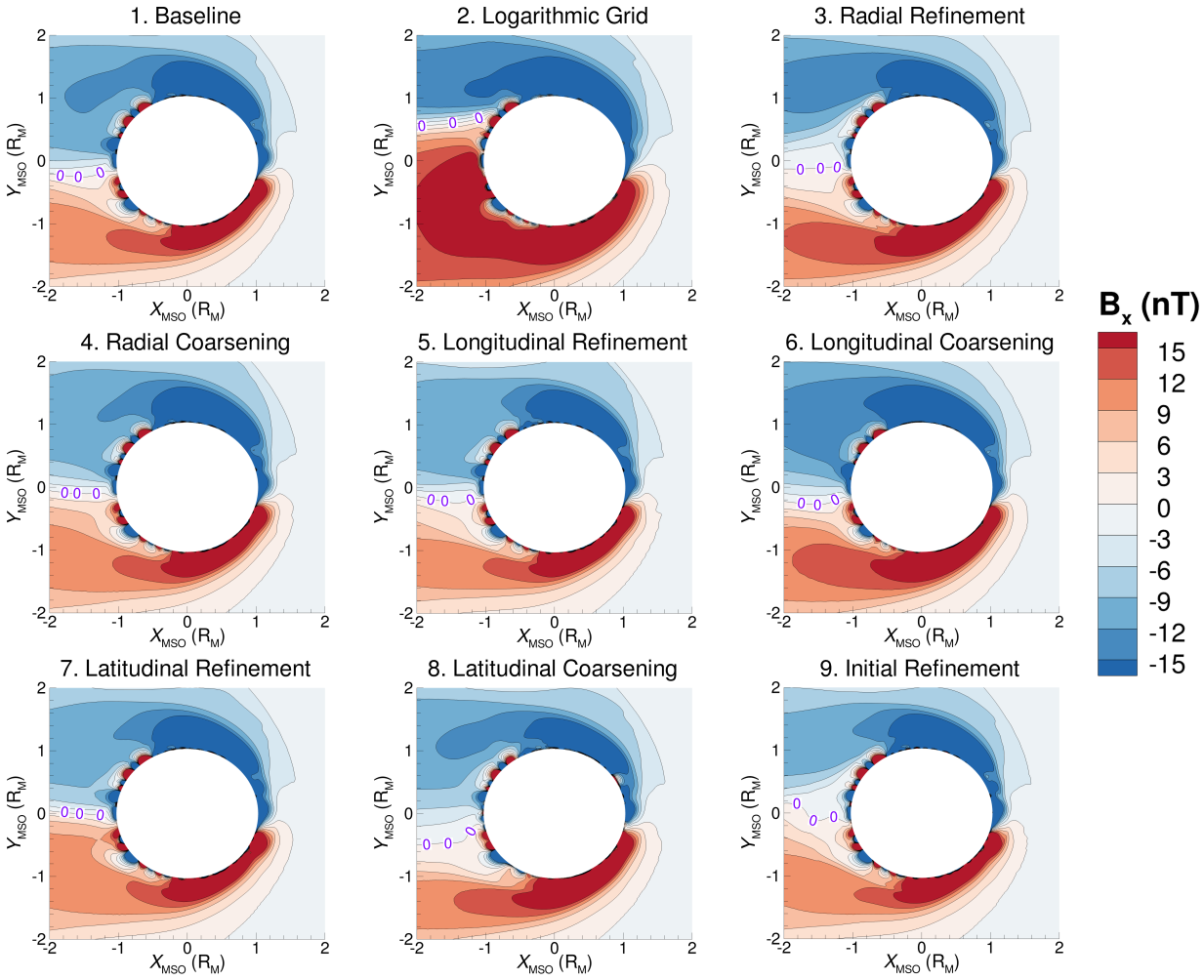


Figure 5.4: Zoomed in version of Figure 5.3 with a range from -2 to 2 R_M.

Figure 5.5 shows the slice at X=-2 R_M of the magnetic field in the $Y_{MSO} - Z_{MSO}$ plane. These simulation results range from -3 to 3 R_M and present B_x from -10 to 10 nT, and the y-axis is flipped to show the view of the tail toward the Sun.

In this plane, all cases exhibit variability with a pronounced twist in the magnetotail current sheet near Y=0. Case 2 produces a substantially stronger magnetic field compared to all other cases. This enhancement is likely attributed to the reduced representation of ionospheric dynamics near the inner boundary. Increasing the grid resolution in any direction elongates the twisted structure, whereas simulations with coarser resolution closely resemble Case 1.

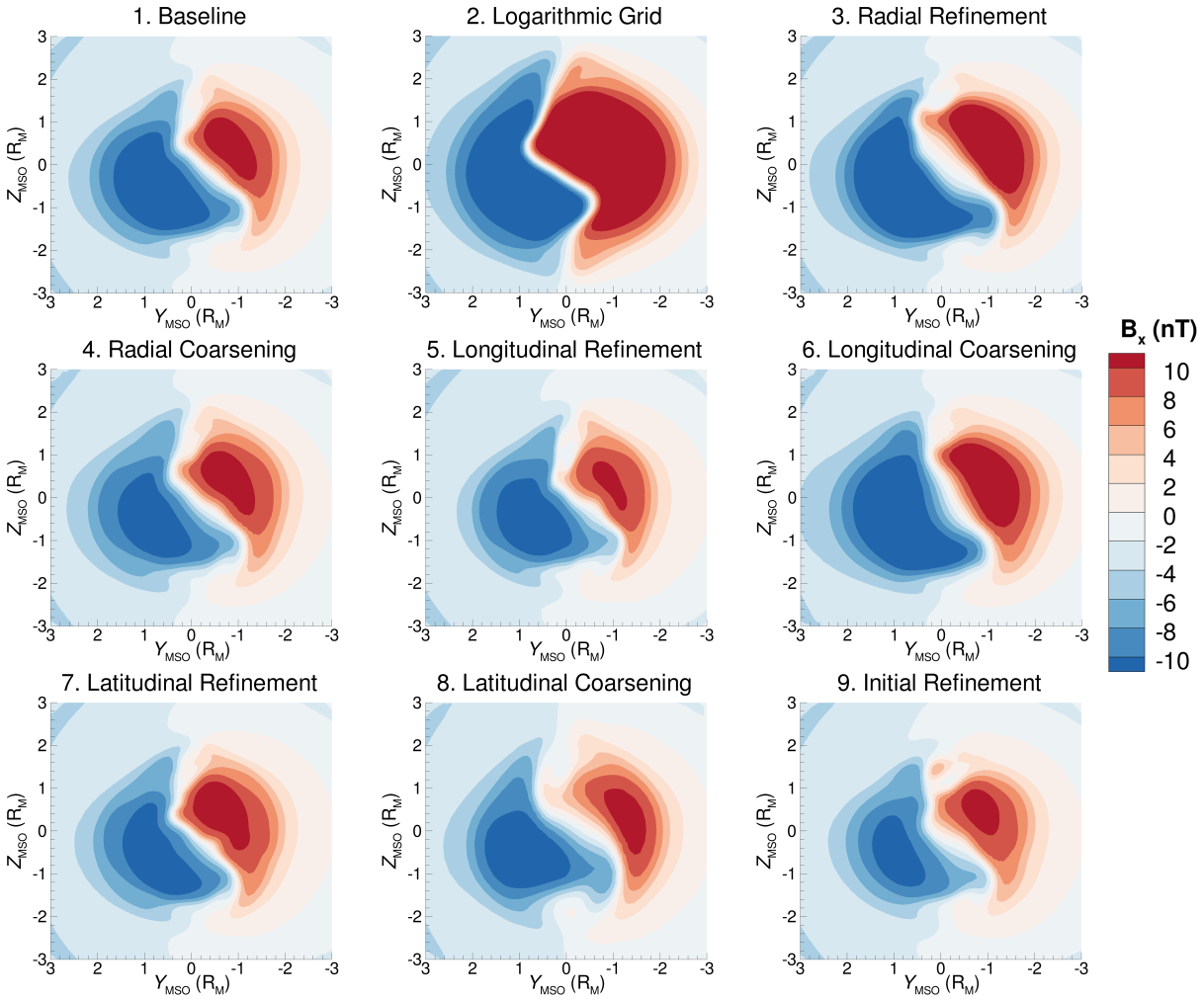


Figure 5.5: Magnetic field slice at X=-2 R_M, as seen from the $Y_{MSO} - Z_{MSO}$ plane. The Y_{MSO}-axis is reversed to show the magnetotail current sheet behavior from the tail towards the Sun.

All slices exhibit the S-shaped structure reported in previous studies (DiBraccio et al., 2017; Quartey and Liemohn, 2025), though the magnitude and displacement varies with model configuration. Among all cases, Cases 4 and 7 show the closest agreement with the baseline. The logarithmic grid produces a notably thinner S-shape and a systematically stronger magnetic field compared to the generalized grid, likely associated with its coarser inner boundary. Modifying the grid resolution in any direction does not substantially alter the magnetotail current sheet morphology in this plane, with the largest deviations arising from the logarithmic grid.

With a coarse inner boundary, the magnetic field appears stronger than it typically would under the same conditions as the baseline. Within the focused parameter study, variations in grid geometry primarily affect the magnitude and displacement of the magnetotail current sheet, with the logarithmic grid producing the most pronounced deviations from the baseline.

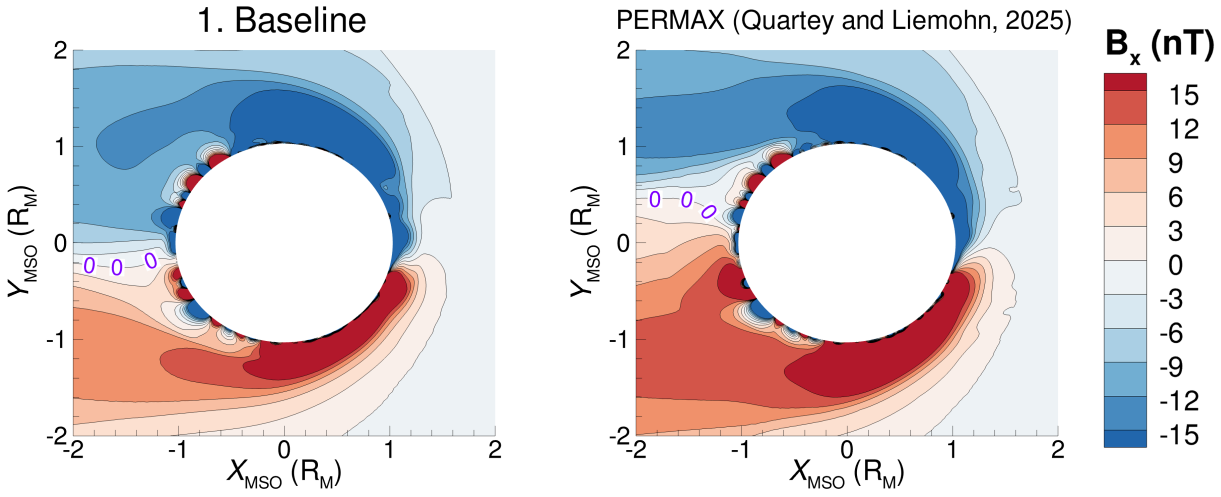


Figure 5.6: Comparison of B_x from the baseline and Quartey and Liemohn (2025).

5.3.2 Total Current Density

Having characterized the magnetotail current sheet structures across various grid configurations, we next examine the total current density J, which reflects the distribution of magnetic stresses in the tail. Figure 5.7 shows the total current density J for all cases in the X_{MSO}-Y_{MSO} plane. The current density ranges from 0 to 20 nanoamperes per square meter (nA/m^2), and the plotted domain spans from -4 to 2 R_M in the x-direction and -3 to 3 R_M in the y-direction.

At the baseline, the total current density is concentrated near the Y=0, but there is also current present along dawn (-Y) and dusk (+Y). Case 2 exhibits a strong current downtail, primarily focused on the dusk side and deviates most strongly from most cases. For Case 3, the current is relatively weak and predominantly concentrated at dawn. Cases 4-7 resemble the baseline in overall morphology, though the current density strength varies across these

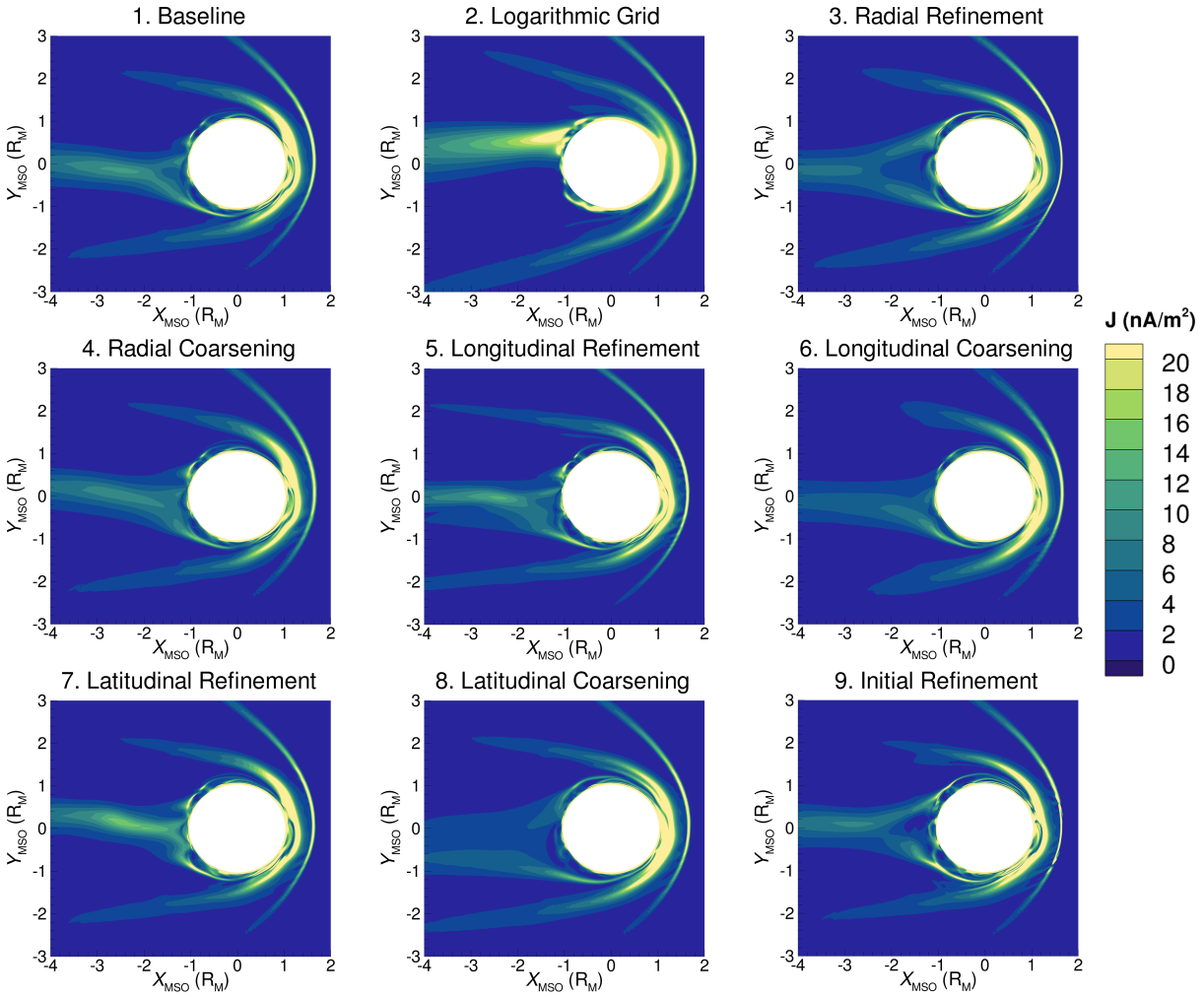


Figure 5.7: Total current density cases in the X_{MSO}-Y_{MSO} plane. Current density ranges from 0 to 20 nanoamperes per square meter (nA/m^2).

configurations. Case 8 produces a pronounced dawnward shift that also deviates strongly from the baseline. Finally, Case 9 produces a current density distribution similar to Case 3.

Overall, the total current distribution is consistent across parameters modified in this case study. Only Cases 2 and 8 show notable deviations from the baseline, while the remaining configurations are in close agreement in both structure and location. However, all cases exhibit a bifurcated current system, where distinct currents are present at the dawn and dusk sides behind Mars.

To further understand the behavior of the bifurcated current structure across different model configurations, a slice in the Y_{MSO}-Z_{MSO} plane is analyzed. Figure 5.8 shows the slices of the total current density 2 R_M downtail from 0 to 10 nA/m^2.

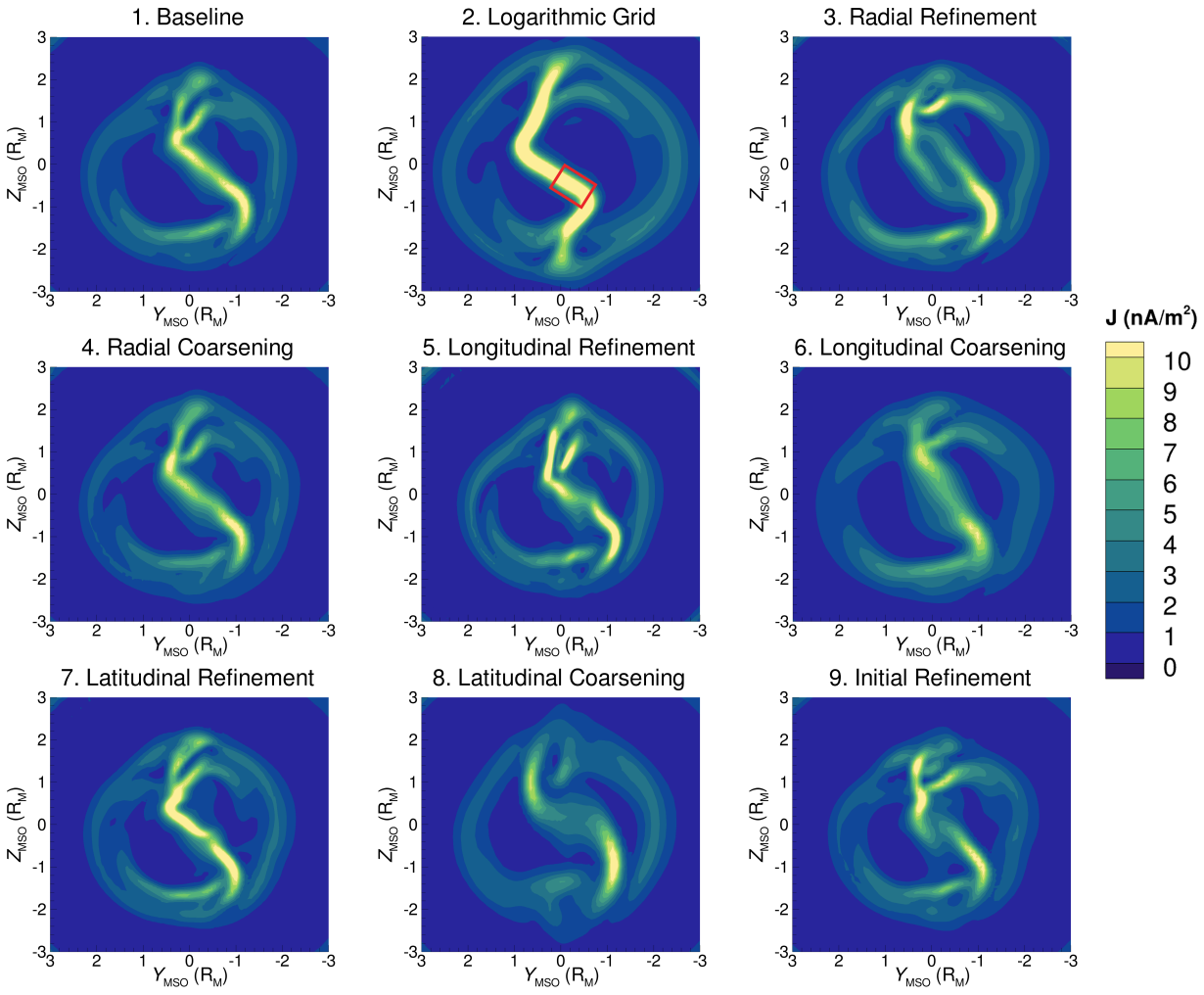


Figure 5.8: Total current density at X=-2 R_M in the Y_{MSO}-Z_{MSO} plane from 0 to 10 nA/m^2. The red square in Case 2 shows where the current is weaker, indicating the location of the bifurcation.

The baseline exhibits a bifurcated current structure, with two strong currents above and below the equatorial plane separated by a weaker central current. This central current is shifted slightly towards dawn. In Case 2, the current sheet appears uniform due to the saturated color scale, but the bifurcation in this slice is located below the equatorial plane near Z=-1 R_M and is also shifted dawnward. Case 3 shows a bifurcated structure above and

below the equatorial plane that is more spread out between dawn and dusk, producing the largest apparent bifurcation of all cases. Cases 4, 5, 7, and 9 closely resemble the baseline, while Cases 6 and 8 deviate slightly in structure. In each of these cases, the bifurcation still remains near the equatorial plane and shifted towards dawn.

This plane focuses on the shape of the current, specifically whether the model configurations still exhibit the bifurcated structure. All cases show this feature, though Case 2 displays the least defined S-shape, appearing nearly uniform due to the strong current in this plane. Within the context of this focused parameter study, these results suggest that the logarithmic grid produces a less well-defined magnetotail current sheet compared to other model configurations.

5.4 Grid Geometry

Within this controlled parameter study, most variations in grid configuration produce only modest changes in the large-scale magnetotail structure. However, the logarithmic grid consistently introduces the most significant differences, affecting the shape, magnitude, and displacement of the magnetic field and total current density.

Quartey and Liemohn (2025) used the BATS-R-US multispecies MHD code to simulate the solar wind interaction at Mars under four developed solar conditions (PERMAX, APHMAX, PERMIN, APHMIN). The grid settings used in that investigation are summarized in Table 5.3. The root level resolution corresponded to $80 \times 80 \times 16$ cells across the domain, yielding a radial resolution of $\sim$40 km, longitudinal resolution of $\sim1^{\circ}$, and a latitudinal resolution of $\sim2^{\circ}$.

The grid settings from this investigation are compared with those used in Quartey and Liemohn (2025). Figure 5.9 shows the corresponding mesh structures, with the baseline configuration displayed in the top row and the Chapter 3 configuration in the bottom row. The

Table 5.3: Grid configuration and corresponding inner boundary resolution from Quartey and Liemohn (2025).

Setting	Default
Grid Geometry	Logarithmic grid
Radial Resolution Δ r (km)	40
Longitudinal Resolution Δ ϕ (°)	1
Latitudinal Resolution Δ θ (°)	2
Initial Refinement Levels	1
Global Refinement Levels	0
Inner Boundary Refinement Levels	9

columns show the mesh at the inner boundary, the range used throughout the investigation, and across the full simulation domain.

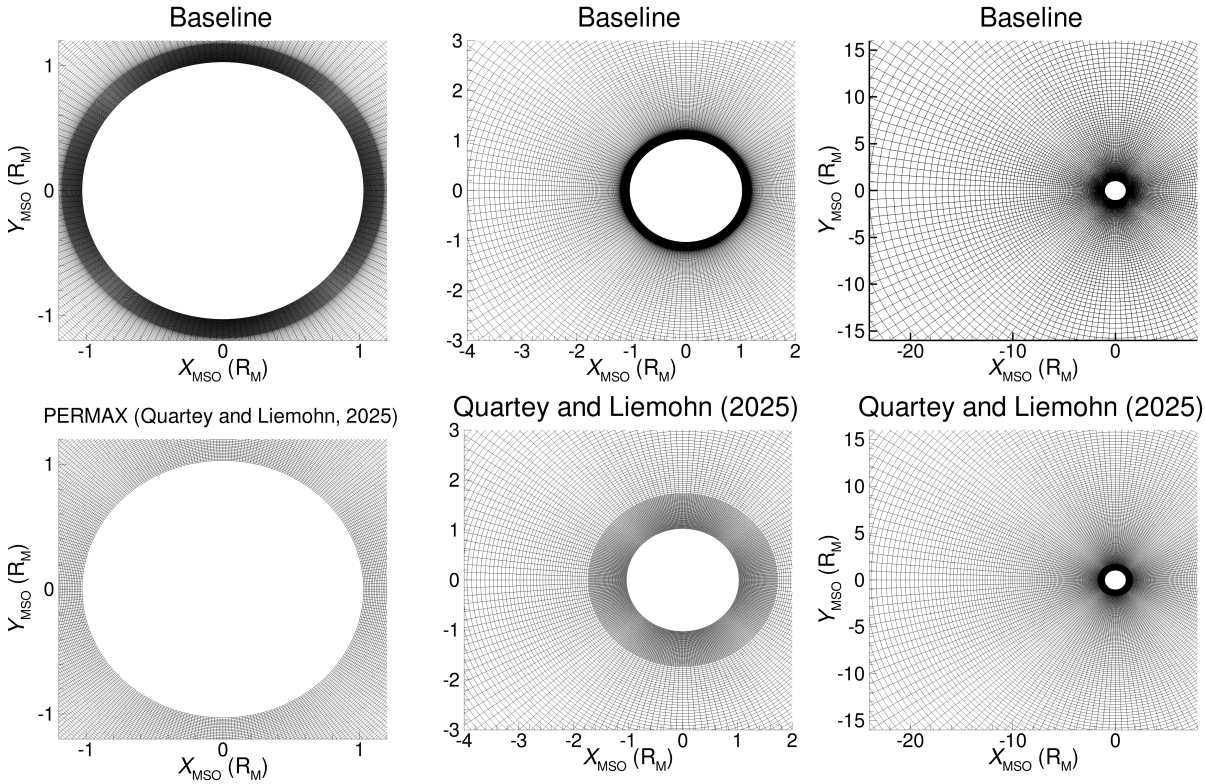


Figure 5.9: Mesh comparison of the baseline and Quartey and Liemohn (2025) at the inner boundary, mid-range (X_{MSO}=[-4, 2] R_M, Y_{MSO}=[-3, 3] R_M), and the full simulation domain. See Tables 5.1 and 5.3 for the details of the grid settings used in each study.

At the inner boundary, the baseline mesh is more refined than the settings used in Quartey and Liemohn (2025). Moving outward, the Quartey and Liemohn (2025) mesh remains

coarser than the baseline, but the region of refined cells extends to roughly 2 R_M. At the outer boundary, Quartey and Liemohn (2025) becomes more refined than the baseline.

Figure 5.10 compares the magnetic field B_x of the baseline and Quartey and Liemohn (2025) settings at PERMAX, APHMAX, PERMIN, and APHMIN to examine the variation of the magnetotail current sheet with each setting. Cases are plotted in $X_{MSO} - Y_{MSO}$ plane ranging from 4 to 2 R_M in X_{MSO} and -3 to 3 R_M in Y_{MSO}.

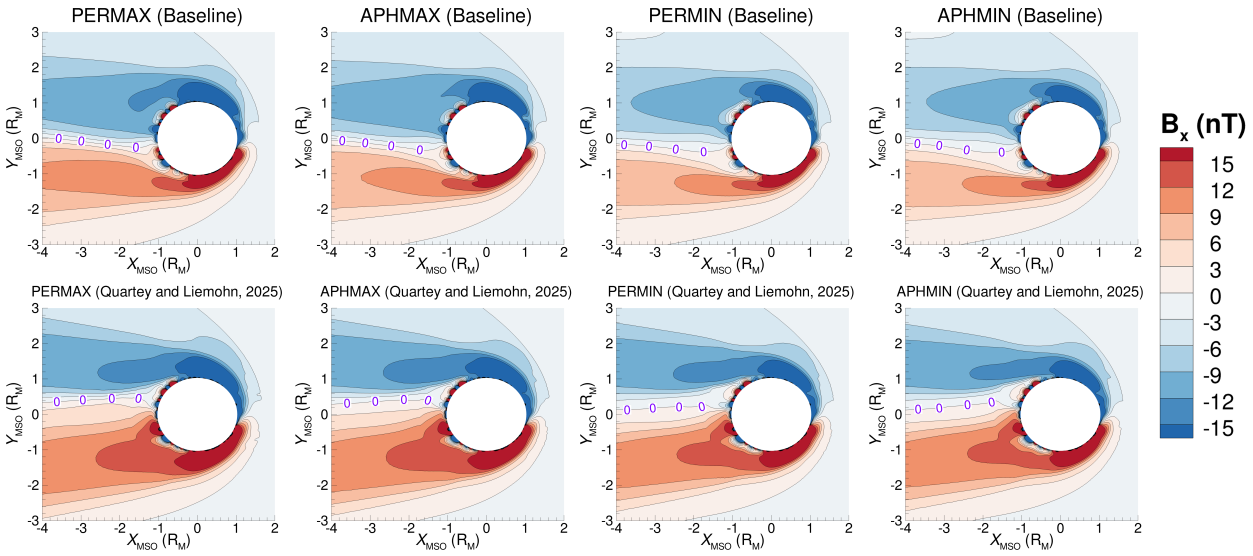


Figure 5.10: Magnetotail current sheet comparison of the baseline grid settings and the grid settings of Quartey and Liemohn (2025), rerun here using an updated version of BATS-R-US. PERMAX - solar maximum at perihelion, APHMAX - solar maximum at aphelion, PERMIN, solar minimum at perihelion, APHMIN - solar minimum at aphelion. At -4 R_M, the magnetotail current sheet is shifted in the following ranges (top to bottom): 0 R_M, -0.1 R_M, -0.2 R_M, -0.1 R_M, 0.3 R_M, 0.3 R_M, 0.1 R_M, 0.1 R_M.

The baseline PERMAX case shown here corresponds to Case 1 in Figure 5.3 and is shifted slightly dawnward near Y_{MSO}= 0. This dawnward shift is consistent across the other baseline cases (APHMAX, PERMIN, and APHMIN). In Quartey and Liemohn (2025), all cases show a slightly duskward shifted magnetotail current sheet.

Figure 5.11 shows B_x at $X = -2$ R_M and displays it in the $Y_{MSO} - Z_{MSO}$ plane. Both Y_{MSO} and Z_{MSO} range from -3 to 3 R_M, and the y-axis is flipped to show the behavior of the magnetotail current sheet from the tail towards the Sun.

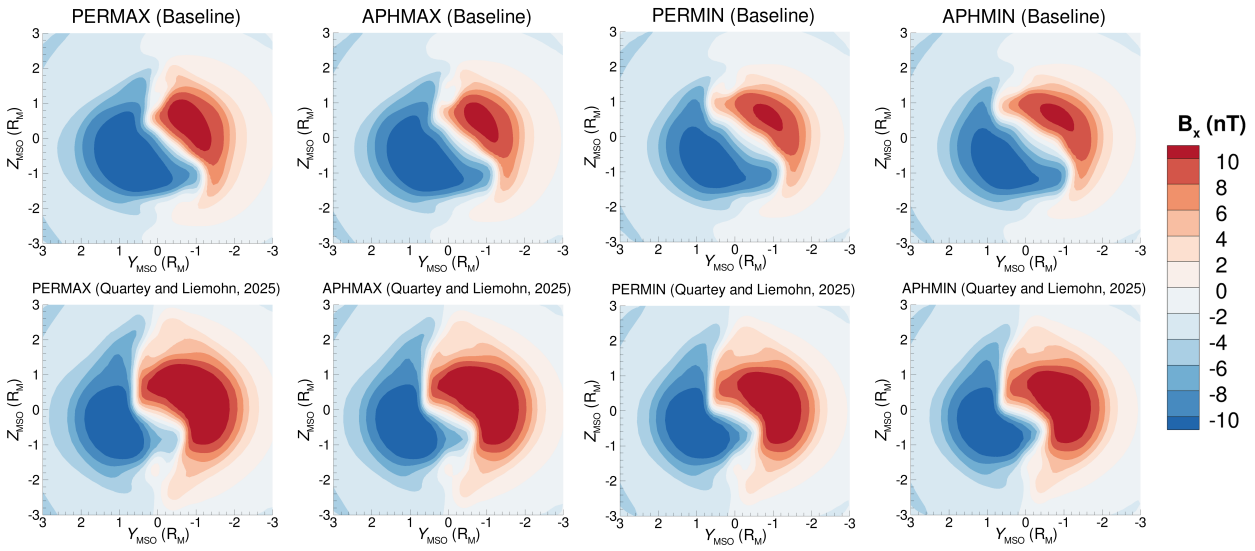


Figure 5.11: Slice of the magnetic field B_x at 2 R_M, plotted in the Y_{MSO}-Z_{MSO} plane. The top and bottom rows show the generalized and the logarithmic grid settings used in Quartey and Liemohn (2025) respectively. See Tables 5.1 and 5.3 for the details of each respective grid configuration. Each column shows a different solar condition (PERMAX, APHMAX, PERMIN, APHMIN).

Both grid settings reproduce the S-shaped structure seen in previous MHD simulations and satellite observations. However, the Quartey and Liemohn (2025) results primarily vary in magnitude, and the baseline settings show variations in both magnitude and the detailed structure of the magnetotail current sheet.This suggests that the baseline grid settings are more sensitive to parameter changes, capturing finer structural features in the tail.

Figure 5.12 compares the B_x along Y_{MSO} from -2 to 2 R_M, highlighting qualitative differences between the grid types. Baseline results are shown in blue, and the Quartey and Liemohn (2025) results are shown in red.

Across all cases, the baseline results appear smoother, while the Quartey and Liemohn (2025) results exhibit more small-scale fluctuations. Regardless, both results retain the characteristic S-shaped structure at every solar condition. Though the overall morphology remains consistent, this comparison shows that the grid geometry primarily affects the structure of the magnetotail current sheet.

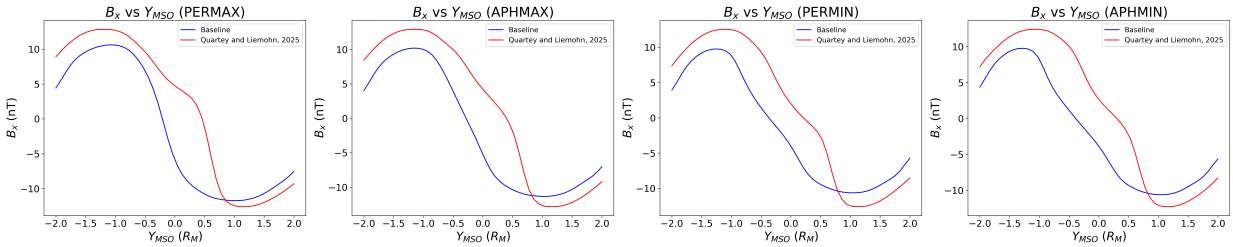


Figure 5.12: Comparison of B_x with respect to Y_{MSO} from -2 to 2 R_M, with the line extracted at X=-2 R_M. Lines in blue show the baseline grid configuration and lines in red show the Quartey and Liemohn (2025) grid configuration for PERMAX, APHMAX, PERMIN, and APHMIN.

5.5 Conclusion

We conduct a focused parameter study to evaluate how specific grid features influence the Mars magnetotail current sheet. Using the BATS-R-US multispecies MHD code, we establish a baseline configuration and systemically modify one parameter at a time to assess the sensitivity of the current sheet to each change.

Examination of the magnetic field B_x and total current density J shows minimal variation in the overall current sheet morphology when grid resolution or refinement levels are altered. However, the grid geometry produces noticeable differences. Specifically, the logarithmic grid is coarser at the inner boundary, resulting in a thinner but stronger current sheet.

Comparison of the baseline and Quartey and Liemohn (2025) grid configurations show that both reproduce the characteristic S-shaped magnetotail found in MHD simulations and satellite observations. However, the Quartey and Liemohn (2025) results deviate from the baseline and exhibit more small scale fluctuations, supporting the conclusion that the grid geometry significantly influences the structure of the magnetotail current sheet.

This study provides insight into how grid configuration influences the morphology of the Mars magnetotail current sheet. While determining which configuration most accurately reproduces physical conditions is beyond the scope of this work, the baseline configuration will serve as a foundation for future studies. Specifically, it will be further refined and

adjusted to enable a small scale data model comparison with MAVEN (Mars Atmosphere and Volatile EvolutioN) observations, allowing for assessment of how well the simulations reproduce the measured magnetic field structures.

CHAPTER 6

Comparison of MAVEN Observations and BATS-R-US Simulations at the Mars Magnetotail Current Sheet

A manuscript based on this chapter is in preparation for submission

6.1 Introduction

In situ measurements from the MAVEN mission provide detailed sampling of the nightside plasma environment, but the spacecraft's orbital geometry limits continuous spatial coverage. Global MHD models capture large-scale asymmetries, but results depend sensitively on model configuration and numerical resolution. A systematic assessment of how model setup affects the simulated dawn-dusk displacement relative to spacecraft observations has not yet been performed.

In Chapter 4, it was shown that the magnetotail current sheet structure changes with the orientation of the strongest crustal magnetic fields. In this chapter, that result is evaluated through a data-model comparison. Specifically, the analysis tests whether the Martian magnetotail exhibits structural variation consistent with those predicted by the simulations presented in Chapter 4.

Here, we compare global multispecies simulations using BATS-R-US with in situ measurements from MAVEN along a representative nightside orbit. This data-model comparison focuses on the magnetotail current sheet's structure and dawn-dawn displacement, including magnetic field strength and IMF orientation.

6.2 MAVEN Trajectory

The MAVEN mission arrived at Mars in September 2014, with the goal of understanding the role that atmospheric loss to space has played in the Mars space environment (Jakosky et al., 2015). MAVEN's orbit has a periapsis altitude of 150 km, apoapsis altitude of 6220 km, and a period of 4.5 hours. The dual vector fluxgate magnetometer (MAG) measures the intensity and direction of the magnetic field in regions traversed by MAVEN, providing information on the structure of the magnetic field throughout the magnetosphere (Connerney et al., 2015). The MAG instrument is used in this study for direct comparison with BATS-R-US simulation data.

We focus on MAVEN orbits in which apoapsis is located directly downtail of Mars, providing optimal sampling of the nightside magnetotail. The selected interval is 28 May 2017, during which two consecutive orbits were examined. The spacecraft is positioned near the central magnetotail current sheet at apoapsis, enabling clear identification of the dawn-dusk displacement and magnetic field structure. These orbits pass the central tail region and are optimal for testing whether the results of Chapter 4 are valid. The planet rotates as the MAVEN spacecraft moves from apoapse to apoapse, providing an opportunity to assess whether the change in structure is what is really happening behind the planet.

Figure 6.1 and Figure 6.2 show the MAVEN orbit summary plot on 28 May 2017 at 04:22 UTC and 08:54 UTC respectively. These times correspond to the two apoapsis passes analyzed in this study.

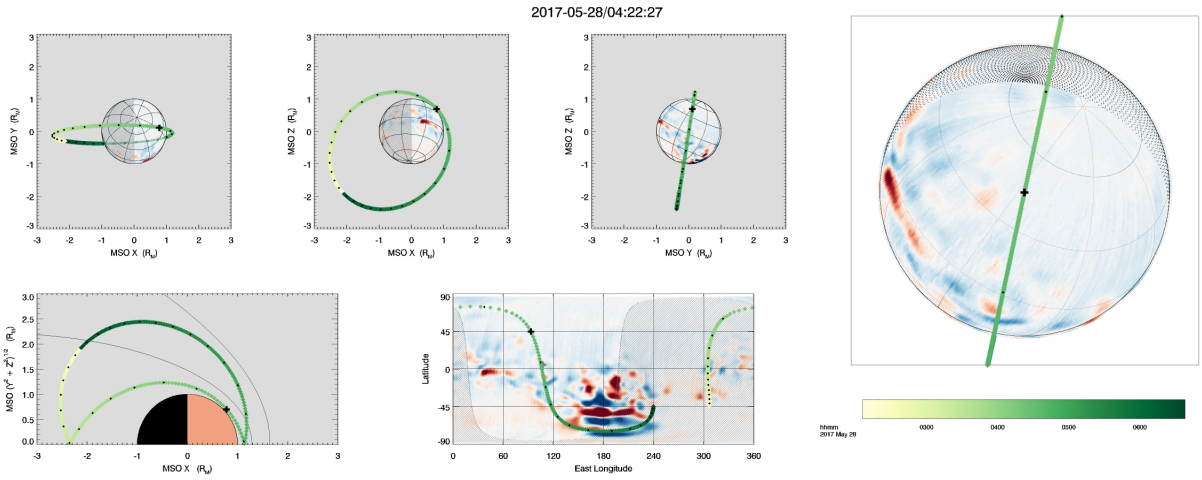


Figure 6.1: MAVEN orbit summary plot on 28 May 2017 at 04:22 UTC, obtained from the MAVEN Science Data Center. The top row shows the spacecraft trajectory in the $X_{MSO} - Y_{MSO}$, $X_{MSO} - Z_{MSO}$, and $Y_{MSO} - Z_{MSO}$ planes. The bottom row displays the trajectory in the $X_{MSO} - (Y^2 + Z^2)^{1/2}_{MSO}$ plane (left) and the map projection (right). The rightmost panel shows the 3D image of Mars and a color bar indicating orbit time. The plus symbol in each panel marks the spacecraft location at 04:22 UTC.

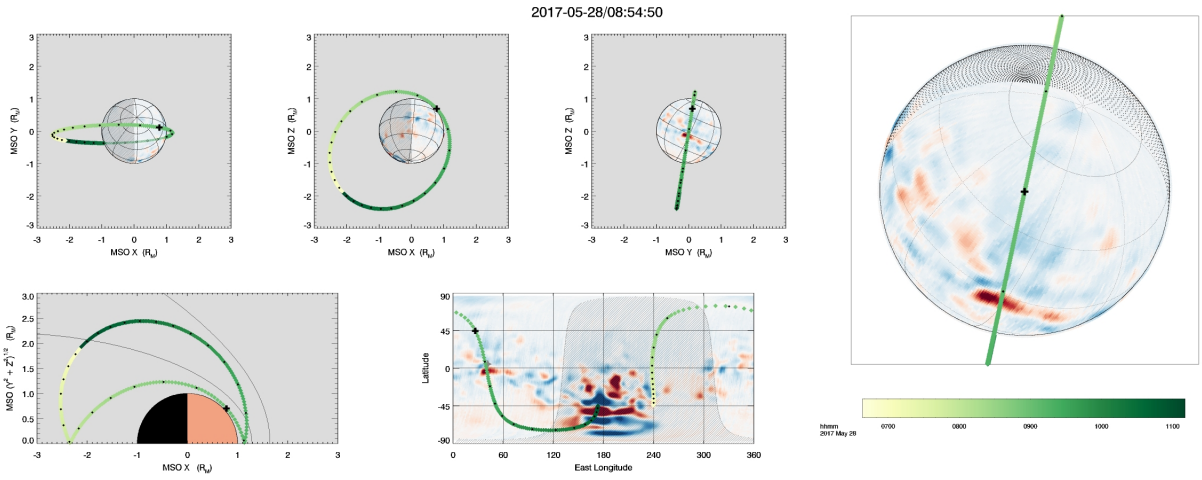


Figure 6.2: MAVEN orbit summary plot on 28 May 2017 at 08:54 UTC. See Figure 6.1 for interpretation of individual panels.

On 28 May 2017, Mars was located at approximately 1.5 AU from the Sun during solar minimum conditions of Solar Cycle 24. The plus symbols in the figures indicate the spacecraft position at the specified time. In Figure 6.1, the map projection shows the spacecraft near 90°E, 45°N on the dayside. Because this study focuses on the magnetotail current sheet,

we instead analyze the subsequent nightside segment of the orbit. Roughly one hour after the timestamp shown, the spacecraft transitions to the nightside near 120°E, 0°N, placing it closer to the central tail region.

Accordingly, the BATS-R-US simulation selected for comparison corresponds to solar minimum conditions with the spacecraft mapped to a subsolar longitude of 120°E, 0°N. In Figure 6.2, the spacecraft is initially located near 30°E, 45°N. Advancing roughly one hour along the trajectory places the spacecraft near 60°E, 0°N, which defines the corresponding location used for the solar minimum BATS-R-US comparison.

We use the MAVEN orbit summary plots as reference to associate magnetic field measurements with the spacecraft trajectory. The MAG data are aligned with MAVEN's 4.5 hour orbital period, starting at 00:00 UTC. Figures 6.3 and 6.4 show the spacecraft trajectories overlaid with the corresponding MAG measurements. The panels display the B_x, B_y, and B_z components in the $X_{MSO} - Y_{MSO}$ and $X_{MSO} - Z_{MSO}$ planes. Figure 6.3 corresponds to the first orbit segment from 00:00 to 04:30 UTC, while Figure 6.4 corresponds to the subsequent orbit from 04:30 to 09:00 UTC.

In the $X_{MSO} - Z_{MSO}$ plane, the spacecraft in in the magnetosheath when it is near the bow shock. We examine the magnetic field components in this region to assess the IMF orientation. In both Figures 6.3 and 6.4, B_x is predominantly negative (blue), B_y is positive (red), and B_z nears zero (a mix of gray and light blue). This configuration is consistent with an away-sector IMF for both orbits.

6.3 BATS-R-US Configuration

We use the BATS-R-US multispecies MHD code to simulate a steady-state global interaction between the solar wind and Mars. The simulation domain spans -24 $R_M < x < 8$ R_M, -16 R_M $< y <$ 16 R_M, -16 $R_M < z <$ 16 R_M. The effective grid resolution at the inner boundary is

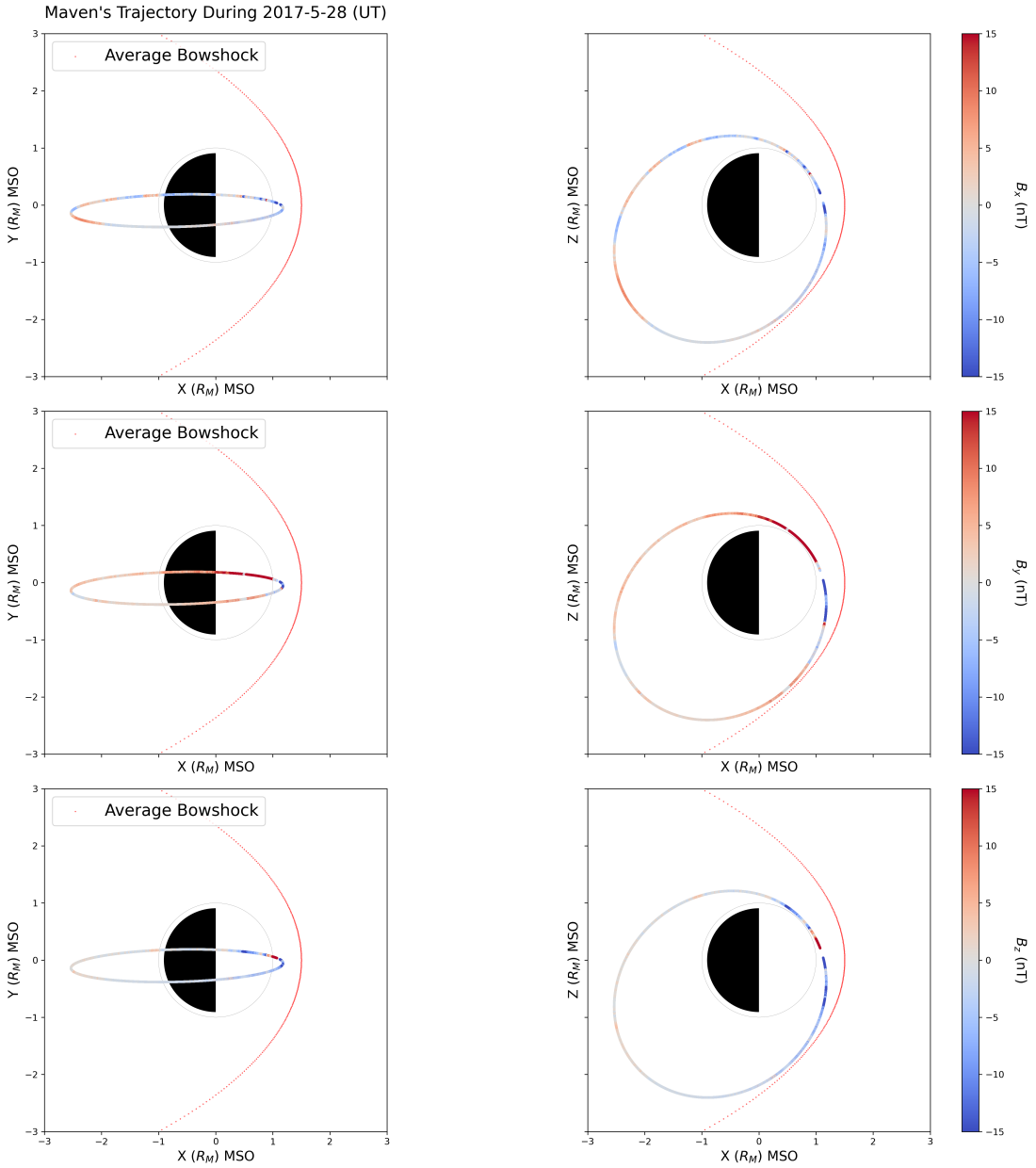


Figure 6.3: MAVEN orbit combined with MAG measurements on 28 May 2017 from 00:00-4:30 UTC. From top to bottom, the rows show the magnetic field components B_x, B_y, and B_z. From left to right, the columns show MAVEN's orbit trajectory in the $X_{MSO} - Y_{MSO}$ and $X_{MSO} - Z_{MSO}$ planes. The magnetic field is plotted from -15 to 15 nT in all directions, and all distances range from -3 to 3 R_M. The average bow shock (red dotted lines) is taken from Slavin et al. (1982), and MAG data is obtained from NASA's Coordinated Data Analysis Web (CDAWeb).

$\sim$8 km in the radial direction and 2°angularly. Simulations are driven by nominal solar wind conditions at Mars: the IMF is a 3 nT away sector Parker spiral (B_x=-1.67 nT, B_y=2.48

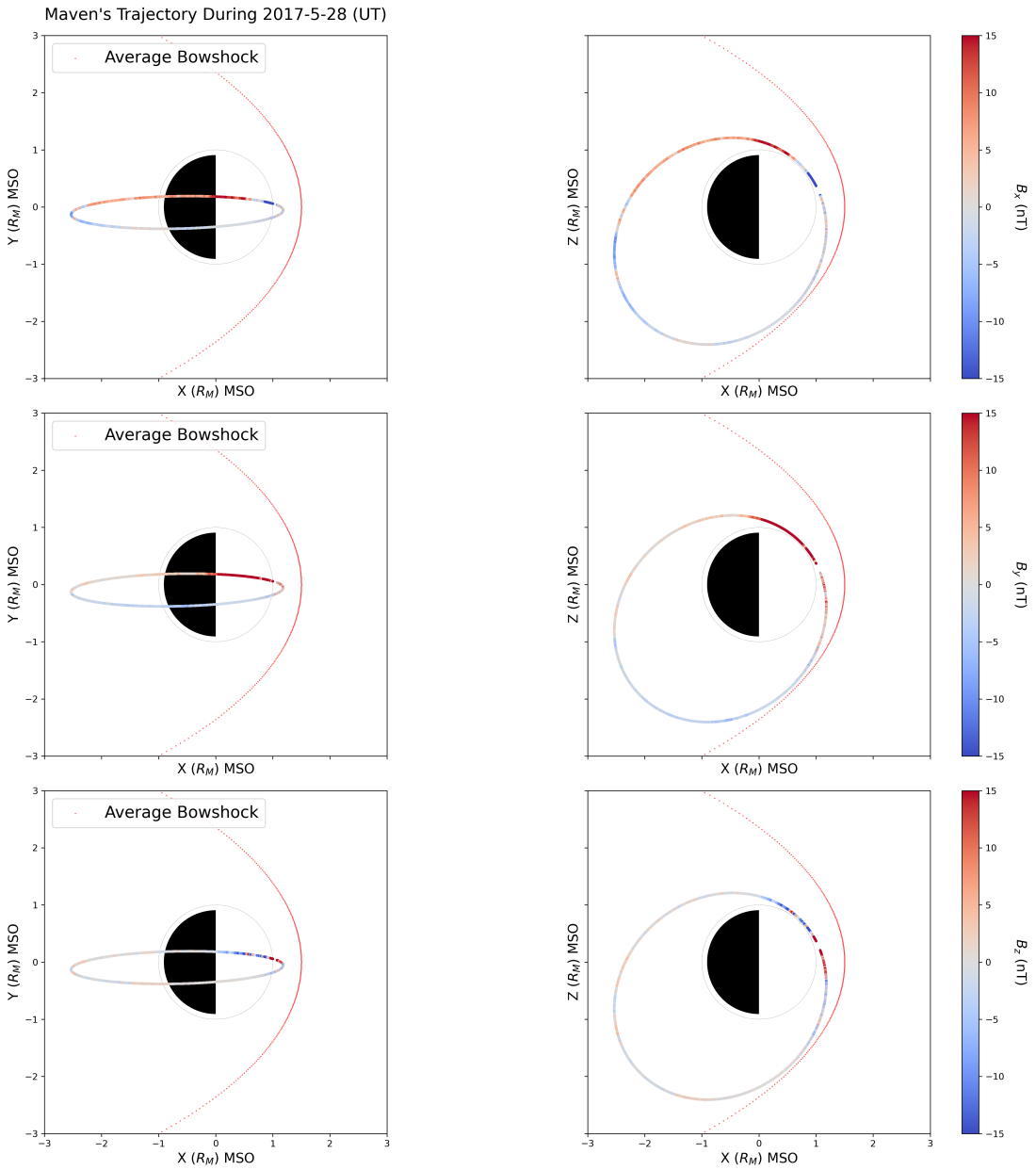


Figure 6.4: MAVEN orbit combined with MAG measurements on 28 May 2017 from 04:30-09:00 UTC. See Figure 6.3 for details of the plotted data.

nT, B_z=0), the solar wind density is 4 cm^{-3}, solar wind velocity is -400 km/s in x-direction, and the solar wind temperature is 3.5 $\times$ 10^5 K. As mentioned previously, the MAVEN pass on 28 May 2017 occurred during solar minimum conditions of Solar Cycle 24, and Mars was approximately 1.5 AU away from the Sun. As such, upstream parameters representative of solar minimum are used to drive the simulation.

Figure 6.5 shows the simulation results at 120°E, 0°N. Figure 6.6 shows the simulation results at 60°E, 0°N. In each figure, the columns correspond to the $X_{MSO} - Y_{MSO}$ and $Y_{MSO} - Z_{MSO}$ planes, and the rows display B_x, B_y, and B_z respectively, with the magnetic field components plotted from -15 to 15 nT.

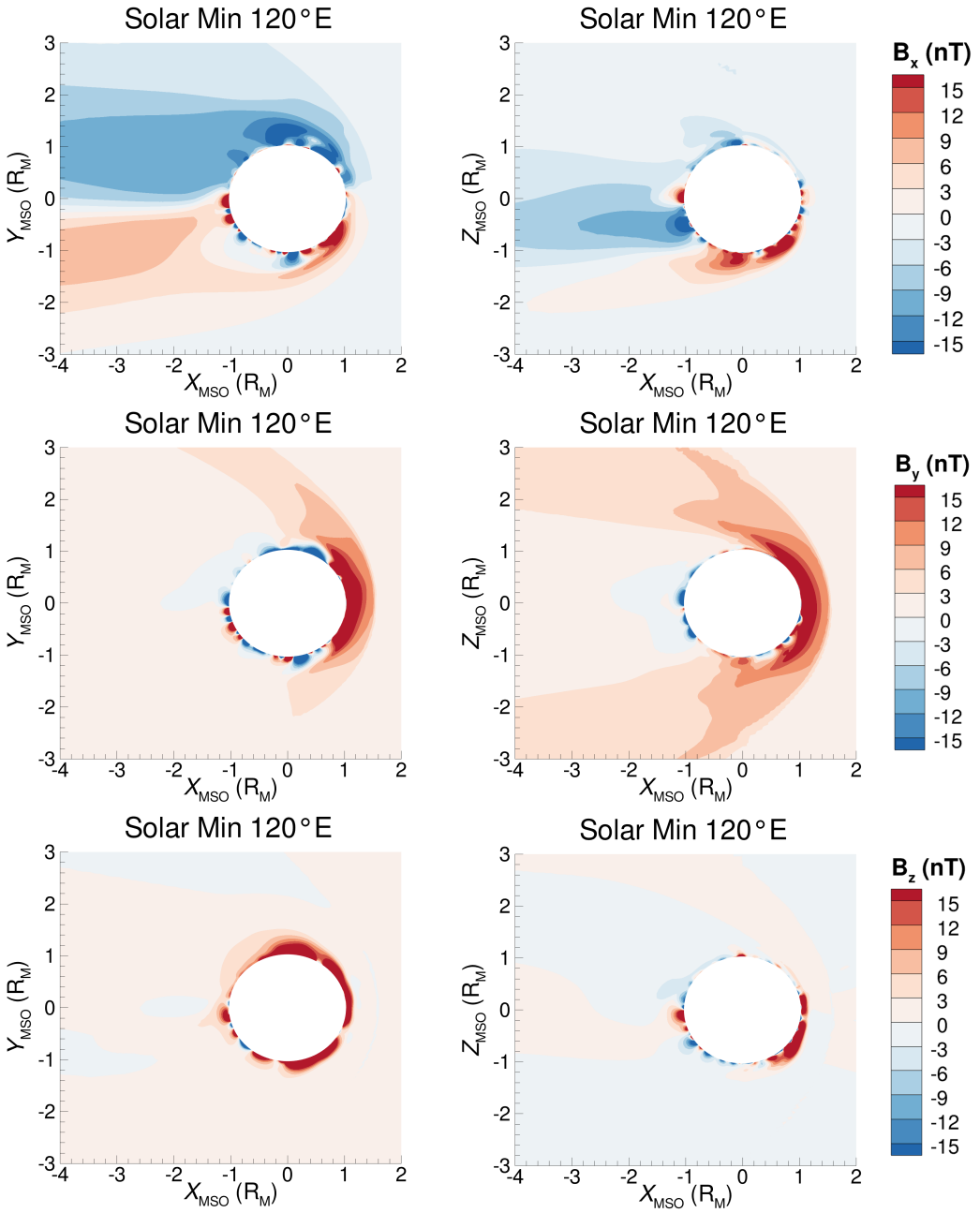


Figure 6.5: BATS-R-US simulation at solar minimum at the subsolar longitude of 120°E, 0°N. The columns correspond to the $X_{MSO} - Y_{MSO}$ and $Y_{MSO} - Z_{MSO}$ planes, and the rows display B_x, B_y, and B_z respectively, plotted from -15 to 15 nT.

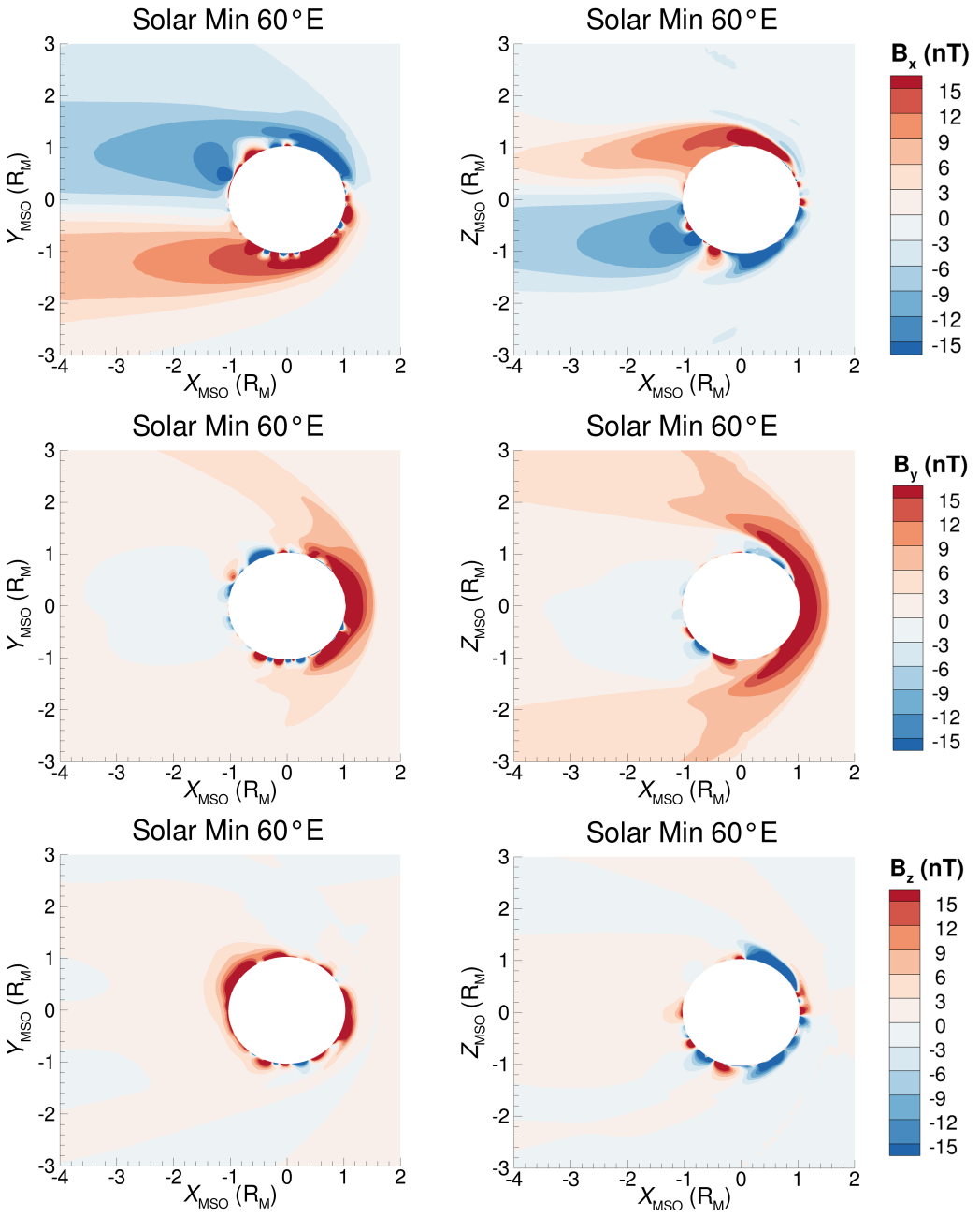


Figure 6.6: BATS-R-US simulation at solar minimum at the subsolar longitude of 60°E, 0°N. See Figure 6.5 for details of the plot.

Because BATS-R-US is a steady-state simulation, its outputs do not vary in time. To enable a direct comparison with MAVEN observations, we extract simulation data corresponding to the spatial region of interest rather than a specific timestamp. For each selected MAVEN orbit, we focus on a one-hour interval during which the B_x component reverses

sign, indicating the spacecraft's passage through the current sheet. This interval isolates the region of the current sheet crossing, which is the primary feature of interest in this study.

For the BATS-R-US comparison, we extract data from the corresponding region of the simulated magnetotail. Though the simulation is time-independent, we treat this spatial extraction to approximately a 10-minute segment of MAVEN measurements. This approach allows a consistent comparison of magnetic field structure across the current sheet, despite the differing temporal characteristics of the data sources.

6.4 Results

Figure 6.7 compares the MAG measurements from 02:15 to 03:15 UTC with the corresponding BATS-R-US solar minimum simulation extracted over a representative 10-minute interval near the modeled current sheet. The y-axis shows the B_x component of the magnetic field, while the x-axis shows time along the selected one hour segment of the MAVEN orbit. This interval was chosen because it captures the reversal of B_x, indicating the spacecraft's passage through the magnetotail current sheet.

The MAVEN observations exhibit a clear transition from positive to negative B_x near 02:50 UTC, marking the timestamp of the current sheet crossing. The BATS-R-US simulation reproduces a similar trend of B_x across the current sheet, though differences are evident in the magnitude. The similarities in the general trend provide an initial assessment of how well the model captures the observed magnetic field structure in the nightside magnetotail.

Figure 6.8 compares the MAG measurements from 07:10 to 08:10 UTC with the corresponding BATS-R-US solar minimum simulation extracted over a representative 10-minute interval near the modeled current sheet. As in the previous orbit, this interval was selected to capture the B_x reversal, indicating a current sheet crossing.

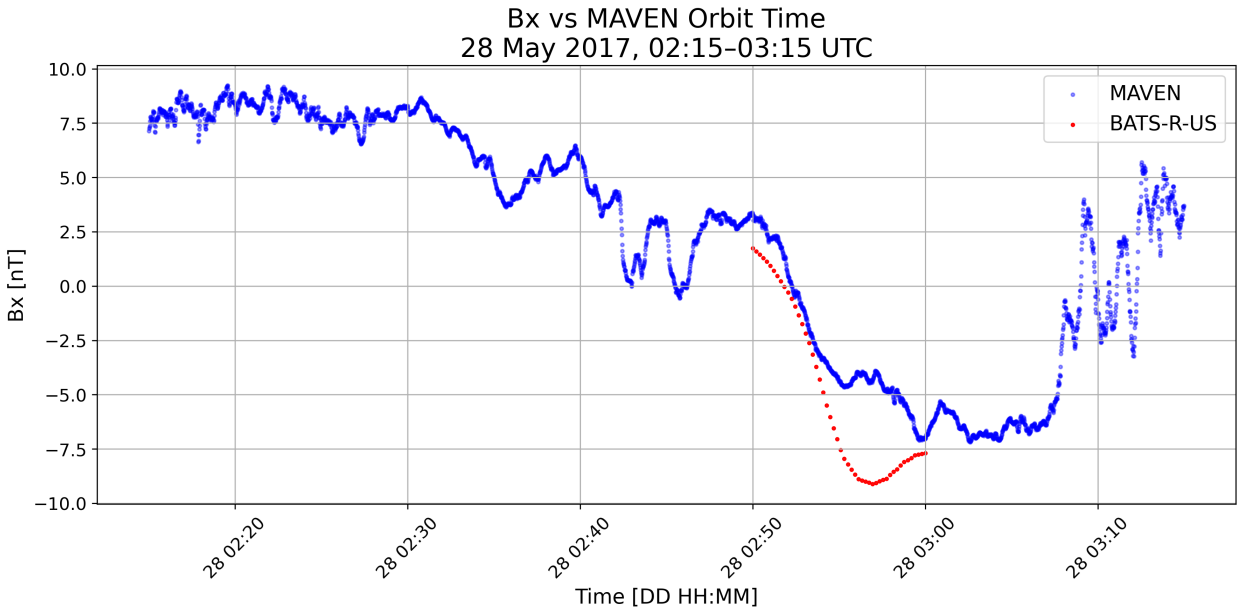


Figure 6.7: Comparison of the MAVEN pass (blue) in the magnetotail current sheet on 28 May 2017 from 02:15 to 03:15 UTC with BATS-R-US simulation (red) at 120°E, 0°N. The B_x component of the magnetic field is plotted on the y-axis as a function of time along the selected MAVEN orbit segment. The simulation values correspond to a spatial extraction near the modeled current sheet, treated as equivalent to a representative 10-minute interval for comparison.

Pronounced fluctuations in B_x are observed between 07:30 and 07:45 UTC, which could appears to be current sheet flapping. Current sheet flapping refers to quasi-periodic vertical oscillations of the magnetotail current sheet, often driven by instabilities or variations in upstream solar wind conditions. The timing and amplitude of the observed B_x fluctuations suggest that the magnetotail responds dynamically to transient solar wind forcing, causing the current sheet to oscillate. While the present analysis does not identify the exact driver of the flapping, the observed signatures in B_x are consistent with the expected morphology of such oscillations in the near-tail region.

Around 07:52 UTC, B_x undergoes a sustained reversal from negative to positive, marking the current sheet crossing. The BATS-R-US simulation reproduces the overall sign change large-scale trend in B_x, although it does not capture the smaller scale fluctuations present in MAVEN measurements, consistent with the idealized nature of the model.

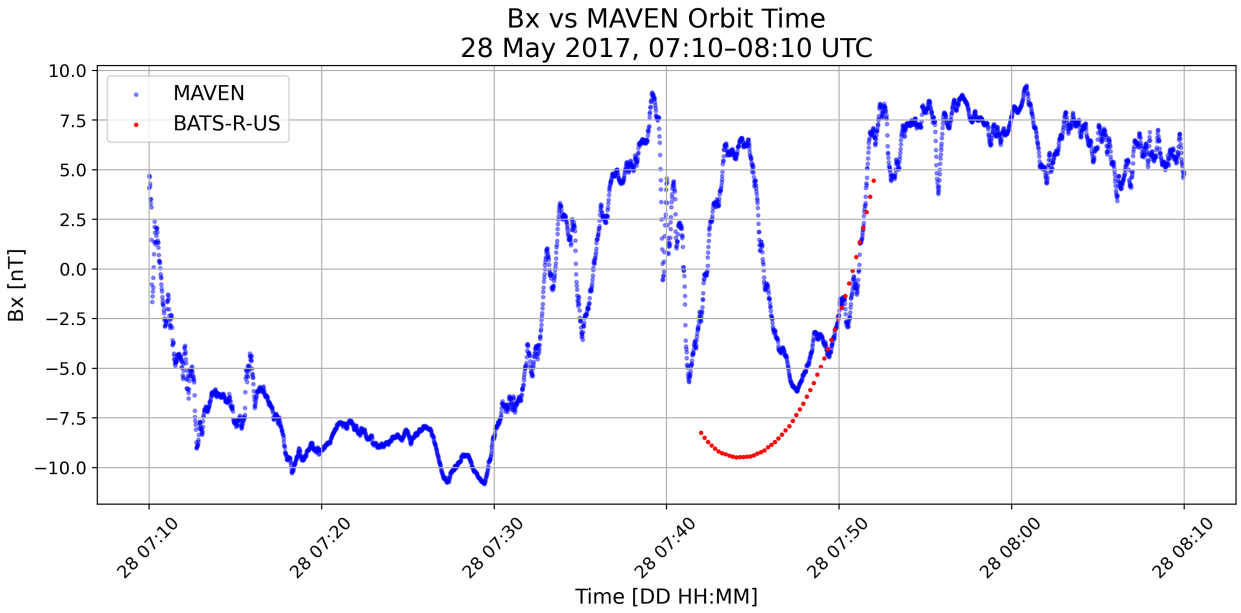


Figure 6.8: Comparison of the MAVEN pass in the magnetotail current sheet on 28 May 2017 from 07:10 to 08:10 UTC with BATS-R-US simulation at 60°E, 0°N. See Figure 6.7 for details of the plot.

In both results, the agreement in the timing of the B_x reversal indicates that the simulation captures the large-scale structure of the magnetotail current sheet. Discrepancies in variability highlight the limitations of a steady-state MHD framework in representing transient features.

6.5 Discussion

While the preliminary results demonstrate encouraging agreement between MAVEN observations and the BATS-R-US simulations, several limitations should be considered when interpreting these results.

The timing of the B_x reversal matches for these two for orbits, for which the reversal changed locaiton by substantial amount as the planet rotated between the apoapse passes. This match implies that the changes in spatial structure modeled in Chapter 4 are what is really happening in the Martian magnetotail.

6.5.1 BATS-R-US Interval Selection

The one hour MAVEN intervals were selected based on the reversal of the B_x component, which serves as a proxy for the magnetotail current sheet crossing. This isolates the primary feature of interest, but BATS-R-US represents a steady-state solution. The 10-minute simulation interval used for comparison is a spatial extraction intended to approximate the region sampled during the observed current sheet crossing rather than a true temporal match.

The choice of BATS-R-US interval length may influence the apparent agreement between the data and the model. A narrower window centered more tightly on the B_x reversal could emphasize large-scale structure, whereas a broader interval would incorporate additional variability and potentially increase discrepancies.

6.5.2 Model Configuration and Resolution

The BATS-R-US simulations used are steady-state and assume idealized upstream conditions. Short timescale fluctuations observed in the MAVEN measurements are not reproduced, likely because the model is capturing the time-independent magnetotail structure.

Numerical configuration may also influence the data-model comparison. Grid resolution and refinement directly affect the modeled current sheet thickness, gradient steepness, and the magnetitude of the dawn-dusk displacement. This investigation uses the baseline settings from Chapter 4, which uses the spherical generalized grid geometry. A more refined mesh near the inner boundary or the logarithmic grid geometry could potentially improve agreement with observations.

6.5.3 Steady-State Assumption

Because the simulations are steady-state, they do not capture planetary rotation, time-varying IMF conditions, or transient plasma dynamics. MAVEN samples a dynamic and evolving magnetosphere. As a result, the spacecraft trajectory through the magnetotail

reflects both spatial structure and temporal evolution, whereas the model represents a time-independent configuration.

A time-accurate simulation would allow the spacecraft trajectory and planetary rotation to be incorporated self-consistently. This approach could improve the spatial correspondence between the model and observations, allowing direct comparison of transient features. The current sheet crossings may also differ depending on the location of the strongest crustal magnetic fields.

6.5.4 Event Selection

This analysis focused on two orbits on 28 May 2017, providing concise comparison between MAVEN observations and BATS-R-US simulations. While these orbits capture clear current sheet crossing, including additional orbits from this day could further assess the consistency of the modeled dawn-dusk displacement across multiple crossings. Expanding the study to other MAVEN passes under similar upstream IMF conditions would allow evaluation of whether the observed agreement is event-specific or indicative of broader, systematic behavior in the nightside magnetotail. The implemented solar conditions (PERMAX, APHMAX, PERMIN, APHMIN) were not tested against MAVEN observations because Mars was approximately at 1.5 AU and the Sun the showed solar minimum conditions. A different MAVEN pass would help determine how well the solar condition implementations agree with the spacecraft.

6.6 Conclusion

This study presents a preliminary small-scale comparison between MAVEN observations and BATS-R-US simulations of the Mars magnetotail current sheet. Despite the model limitations, the results demonstrate encouraging agreement in the large-scale structure and dawn-dusk displacement of the current sheet. These findings highlight the potential of BATS-R-US

to reproduce key magnetotail feature and provide a foundation for future analyses involving additional orbits, time-dependent simulations, and various grid resolution configurations. As a focused case study, this work serves as a first step towards more comprehensive data-model comparisons.

CHAPTER 7

Conclusion

7.1 Summary

Through targeted improvements to the BATS-R-US multispecies MHD code, this work has enabled a more comprehensive investigation of the Martian magnetotail current sheet asymmetry. Using this framework, the following results address the science questions posed:

1. **How does the magnetotail current sheet asymmetry under the influence of crustal magnetic fields and ionosphere vary with Martian season?**

Four solar conditions are implemented in the BATS-R-US multispecies MHD code to investigate the magnetotail current sheet asymmetry is influence of orbital position:

- Solar maximum at perihelion (PERMAX)
- Solar maximum at aphelion (APHMAX)
- Solar minimum at perihelion (PERMIN)
- Solar minimum at aphelion (APHMIN)

For each case, the strongest crustal magnetic fields were positioned on the dayside (180°W, 0°N) and the magnetotail current sheet was shifted duskward ($+Y$). When crustal fields were omitted, this meant that the ionosphere was the key feature in preventing the solar wind from impinging on the surface of Mars. No systematic dawn-dusk shift occurred, suggesting

that the asymmetry is primarily driven by crustal fields.

Given that the magnetotail current sheet did not shift in these cases, the ionization rates were assessed to determine whether they would induce a more significant shift. Within BATS-R-US, the ionization rates were raised or lowered by one order of magnitude, depending on whether the solar condition was PERMAX or APHMIN. This process was repeated until either the magnetotail current sheet shifted significantly or the ionosphere dominated the Mars space environment. Though a slight shift was seen in both cases, it was determined that the ionization rates influenced the the magnetic field and ionosphere strength, but not the current sheet shift. Analysis of the dayside ionosphere O^+ ion species also revealed that a shift was not induced, validating the claim that the ionosphere does not contribute to the behavior seen in this MHD study. By incorporating seasonal variations into BATS-R-US, this investigation provided new insights into the the behavior of the current sheet.

2. **How does the magnetotail current sheet morphology change with subsolar longitude?**

Most MHD Mars-solar wind simulations orient the planet at 180°W, 0°N, where the strongest crustal magnetic fields are on the dayside. This study runs 24 steady-state simulations, incrementing Mars by 15°to examine the current sheet behavior at various subsolar longitudes. Near dusk (210-270°W), the magnetic field was more compressed. Everywhere else, the magnetic field was more space out. These results confirm that the subsolar longitude significantly influences the magnetotail current sheet asymmetry, but may also be influenced by broader features of the Mars space environment.

To investigate the drivers of this behavior, the total current density was examined as it provides a proxy for the distribution of magnetic forces throughout the magnetotail. This analysis revealed that the current sheet was uniform near dusk (210-270°W) and bifurcated (meaning it consisted of two spatially distinct current areas separated by a low current region) at all other subsolar longitudes, aligning with the behavior of the magnetic field.

Mass flux was examined to identify where strong plasma regions, and the results agreed with the current density behavior. This suggests at most subsolar longitudes, plasma is escaping through two channels in the magnetotail. Between 210-270°W, plasma is escaping through one channel. This study offers novel insights into the morphology and spatial variability of the current sheet.

3. **What grid configuration provides a reliable framework for data-model comparison with MAVEN observations?**

A grid-focused parameter study was conducted to evaluate how specific features influences the magnetotail current sheet. A baseline configuration was established with the generalized grid geometry, modest grid resolution, and minimal refinement. Settings were adjusted individually to determine how each influenced the magnetotail current sheet behavior.

Analysis of magnetic field and total current density showed little variation in the overall current sheet morphology when altering grid resolution or refinement levels. However, grid geometry had a significant impact. Using the logarithmic grid geometry resulted in a coarse inner boundary, producing a strong but thin current sheet. Despite grid geometry being the only notable deviation, the logarithmic and generalized grids reproduced the current sheet S-shape behavior seen in satellite observations. This case study provides insight to how grid configuration influences the morphology of the Mars magnetotail current sheet. While determining the grid configuration best for reproducing physical conditions at Mars is beyond the scope of this work, the baseline configuration was selected for comparison with MAVEN observations.

4. **Do the implemented modifications to the idealized MHD simulations agree with MAVEN observations?**

This study compares BATS-R-US multispecies MHD simulations with in situ measurements from MAVEN along a representative nightside orbit. The focus of the study is to determine whether BATS-R-US can successfully reproduce current sheet crossings from MAVEN.

The data-model comparison between MAVEN and BATS-R-US show the model captures large-scale structures and the magnetic field reversal of in the current sheet observed by MAVEN, showing encouraging signs of current sheet crossing agreement. While small-scale fluctuations are not captured due to the idealized nature of the simulations, the timing and sign reversal of B_x generally agree. The fact that there is close agreement for both of the apoapse passes through the central tail region indicates that the magnetotail configuration changes predicted by the numerical results are what is really happening at Mars.

7.2 Broader Implications

The projects in this dissertation demonstrate how Mars' magnetotail current sheet responds to seasonal, longitudinal, and geometric changes within a global multispecies MHD framework. By isolating the the drivers of asymmetry, this work provides a clearer physical interpretation of magnetotail structure not only analyzed by MHD models, but by observations from MAVEN.

By quantifying the seasonal, longitudinal, and geometric drivers of asymmetry. Because atmospheric escape is intimately linked to magnetotail dynamics, resolving these structural asymmetries improves our broader understanding of of Mars' atmospheric evolution.

More broadly, this work contributes to comparative studies of planetary magnetotails, particularly for unmagnetized or weakly magnetized bodies. As solar wind-planet interactions play a central role in shaping planetary environments across the solar system and beyond, understanding the fundamental drivers of tail structure at Mars provides insight into the plasma environments of terrestrial planets.

7.3 Future Work

Future work will continue development and application of the BATS-R-US model to further improve our understanding of magnetotail current sheet asymmetry. Specific areas for future investigation include:

- Run the BATS-R-US multispecies MHD code in time-accurate mode to investigate magnetotail current sheet motion and its response to dynamic solar wind conditions.

  Because our simulations are steady-state, Mars does not rotate and the IMF does not vary with time. Time-accurate simulations will allow us to implement rotation and tilt in our model, which will help reproduce more realistic magnetotail structures.

- Implementing and analyzing solar conditions from Chapter 3 into the BATS-R-US multifluid MHD model.

  PERMAX, APHMAX, PERMIN, and APHMIN have only been implemented in the BATS-R-US multispecies MHD code. Including these solar conditions in the multifluid MHD code will allow us to assess the magnetotail current sheet behavior under conditions where the major atmospheric ions have individual velocities and temperatures.

- Investigating the role of the major ion species (H^+, O_2^+, O^+, CO_2^+) in shaping magnetotail current sheet asymmetry.

  Chapter 3 went into brief detail of the influence of atmospheric ions on the dayside ionosphere. However, the influence of atmospheric ions in the magnetotail current sheet region has not been examined in detail. Atmospheric ions may improve our understanding of ion loss at Mars.

- Performing a more comprehensive grid comparison with additional diagnostic variables.

  The parameter focused case study in Chapter 5 only changed parameter at a time within BATS-R-US. Multiple changed grid parameters could yield a more refined grid

that yields more comparable results to MAVEN, even in an idealized simulation.

- Conducting a more robust data-model comparison between BATS-R-US simulations and MAVEN observations.

  This would involve comparing the BATS-R-US simulations to multiple MAVEN current sheet crossing in order to validate the results of Chapter 6 and modifying BATS-R-US conditions such as IMF orientation, solar wind speeds, and extreme space weather scenarios.

BIBLIOGRAPHY

Acuña, M. H., Connerney, J. E. P., F., N., Ness, Lin, R. P., Mitchell, D., Carlson, C. W., McFadden, J., Anderson, K. A., Rème, H., Mazelle, C., Vignes, D., Wasilewski, P., and Cloutier, P. (1999). Global distribution of crustal magnetization discovered by the mars global surveyor mag/er experiment. *Science*, 284:790–793.

Alfvén, H. (1957). On the theory of comet tails. *Tellus*, 9:92–96.

Arkani-Hamed, J. (2001). A 50-degree spherical harmonic model of the magnetic field of mars. *Journal of Geophysical Research: Planets*, 106:23197–23208.

Axford, W. I. (1962). The interaction between the solar wind and the earth's magnetosphere. *Journal of Geophysical Research*, 67:3791–3796.

Barabash, S., Fedorov, A., Lundin, R., and Sauvaud, J.-A. (2007). Martian atmospheric erosion rates. *Science*, 315:501–503.

Brain, D., Barabash, S., Boesswetter, A., Bougher, S., Brecht, S., Chanteur, G., Hurley, D., Dubinin, E., Fang, X., Fraenz, M., Halekas, J., Harnett, E., Holmstrom, M., Kallio, E., Lammer, H., Ledvina, S., Liemohn, M., Liu, K., Luhmann, J., Ma, Y., Modolo, R., Nagy, A., Motschmann, U., Nilsson, H., Shinagawa, H., Simon, S., and Terada, N. (2010). A comparison of global models for the solar wind interaction with mars. *Icarus*, 206:139–151.

Brecht, S. H. and Ledvina, S. A. (2006). The solar wind interaction with the martian ionosphere/atmosphere. *Space Science Reviews*, 126:15–38.

Bößwetter, A., Bagdonat, T., Motschmann, U., and Sauer, K. (2004). Plasma boundaries at mars: a 3-d simulation study. *Annales Geophysicae*, 22:4363–4379.

Carlsson, E., Brain, D., Luhmann, J., Barabash, S., Grigoriev, A., Nilsson, H., and Lundin, R. (2008). Influence of imf draping direction and crustal magnetic field location on martian ion beams. *Planetary and Space Science*, 56:861–867.

Connerney, J. E. P., Acuña, M. H., Wasilewski, P. J., Ness, N. F., Rème, H., Mazelle, C., Vignes, D., Lin, R. P., Mitchell, D. L., and Cloutier, P. A. (1999). Magnetic lineations in the ancient crust of mars. *Science*, 284:794–798.

Connerney, J. E. P., Acuña, M. H., Ness, N. F., Kletetschka, G., Mitchell, D. L., Lin, R. P., and Reme, H. (2005). Tectonic implications of mars crustal magnetism. *Proceedings of the National Academy of Sciences*, 102:14970–14975.

Connerney, J. E. P., Acuña, M. H., Wasilewski, P. J., Kletetschka, G., Ness, N. F., Rème, H., Lin, R. P., and Mitchell, D. L. (2001). The global magnetic field of mars and implications for crustal evolution. *Geophysical Research Letters*, 28:4015–4018.

Connerney, J. E. P., Espley, J., Lawton, P., Murphy, S., Odom, J., Oliversen, R., and Sheppard, D. (2015). The maven magnetic field investigation. *Space Science Reviews*, 195:257–291.

Crider, D., Acuña, M., Connerney, J., Mitchell, D., Lin, R., Cloutier, P., Rème, H., Mazelle, C., Brain, D., Ness, N., and Bauer, S. (2001). Magnetic field draping around mars: Mars global surveyor results. *Advances in Space Research*, 27:1831–1836.

Crider, D. H., Acuña, M. H., Connerney, J. E. P., Vignes, D., Ness, N. F., Krymskii, A. M., Breus, T. K., Rème, H., Mazelle, C., Mitchell, D. L., Lin, R. P., Cloutier, P. A., and Winterhalter, D. (2002). Observations of the latitude dependence of the location of the martian magnetic pileup boundary. *Geophysical Research Letters*, 29.

DiBraccio, G. A., Dann, J., Espley, J. R., Gruesbeck, J. R., Soobiah, Y., Connerney, J. E. P., Halekas, J. S., Harada, Y., Bowers, C. F., Brain, D. A., Ruhunusiri, S., Hara, T., and Jakosky, B. M. (2017). Maven observations of tail current sheet flapping at mars. *Journal of Geophysical Research: Space Physics*, 122:4308–4324.

DiBraccio, G. A., Espley, J. R., Gruesbeck, J. R., Connerney, J. E. P., Brain, D. A., Halekas, J. S., Mitchell, D. L., McFadden, J. P., Harada, Y., Livi, R., Collinson, G., Hara, T., Mazelle, C., and Jakosky, B. M. (2015). Magnetotail dynamics at mars: Initial maven observations. *Geophysical Research Letters*, 42:8828–8837.

DiBraccio, G. A., Luhmann, J. G., Curry, S. M., Espley, J. R., Xu, S., Mitchell, D. L., Ma, Y., Dong, C., Gruesbeck, J. R., Connerney, J. E. P., Harada, Y., Ruhunusiri, S., Halekas, J. S., Soobiah, Y., Hara, T., Brain, D. A., and Jakosky, B. M. (2018). The twisted configuration of the martian magnetotail: Maven observations. *Geophysical Research Letters*, 45:4559–4568.

DiBraccio, G. A., Romanelli, N., Bowers, C. F., Gruesbeck, J. R., Halekas, J. S., Ruhunusiri, S., Weber, T., Espley, J. R., Xu, S., Luhmann, J. G., Harada, Y., Dubinin, E., Poh, G. K., Brain, D. A., and Curry, S. M. (2022). A statistical investigation of factors influencing the magnetotail twist at mars. *Geophysical Research Letters*, 49.

Dong, C., Bougher, S. W., Ma, Y., Toth, G., Lee, Y., Nagy, A. F., Tenishev, V., Pawlowski, D. J., Combi, M. R., and Najib, D. (2015). Solar wind interaction with the martian upper atmosphere: Crustal field orientation, solar cycle, and seasonal variations. *Journal of Geophysical Research: Space Physics*, 120:7857–7872.

Dong, C., Bougher, S. W., Ma, Y., Toth, G., Nagy, A. F., and Najib, D. (2014). Solar wind interaction with mars upper atmosphere: Results from the one-way coupling between the multifluid mhd model and the mtgcm model. *Geophysical Research Letters*, 41:2708–2715.

Dubinin, E., Fraenz, M., Fedorov, A., Lundin, R., Edberg, N., Duru, F., and Vaisberg, O. (2011). Ion energization and escape on mars and venus. *Space Science Reviews*, 162:173–211.

Dubinin, E., Lundin, R., Norberg, O., and Pissarenko, N. (1993). Ion acceleration in the martian tail: Phobos observations. *Journal of Geophysical Research: Space Physics*, 98:3991–3997.

Egan, H., Ma, Y., Dong, C., Modolo, R., Jarvinen, R., Bougher, S., Halekas, J., Brain, D., Mcfadden, J., Connerney, J., Mitchell, D., and Jakosky, B. (2018). Comparison of global martian plasma models in the context of maven observations. *Journal of Geophysical Research: Space Physics*, 123:3714–3726.

Fang, X., Liemohn, M. W., Nagy, A. F., Luhmann, J. G., and Ma, Y. (2010). On the effect of the martian crustal magnetic field on atmospheric erosion. *Icarus*, 206:130–138.

Fang, X., Liemohn, M. W., Nagy, A. F., Ma, Y., Zeeuw, D. L. D., Kozyra, J. U., and Zurbuchen, T. H. (2008). Pickup oxygen ion velocity space and spatial distribution around mars. *Journal of Geophysical Research: Space Physics*, 113.

Fang, X., Ma, Y., Brain, D., Dong, Y., and Lillis, R. (2015). Control of mars global atmospheric loss by the continuous rotation of the crustal magnetic field: A time-dependent mhd study. *Journal of Geophysical Research: Space Physics*, 120.

Fox, J. L. and Sung, K. Y. (2001). Solar activity variations of the venus thermosphere/ionosphere. *Journal of Geophysical Research: Space Physics*, 106:21305–21335.

Gao, J. W., Rong, Z. J., Cai, Y. H., Lui, A. T. Y., Petrukovich, A. A., Shen, C., Dunlop, M. W., Wei, Y., and Wan, W. X. (2018). The distribution of two flapping types of magnetotail current sheet: Implication for the flapping mechanism. *Journal of Geophysical Research: Space Physics*, 123:7413–7423.

Gao, J. W., Rong, Z. J., Klinger, L., Li, X. Z., Liu, D., and Wei, Y. (2021). A spherical harmonic martian crustal magnetic field model combining data sets of maven and mgs. *Earth and Space Science*, 8.

Gombosi, T. I., Chen, Y., Glocer, A., Huang, Z., Jia, X., Liemohn, M. W., Manchester, W. B., Pulkkinen, T., Sachdeva, N., Shidi, Q. A., Sokolov, I. V., Szente, J., Tenishev, V., Toth, G., van der Holst, B., Welling, D. T., Zhao, L., and Zou, S. (2021). What sustained multi-disciplinary research can achieve: The space weather modeling framework. *Journal of Space Weather and Space Climate*, 11:42.

Gombosi, T. I., Tóth, G., Zeeuw, D. L. D., Hansen, K. C., Kabin, K., and Powell, K. G. (2002). Semirelativistic magnetohydrodynamics and physics-based convergence acceleration. *Journal of Computational Physics*, 177:176–205.

Gringauz, K., Bezrukhikh, V., Verigin, M., and Remizov, A. (1975). Studies of solar plasma near mars and along the earth-mras path, 3. characteristics of ion and electron components measured on satellite mars-5. *Cosmic Res*, 13:107.

Harnett, E. M. and Winglee, R. M. (2003). The influence of a mini-magnetopause on the magnetic pileup boundary at mars. *Geophysical Research Letters*, 30.

Harnett, E. M. and Winglee, R. M. (2005). Three-dimensional fluid simulations of plasma asymmetries in the martian magnetotail caused by the magnetic anomalies. *Journal of Geophysical Research: Space Physics*, 110.

Jakosky, B. M., Lin, R. P., Grebowsky, J. M., Luhmann, J. G., Mitchell, D. F., Beutelschies, G., Priser, T., Acuna, M., Andersson, L., Baird, D., Baker, D., Bartlett, R., Benna, M., Bougher, S., Brain, D., Carson, D., Cauffman, S., Chamberlin, P., Chaufray, J.-Y., Cheatom, O., Clarke, J., Connerney, J., Cravens, T., Curtis, D., Delory, G., Demcak, S., DeWolfe, A., Eparvier, F., Ergun, R., Eriksson, A., Espley, J., Fang, X., Folta, D., Fox, J., Gomez-Rosa, C., Habenicht, S., Halekas, J., Holsclaw, G., Houghton, M., Howard, R., Jarosz, M., Jedrich, N., Johnson, M., Kasprzak, W., Kelley, M., King, T., Lankton, M., Larson, D., Leblanc, F., Lefevre, F., Lillis, R., Mahaffy, P., Mazelle, C., McClintock, W., McFadden, J., Mitchell, D. L., Montmessin, F., Morrissey, J., Peterson, W., Possel, W., Sauvaud, J.-A., Schneider, N., Sidney, W., Sparacino, S., Stewart, A. I. F., Tolson, R., Toublanc, D., Waters, C., Woods, T., Yelle, R., and Zurek, R. (2015). The mars atmosphere and volatile evolution (maven) mission. *Space Science Reviews*, 195:3–48.

Kallio, E., Fedorov, A., Budnik, E., Barabash, S., Jarvinen, R., and Janhunen, P. (2008). On the properties of o+ and o2+ ions in a hybrid model and in mars express ima/aspera-3 data: A case study. *Planetary and Space Science*, 56:1204–1213.

Lang, K. (2005). *SOLAR SYSTEM — The Sun*, pages 209–220. Elsevier.

Langlais, B., Thébault, E., Houliez, A., Purucker, M., and Lillis, R. (2019). A new model of the crustal magnetic field of mars using mgs and maven. *Journal of Geophysical Research: Planets*, 124:1542–1569.

Ledvina, S. A., Brecht, S. H., Brain, D. A., and Jakosky, B. M. (2017). Ion escape rates from mars: Results from hybrid simulations compared to maven observations. *Journal of Geophysical Research: Space Physics*, 122:8391–8408.

Li, L., Xie, L., Zhang, Y., and Liu, T. (2013). Model investigation of current system and influence of the crustal fields on the large scale structure of current sheets at mars. *Planetary and Space Science*, 86:80–85.

Li, X. Z., Rong, Z. J., Fraenz, M., Zhang, C., Klinger, L., Shi, Z., Gao, J. W., Dunlop, M. W., and Wei, Y. (2023). Two types of martian magnetotail current sheets: Maven observations of ion composition. *Geophysical Research Letters*, 50.

Liemohn, M. W. and Xu, S. (2018). *Recent Advances Regarding the Mars Magnetotail Current Sheet*, pages 177–190.

Liemohn, M. W., Xu, S., Dong, C., Bougher, S. W., Johnson, B. C., Ilie, R., and Zeeuw, D. L. D. (2017). Ionospheric control of the dawn-dusk asymmetry of the mars magnetotail current sheet. *Journal of Geophysical Research: Space Physics*, 122:6397–6414.

Luhmann, J. G. and Brace, L. H. (1991). Near-mars space. *Reviews of Geophysics*, 29:121–140.

Luhmann, J. G., Dong, C., Ma, Y., Curry, S. M., Mitchell, D., Espley, J., Connerney, J., Halekas, J., Brain, D. A., Jakosky, B. M., and Mazelle, C. (2015). Implications of maven mars near-wake measurements and models. *Geophysical Research Letters*, 42:9087–9094.

Luhmann, J. G., Russell, C. T., Scarf, F. L., Brace, L. H., and Knudsen, W. C. (1987). Characteristics of the marslike limit of the venus-solar wind interaction. *Journal of Geophysical Research: Space Physics*, 92:8545–8557.

Lundin, R. (2011). Ion acceleration and outflow from mars and venus: An overview. *Space Science Reviews*, 162:309–334.

Ma, Y., Fang, X., Russell, C. T., Nagy, A. F., Toth, G., Luhmann, J. G., Brain, D. A., and Dong, C. (2014). Effects of crustal field rotation on the solar wind plasma interaction with mars. *Geophysical Research Letters*, 41:6563–6569.

Ma, Y. and Nagy, A. F. (2007). Ion escape fluxes from mars. *Geophysical Research Letters*, 34.

Ma, Y., Nagy, A. F., Hansen, K. C., DeZeeuw, D. L., Gombosi, T. I., and Powell, K. G. (2002). Three-dimensional multispecies mhd studies of the solar wind interaction with mars in the presence of crustal fields. *Journal of Geophysical Research: Space Physics*, 107.

Ma, Y., Nagy, A. F., Sokolov, I. V., and Hansen, K. C. (2004). Three-dimensional, multispecies, high spatial resolution mhd studies of the solar wind interaction with mars. *Journal of Geophysical Research: Space Physics*, 109.

Ma, Y. J., Dong, C. F., Toth, G., van der Holst, B., Nagy, A. F., Russell, C. T., Bougher, S., Fang, X., Halekas, J. S., Espley, J. R., Mahaffy, P. R., Benna, M., McFadden, J., and Jakosky, B. M. (2019). Importance of ambipolar electric field in driving ion loss from mars: Results from a multifluid mhd model with the electron pressure equation included. *Journal of Geophysical Research: Space Physics*, 124:9040–9057.

Ma, Y. J., Russell, C. T., Fang, X., Dong, Y., Nagy, A. F., Toth, G., Halekas, J. S., Connerney, J. E. P., Espley, J. R., Mahaffy, P. R., Benna, M., McFadden, J. P., Mitchell, D. L., and Jakosky, B. M. (2015). Mhd model results of solar wind interaction with mars and comparison with maven plasma observations. *Geophysical Research Letters*, 42:9113–9120.

McComas, D. J., Spence, H. E., Russell, C. T., and Saunders, M. A. (1986). The average magnetic field draping and consistent plasma properties of the venus magnetotail. *Journal of Geophysical Research: Space Physics*, 91:7939–7953.

Modolo, R., Chanteur, G. M., Dubinin, E., and Matthews, A. P. (2005). Influence of the solar euv flux on the martian plasma environment. *Annales Geophysicae*, 23:433–444.

Nagy, A., Winterhalter, D., Sauer, K., Cravens, T., Brecht, S., Mazelle, C., Crider, D., Kallio, E., Zakharov, A., Dubinin, E., Verigin, M., Kotova, G., Axford, W., Bertucci, C., and Trotignon, J. (2004). The plasma environment of mars. *Space Science Reviews*, 111:33–114.

Nagy, A. F., Gombosi, T. I., Szego, K., Sagdeev, R. Z., Shapiro, V. D., and Shevchenko, V. I. (1990). Venus mantle-mars planetosphere: What are the similarities and differences? *Geophysical Research Letters*, 17:865–868.

Najib, D., Nagy, A. F., Tóth, G., and Ma, Y. (2011). Three-dimensional, multifluid, high spatial resolution mhd model studies of the solar wind interaction with mars. *Journal of Geophysical Research: Space Physics*, 116.

Nauth, M., Mitchell, D. L., Fowler, C. M., de Pater, I., and Azari, A. R. (2024). Evidence for a current system and potential structure in the martian magnetotail. *Journal of Geophysical Research: Space Physics*, 129.

Parker, E. N. (1958). Dynamics of the interplanetary gas and magnetic fields. *Astrophysical Journal, vol. 128, p. 664*, 128:664.

Peter, K., Sánchez-Cano, B., Němec, F., González-Galindo, F., Kopf, A. J., Lester, M., Pätzold, M., Regan, C. E., and Holmström, M. (2024). The ionosphere of mars after 20 years of mars express contributions. *Space Science Reviews*, 220:41.

Powell, K. G., Roe, P. L., Linde, T. J., Gombosi, T. I., and Zeeuw, D. L. D. (1999). A solution-adaptive upwind scheme for ideal magnetohydrodynamics. *Journal of Computational Physics*, 154:284–309.

Quartey, N. A. and Liemohn, M. W. (2025). Multispecies mhd simulations of the crustal field influence at the mars magnetotail current sheet. *Journal of Geophysical Research: Space Physics*, 130.

Quartey, N. A., Liemohn, M. W., Ma, Y., Sun, W., and Curry, S. M. (2026). Rotational influence on the martian magnetotail current sheet: A multispecies mhd study. *Journal of Geophysical Research: Space Physics*, 131.

Romanelli, N., Modolo, R., Leblanc, F., Chaufray, J., Hess, S., Brain, D., Connerney, J., Halekas, J., Mcfadden, J., and Jakosky, B. (2018). Effects of the crustal magnetic fields and changes in the imf orientation on the magnetosphere of mars: Maven observations and lathys results. *Journal of Geophysical Research: Space Physics*, 123:5315–5333.

Russell, C. T., Elphic, R. C., and Slavin, J. A. (1980). Limits on the possible intrinsic magnetic field of venus. *Journal of Geophysical Research: Space Physics*, 85:8319–8332.

Sakata, R., Seki, K., Sakai, S., Terada, N., Shinagawa, H., and Tanaka, T. (2020). Effects of an intrinsic magnetic field on ion loss from ancient mars based on multispecies mhd simulations. *Journal of Geophysical Research: Space Physics*, 125.

Schunk, R. W. and Nagy, A. F. (2000). *Ionospheres*. Cambridge University Press.

Slavin, J. A., Holzer, R. E., Spreiter, J., Stahara, S., and Chausee, D. (1982). Solar wind flow about the terrestrial planets. *Comparison with gas-dynamic theory and implications for*.

Sun, W., Ma, Y., Russell, C. T., Luhmann, J., and Brain, D. (2025). Magnetohydrodynamic study of mars's response to short-term solar wind dynamic pressure enhancements. *The Astrophysical Journal*, 991:40.

Sun, W., Ma, Y., Russell, C. T., Luhmann, J., Nagy, A., and Brain, D. (2023). 5-species mhd study of martian proton loss and source. *Journal of Geophysical Research: Space Physics*, 128.

Sun, W., Sakata, R., Ma, Y., Seki, K., Russell, C. T., Terada, N., Sakai, S., Shinagawa, H., Brain, D., and Toth, G. (2024). Comprehensive comparison of two global multi-species mhd models of mars. *Earth and Space Science*, 11.

Terada, N., Kulikov, Y. N., Lammer, H., Lichtenegger, H. I., Tanaka, T., Shinagawa, H., and Zhang, T. (2009). Atmosphere and water loss from early mars under extreme solar wind and extreme ultraviolet conditions. *Astrobiology*, 9:55–70.

Tóth, G. (2000). The $\nabla \cdot b=0$ constraint in shock-capturing magnetohydrodynamics codes. *Journal of Computational Physics*, 161:605–652.

Tóth, G., van der Holst, B., Sokolov, I. V., Zeeuw, D. L. D., Gombosi, T. I., Fang, F., Manchester, W. B., Meng, X., Najib, D., Powell, K. G., Stout, Q. F., Glocer, A., Ma, Y.-J., and Opher, M. (2012). Adaptive numerical algorithms in space weather modeling. *Journal of Computational Physics*, 231:870–903.

Vaisberg, O. L., Bogdanov, A. V., Smirnov, V. N., and Romanov, S. A. (1975). Initial results of ion flux measurements by the riep-2801 m instrument on mars-4 and mars-5. *Cosmic Res. (USSR) (Engl. Transl.), v. 13, no. 1, pp. 112-113*.

Verigin, M., Kotova, G., Remizov, A., Szegö, K., Tátrallyay, M., Slavin, J., Rosenbauer, H., Livi, S., Riedler, W., Schwingenschuh, K., and Zhang, T.-L. (2001). Evidence of the influence of equatorial martian crustal magnetization on the position of the planetary magnetotail boundary by phobos 2 data. *Advances in Space Research*, 28:885–889.

Vignes, D., Mazelle, C., Rme, H., Acuña, M. H., Connerney, J. E. P., Lin, R. P., Mitchell, D. L., Cloutier, P., Crider, D. H., and Ness, N. F. (2000). The solar wind interaction with mars: Locations and shapes of the bow shock and the magnetic pile-up boundary from the observations of the mag/er experiment onboard mars global surveyor. *Geophysical Research Letters*, 27:49–52.

Wang, L., Huang, C., Du, A., Ge, Y., Zhao, J., and Chen, D. (2025). Solar wind control of the martian magnetotail current sheet and magnetic reconnection. *The Astrophysical Journal*, 984:131.

Wang, M., Guan, Z., Xie, L., Lu, J., Wei, G., Sui, H., Zhang, J., Li, J., Zhang, H., Qu, B., Xu, Q., and Li, L. (2024). The effect of the interplanetary magnetic field clock angle and the latitude location of the intense crustal magnetic field on the ion escape at mars: An mhd simulation study. *Journal of Geophysical Research: Space Physics*, 129.

Wang, M., Guan, Z. J., Xie, L., Lu, J. Y., Xu, X., Wei, Y., Zhou, Z., Chai, L., Wang, J., Chang, Q., Zhang, H. X., Qu, B. H., Sui, H. Y., Zhang, J. Q., Qiao, F. H., and Li, L. (2023). Three-dimensional mhd simulations of the magnetic pileup at mars. *The Astronomical Journal*, 166:179.

Wen, Y., Rong, Z., Nilsson, H., Zhang, C., Shen, H.-W., and Gao, J. (2025). Statistical investigations of the radial interplanetary magnetic field component impact on the magnetotail current sheet structure of mars: Maven observations. *The Astrophysical Journal*, 993:201.

Xu, S., Liemohn, M. W., Dong, C., Mitchell, D. L., Bougher, S. W., and Ma, Y. (2016). Pressure and ion composition boundaries at mars. *Journal of Geophysical Research: Space Physics*, 121:6417–6429.

Yeroshenko, Y., Riedler, W., Schwingenschuh, K., Luhmann, J. G., Ong, M., and Russell, C. T. (1990). The magnetotail of mars: Phobos observations. *Geophysical Research Letters*, 17:885–888.

Zhang, C., Rong, Z., Zhang, L., Gao, J., Shi, Z., Klinger, L., Shen, C., and Wei, Y. (2023). Properties of flapping current sheet of the martian magnetotail. *Journal of Geophysical Research: Space Physics*, 128.